

ABSTRACT

CONNOR JR, DEAN MICHAEL. Application of diffraction enhanced imaging to bone.

(Under the direction of Hans D. Hallen)

Diffraction enhanced imaging (DEI) is a new x-ray-based medical imaging modality that is in its early stages of development and testing. In images generated using DEI, contrast is from absorption and refraction of x-rays and from ultra-small angle x-ray scattering (USAXS). Though accepted values for x-ray absorption in biological tissues have been established, only recently have investigators begun probing for characteristic refraction and USAXS from biological tissues. For this work, a series of four experiments were performed at the National Synchrotron Light Source (Upton, NY, USA) beamline X15A to help characterize DEI of bone. In the first experiment, the USAXS profile was measured for pre- and post-fatigue loaded cortical bone. Though no clear pattern of change in the USAXS profile was found, the bone samples were shown to have a measurable USAXS signal and it was found that large refracting structures within bone (>100 microns) could be visualized. In the next two experiments, the contrast of DEI's refraction and apparent absorption images was compared to the contrast in synchrotron radiation (SR) radiographs for planar imaging of gap regions in bone and for imaging of trabecular structure in tomography mode. DEI was shown to have significant contrast-to-noise ratio gains over SR radiographs in both experiments. The planar refraction and apparent absorption signals in the gap imaging experiment were shown to be consistent with their theoretically predicted values. DEI in tomography mode (DECT) was found to have significant resolution gains over comparably

obtained SRCT images. In the final experiment, a computer model was developed to predict USAXS from cortical bone and the computer model results were compared to USAXS data obtained using DEI. The scattering widths, as predicted by the computer model, suggest that osteocyte lacunae cause the experimentally measured angular spreading of the x-ray beam. The findings of these experiments provide the impetus for further studies of bone with DEI emphasizing clinical applications.

APPLICATION OF DIFFRACTION ENHANCED IMAGING TO BONE

by

DEAN MICHAEL CONNOR, JR

A dissertation submitted to the Graduate Faculty of

North Carolina State University

in partial fulfillment of the

requirements for the Degree of

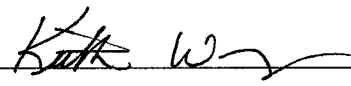
Doctor of Philosophy

PHYSICS

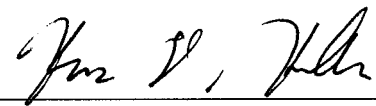
Raleigh, NC

2005

APPROVED BY:

 _____  _____

 _____  _____

 _____  _____

Chair of advisory committee

He is like a man which built an house, and digged deep, and laid the foundation on a rock: and when the flood arose, the stream beat vehemently upon that house, and could not shake it: for it was founded upon a rock.

Luke 6:48

In memory of Dr. Dale Sayers and Pastor Joe Sarver, the two most profound influences on my scientific, personal, and spiritual growth in my graduate school life.

BIOGRAPHY

I was born in Hibbing, Minnesota on January 23, 1978. The first nine years of my life were spent enjoying the mild spring-like summers and the arctic winters of northern Minnesota. Much of my childhood life involved school, church, hockey (an inevitability, given my geographic location, paired with the fact that my dad played varsity hockey at the University of Wisconsin), playing ninja in the woods surrounding my friends' lake homes, and building Barbie houses with my Construx (unavoidable in a house with three sisters and no brothers).

After several years and a couple moves, my family ended up in Farmington Hills, Michigan, where began the most influential year of my life so far. It was my junior year at Harrison High School, when I decided to take the introductory physics course with Mr. Dennis King. He had an enthusiasm for teaching in general, and for teaching physics specifically, that made a lasting impression on me. Unfortunately, during that school year my family was forced to move again, this time to Hartland, Wisconsin. As luck would have it though, I went from one incredibly gifted and enthusiastic teacher in Michigan to another equally enthusiastic and gifted teacher in Wisconsin, Mrs. Cheryl Kaiser. The move away from established friendships in Michigan was a very rough one, but it ended up that I was not alone—three other guys had just moved to the area as juniors in high school. As luck would have it, two of the other guys were on the hockey team, we had three classes together, and we went to the same church youth group. Our little group of vagabonds bonded over physics problem sessions, tough hockey practices, and youth group activities. It was during this year that I decided I would really like to share my teachers' enthusiasm towards physics, to pass

on the torch to the next generation of students. It was also during that year I decided Christianity was a very important part of my life. In one way or another, most of my life choices since that year have been molded by those two decisions.

Though I had it in my head that it would be great to be a physics teacher, I decided to take a somewhat circuitous route to get there. After finishing up with high school, I moved out to rural Wisconsin to attend school at the University of Wisconsin-Platteville, where I chose to study Engineering Physics (they did not have a plain physics degree program). As graduation approached I had to decide whether to try to find an engineering job or to go to graduate school. Though I had an enthusiasm for teaching physics, I still was not completely sure this was what I wanted to do with my life. After more than a little bit of indecision, I decided to go to graduate school at North Carolina State University to study physics.

The decision to go to NC State ended up being a far better one than I had anticipated. To start off with, they were very understanding of my situation coming in—that I did not have the physics background that many students had coming into graduate school. They agreed to let me take some master's level coursework in my first year to catch up with the other graduate students. It was during this year of playing catch-up, that I started working as a teaching assistant with Dr. Robert Beichner. He has the same enthusiasm for teaching that I had seen in my high school teachers. It was then that I was convinced I wanted to continue with graduate school so I could eventually teach at the collegiate level.

One of the responsibilities of graduate students at NC State is to interview perspective faculty members. During my second year in school, the physics department must have had an influx of money because we were seemingly interviewing perspective faculty members

every other day. When the physics department would bring in these perspective faculty members, they would have a senior faculty member escort them around for the day, and the senior faculty member that they chose the most was Dr. Dale Sayers. My first interactions with Dr. Sayers were all in this context. It was there that I saw his devotion to the university and his great character. When he let me know he was looking to hire on a new graduate student, I jumped at the chance to work for him. After I began working for him, my respect for him only grew. As I started into the experiments for my dissertation, he took a hands-off approach. He let me make mistakes and figure things out on my own, but he was always there to lend a helping hand during our weekly, and then—as time progressed—daily meetings. Though Dr. Sayers' passing on November 25, 2004 was a major blow to me—and to everyone else who knew him—personally and professionally, the lessons that he taught me about what it means to be a scientist and what it means to be a person of character will not be forgotten.

As I end my time as a graduate student and move on, I am a stronger person, I have a stronger faith, and I am certainly a better scientist. And I have a duty to pass my enthusiasm and wisdom on to the next generation of scientists.

ACKNOWLEDGEMENTS

I would like to thank God for all He has given me in my life. I do not think I would have been able to finish graduate school had I not had a solid foundation in Him. I know it is cliché to thank God at the end of something that turned out well, as this did for me, but I was reminded about the uncertainty of life during my time in graduate school, and, am incredibly thankful to be where I am now.

I would like to thank my family for being incredibly supportive during my time in graduate school. My time back home with my family has helped greatly in recharging me and keeping me motivated to finish school.

I would like to thank Dr. Dale Sayers for everything he did to get me where I am now. He showed great patience in dealing with me as I developed into a scientist. He showed great integrity in all he did.

I would like to thank Pastor Joe Sarver for the wisdom and humility that he showed as the pastor of my church. And, though his death was tragic, seeing him die with grace, and holding strong to what he believed, has made me—and everyone else who knew him—stronger.

I would like to thank Dr. Hans Hallen for stepping in as my advisor after Dr. Sayers' passing. There was some uncertainty as to what would come of my research, but he stepped in and provided me with a great deal of insight into my research and into what it means to be a scientist.

I would like to thank Dr. Zhong Zhong for stepping into an incredibly important role of providing insight into synchrotron research and DEI. Without Dr. Zhong's assistance, this work would not have been possible.

I would like to thank Dr. David Lalush and Dr. D. Rick Sumner for their insight into medical imaging and bone structure. I would have been lost without their help. Thanks as well to Dr. Etta Pisano for agreeing to join my committee after Dr. Sayers' passing. I would also like to thank Dr. Keith Weninger for agreeing to be on my committee. He played the important role of keeping me on task whenever he saw me working at Cup A Joe.

I would like to thank Dr. Miklos Kiss for helping me as I started into my DEI research. His insight into DEI and into IDL programming was instrumental in getting me acquainted with my research project.

I would like to thank Dr. Christopher Parham for his encouragement and help throughout my time doing DEI research. As the two North Carolina-based graduate students doing DEI research, we spent many hours together picking one another's brains, spurring one another on, and consuming caffeinated beverages.

I would like to thank all of my friends in Raleigh for supporting me throughout my time in school. Kate Snider has been an incredibly loyal friend and was there for me both after Pastor Sarver's and Dr. Sayers' death. Joe Lieb has been a wonderful roommate and a supportive friend. My friendships with Kristan Durham, Eve Van Devender, Jat and Julie Thompson, the Oglesby family, Austin Waters, Matthew Simmons, Gerard McNeill, Scott Andrews, Thurston Smith, and so many others have sustained me throughout my time in school. A special thanks to Cup A Joe, Global Village, Vineyard Café, Helios, and Third

Place for feeding my caffeine addiction. Thanks as well to David Baker, Joshua and Stacy Beun, Matthew Highland, Chris O'Shaughnessy, Grant Palmquist, Joshua Smith, and all of the other graduate students in physics at NC State.

I would like to thank Drs. Michael Paesler, Robert Beichner, Christopher Gould, Bruce Sherwood, Ruth Chabay, Albert Young, Richard Patty, David Aspnes, and Laura Clarke for their help with teaching, and their friendships throughout my time in graduate school. Last, but certainly not least, I would like to thank Jenny Allen, Ina Lunney, and Claudette Hathorne for their patience and assistance throughout my time in school. Their knowledge of the intricacies of NC State logistics saved me much pain and suffering.

Specific acknowledgements for the four different experiments are included in a separate subsection towards the end of each experiment's description.

TABLE OF CONTENTS

<u>LIST OF TABLES</u>	<u>XV</u>
<u>LIST OF FIGURES</u>	<u>XVI</u>
<u>LIST OF SYMBOLS AND ABBREVIATIONS</u>	<u>XVIII</u>
<u>1 INTRODUCTION</u>	<u>1</u>
<u>2 BACKGROUND</u>	<u>3</u>
2.1 DESCRIPTION OF DEI EXPERIMENTAL SETUP	3
2.1.1 X-RAY SOURCE	4
2.1.2 SOURCE TO HUTCH	5
2.1.3 ALUMINUM FILTERS	6
2.1.4 DOUBLE CRYSTAL MONOCHROMATOR	7
2.1.5 ION CHAMBER	10
2.1.6 IMAGING SAMPLE	11
2.1.7 ANALYZER CRYSTAL	11
2.1.8 DETECTORS	13
2.2 SUMMARY OF PAST DEI WORK	15
2.2.1 TWO-IMAGE DEI THEORY	15
2.2.2 WEDGE PHANTOM	17
2.2.3 DIFFRACTION ENHANCED COMPUTED TOMOGRAPHY THEORY	17

2.2.4	DEI CONTRAST	18
2.2.5	MULTIPLE IMAGE RADIOGRAPHY	19
2.2.6	APPLICATIONS OF DEI	20
2.3	THE STRUCTURE OF BONE	20
2.3.1	COLLAGEN FIBRILS AND DAHLITE CRYSTALS	20
2.3.2	MINERALIZED COLLAGEN FIBRILS	21
2.3.3	FIBRIL ARRAYS	21
2.3.4	PACKED FIBRIL ARRAYS	21
2.3.5	OSTEONS, LACUNAE, AND CANALICULI	22
2.3.6	TRABECULAR AND CORTICAL BONE	23
2.3.7	WHOLE BONE	24
2.4	REFERENCES	24
3	<u>IDENTIFICATION OF FATIGUE DAMAGE IN CORTICAL BONE BY DIFFRACTION ENHANCED IMAGING</u>	28
4	<u>DIFFRACTION ENHANCED IMAGING OF CONTROLLED DEFECTS WITHIN BONE, INCLUDING BONE-METAL GAPS</u>	35
4.1	ABSTRACT	36
4.2	INTRODUCTION	36
4.3	BACKGROUND	37
4.3.1	INTERFACE GAPS IN BONE IMPLANTS	37
4.3.2	X-RAY INTERACTION WITH MATTER	39
4.3.3	BRIEF REVIEW OF DEI EXPERIMENTS	39

4.3.4	DEI DESCRIPTION	40
4.3.5	EXPERIMENTAL JUSTIFICATIONS	43
4.4	MATERIALS AND METHODS	44
4.4.1	COMPUTER MODEL	44
4.4.2	BOVINE CORTICAL BONE EXPERIMENTS	45
4.4.3	STEPPED IMPLANT IN FEMUR	47
4.4.4	DEI EXPERIMENTAL CONFIGURATION	47
4.4.5	ACQUIRING DIFFRACTION ENHANCED IMAGES	48
4.4.6	ACQUIRING SR RADIOGRAPHS	49
4.4.7	IMAGE ANALYSIS	49
4.5	RESULTS	51
4.5.1	DRILL HOLE EXPERIMENT	51
4.5.2	SHAVED PIN EXPERIMENT	51
4.5.3	STEPPED IMPLANT EXPERIMENT	52
4.6	DISCUSSION	53
4.7	CONCLUSIONS AND FUTURE RESEARCH	55
4.8	ACKNOWLEDGEMENTS	55
4.9	REFERENCES:	57
5	<u>COMPARISON OF DIFFRACTION-ENHANCED COMPUTED TOMOGRAPHY AND MONOCHROMATIC SYNCHROTRON RADIATION COMPUTED TOMOGRAPHY OF HUMAN TRABECULAR BONE</u>	72
5.1	ABSTRACT	73
5.2	INTRODUCTION	74

5.3	BACKGROUND	74
5.3.1	ASSESSING TRABECULAR STRUCTURE	74
5.3.2	DIFFRACTION ENHANCED IMAGING EXPERIMENTS	75
5.3.3	DEI DESCRIPTION	76
5.4	MATERIALS AND METHODS	77
5.5	RESULTS	80
5.6	DISCUSSION	81
5.7	CONCLUSIONS	83
5.8	ACKNOWLEDGEMENTS	83
5.9	REFERENCES	84
6	<u>DEVELOPMENT OF A COMPUTER MODEL TO PREDICT ULTRA-SMALL</u>	
	<u>ANGLE X-RAY SCATTERING IN CORTICAL BONE</u>	<u>92</u>
6.1	ABSTRACT	93
6.2	INTRODUCTION	93
6.3	BACKGROUND	94
6.3.1	STRUCTURE OF PLEXIFORM BONE	94
6.3.2	MODEL DESCRIPTION	95
6.3.3	DEI DESCRIPTION	97
6.4	MATERIALS AND METHODS	99
6.4.1	GENERAL MODEL ATTRIBUTES	99
6.4.2	MODELING STRUCTURES IN PLEXIFORM BONE	100
6.4.3	DEI EXPERIMENT	101
6.5	RESULTS	104

6.5.1	GENERAL MODEL ATTRIBUTES	104
6.5.2	EXPERIMENTAL RESULTS	105
6.5.3	MODELING STRUCTURES IN PLEXIFORM BONE	105
6.6	DISCUSSION	106
6.7	CONCLUSIONS	107
6.8	ACKNOWLEDGEMENTS	108
6.9	REFERENCES	108
<u>7</u>	<u>CONCLUSIONS AND FUTURE WORK</u>	<u>116</u>
<u>8</u>	<u>REFERENCES</u>	<u>118</u>

LIST OF TABLES

	<i>Page</i>
Table 3.1 Summary of the difference between the scattering width of pre- and post-fatigue loaded bovine cortical bone samples (listed in manuscript simply as Table 1).....	33
Table 4.1 Summary of the contrast-to-noise ratio gains from the interface gap experiments.....	62

LIST OF FIGURES

	<i>Page</i>
Figure 2.1 Diagram of experimental setup at the National Synchrotron Light Source beamline X15A.....	3
Figure 2.2 Spectral distribution of x-ray intensity at the NSLS beamline X15A	5
Figure 2.3 Comparison of spectral distribution with and without aluminum filter	6
Figure 2.4 Comparison of pre- and post-filtered intensities for energies from 20 to 60 keV.....	7
Figure 2.5 Reflectivity profiles from analyzer crystal for a range of detuning amounts for the second monochromator crystal.	12
Figure 3.1 Diagram of experimental setup at NSLS beamline X15A (listed as figure 1 in the manuscript).....	32
Figure 3.2 Normalized plot of reflectivity profile and images from several analyzer crystal positions (listed as figure 2 in the manuscript).....	32
Figure 4.1 Diagram of the bone configurations for the drill hole and shaved pin experiments.....	63
Figure 4.2 Diagram and contact x-ray for the stepped titanium implant	64
Figure 4.3 Diagram of experimental setup at NSLS beamline X15A	65
Figure 4.4 Radiograph, peak, apparent absorption, and refraction images taken from the drill hole experiment.	66
Figure 4.5 Line profiles taken from the drill hole experiment.....	67
Figure 4.6 SR radiograph and DE images from the shaved pin experiment.....	68
Figure 4.7 Line profiles taken from the shaved pin experiment.....	69
Figure 4.8 SR radiograph and DE images from the stepped implant experiment	70
Figure 4.9 Line profiles from the stepped implant experiment.....	71
Figure 5.1 Diagram of the experimental setup at NSLS beamline X15A.....	88

	<i>Page</i>
Figure 5.2 Example apparent absorption DECT and SRCT slice images of trabecular bone.....	89
Figure 5.3 Comparison slice images of trabecular bone from apparent absorption DECT and refraction DECT	90
Figure 5.4 Example line profiles from small features in the trabecular bone slice images	91
Figure 6.1 Diagram of experimental setup at NSLS beamline X15A	111
Figure 6.2 Image of circles in a sample scatter region in the computer model and the histogram of the photon scattering angles for photons transmitted through sample scattering region	112
Figure 6.3 Plots of the scattering width as a function of four different varied parameters from the USAXS computer model	113
Figure 6.4 Plot of the normalized rocking curves through bone and through water.....	114
Figure 6.5 Plot of x-ray transmission as a function of energy for a variety of different bone thicknesses.....	115

LIST OF SYMBOLS AND ABBREVIATIONS

a	Lattice spacing
AFM	Atomic force microscopy
BV/TV	Ratio of bone volume to total volume
CNR	Contrast-to-noise ratio
CT	Computed tomography
DEI	Diffraction enhanced imaging
DECT	Diffraction enhanced computed tomography
d_{hkl}	Distance between planes $[h,k,l]$
E	Energy
FBP	Filtered back projection
F_H	Structure factor
$FWHM$	Full width at half maximum
h	Planck's constant
h,k,l	Miller indices
IDL	Interactive Data Language
I_H	Measured intensity in high-angle image
I_L	Measured intensity in low-angle image
I_R	Intensity in apparent absorption image
K	Polarization factor
MIR	Multiple image radiography

MRI	Magnetic resonance imaging
m_e	Electron rest mass
n	Index of refraction
NIST	National Institute of Standards and Technology
NLSL	National Synchrotron Light Source
r_e	Classical electron radius
$R(\theta)$	Analyzer crystal reflectivity curve or rocking curve
SAXS	Small-angle x-ray scattering
SR	Synchrotron radiation
SRCT	Synchrotron radiation computed tomography
$Tb.N$	Trabecular number
$Tb.Sp$	Trabecular spacing
$Tb.Th$	Trabecular thickness
TEM	Transmission electron microscopy
USAXS	Ultra-small angle x-ray scattering
V_c	Volume of a unit cell
v_e	Electron velocity

α	Angle of refracting interface with respect to incoming beam
δ	Difference from unity of the real part of the index of refraction
$\Delta\theta_z$	Angular deviation of refracted x-ray beam as measured by DEI
ε	Relative detuning of monochromator crystals
γ	Relativity gamma
λ	Wavelength of light
μ	Absorption coefficient
θ_B	Bragg angle
θ_H	High-angle side angular detuning amount
θ_L	Low-angle side angular detuning amount
ρ	Electron density
$\sigma_{\text{background}}$	Standard deviation of background
σ_{scatter}	Scatter width
ω	Darwin width

1 INTRODUCTION

Diffraction enhanced imaging (DEI) is a new medical imaging modality that is in its early stages of development and testing. Like conventional x-ray imaging, it has contrast that is due to absorption in the sample. But beyond the limits of conventional x-ray imaging, it can produce additional contrast from refraction and from rejecting or accepting x-rays that experience ultra-small angle x-ray scattering (USAXS). Though accepted values for x-ray absorption from biological tissues have been established, only recently have investigators began looking at the refraction and USAXS of x-rays from biological tissues. Of particular interest to this work, little has been done to characterize refraction and USAXS of x-rays from bone. Though divided into smaller experiments, the overall purpose of this work is to provide a starting point in the discussion of whether or not DEI could provide diagnostically useful information that is not available through conventional x-ray imaging.

This work starts with a presentation and description of the DEI experimental apparatus. The properties of the imaging system and how those properties affect the final image are the primary focus of this section. The foundational theory of DEI is then presented along with the results of several proof-of-principle experiments. The background then concludes with a look at the structure that is present within bone. The first experiment that is presented in this work looks at pre- and post-fatigue loaded bones to determine if DEI can detect a change in the scattering profile caused by microfractures within the bone structure. Though no consistent change in the ultra-small angle x-ray scattering (USAXS) profile was observed between the pre- and post-fatigue loaded samples, it was observed that there was measurable USAXS from the bone samples and that, even with the measurable USAXS,

there was refraction contrast for large structures (vascular channels) within bone. In the second experiment presented here, DEI was used to image bone samples with metal implants in them to determine if DEI presented contrast advantages over synchrotron radiation (SR) radiographs. DEI is shown to have contrast-to-noise ratio gains over SR radiograph for the imaging of bones with gap regions in them. In addition, the experimentally measured refraction and absorption values from DEI are compared with their predicted values from DEI theory. The experimentally measured refraction and apparent absorption signals are shown to be consistent with their theoretically predicted values. In the next experiment, diffraction enhanced computed tomography (DECT) and synchrotron radiation computed tomography (SRCT) of trabecular bone were acquired and the resulting image contrast and resolution were compared. DECT is shown to have contrast-to-noise ratio gains over SRCT. DECT is shown to have statistically significant resolution gains over SRCT as well. In the final experiment considered here, a computer model was developed to predict USAXS from cortical bone and the computer model results were compared to USAXS data obtained using DEI. It will be argued that the scattering widths, as predicted by the computer model, suggest that osteocyte lacunae cause the experimentally measured angular spreading of the x-ray beam.

This work concludes with a summary of the findings from the four experiments and a look towards what future work needs to be done to establish DEI as a useful imaging modality for characterizing bone.

2 BACKGROUND

2.1 Description of DEI experimental setup

In the following section the DEI experimental setup will be briefly described. The properties of the components will be considered along with the way in which they affect imaging with DEI. The focus will be on describing the experimental hutch, though the x-ray source will be considered. A diagram of the experimental setup for DEI is included as figure 2.1.

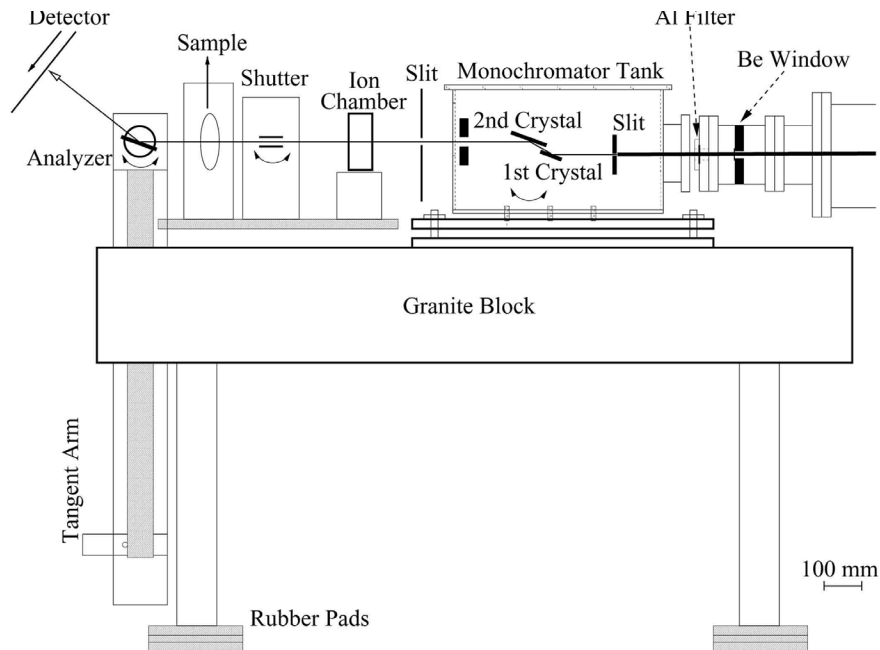


Figure 2.1. Diagram of experimental setup at the NSLS beamline X15A.

2.1.1 X-ray source

The x-ray source at the National Synchrotron Light Source (NSLS) beamline X15A is a bending magnet. Prior to insertion into the storage ring, electrons at the synchrotron are accelerated to near the speed of light. In the storage ring, the electrons are steered using bending magnets. Because the direction of the electrons is changing while being steered by the bending magnets, the electrons emit light (light emitted from accelerating charged particles is called synchrotron radiation). Because the electrons are traveling at relativistic speeds, the emitted light is in a forward facing cone that is tangent to the arc traversed by the electron. The opening angle of the emitted cone of light is approximately $1/\gamma$, where

$$\gamma \equiv \frac{1}{\sqrt{1 - \left(\frac{v_e}{c}\right)^2}} = \frac{E_{electron}}{m_e c^2} \quad \text{Equation 2.1}$$

and v_e is the speed of the electron, c is the speed of light, $E_{electron}$ is the energy of the electron (which is useful because synchrotrons are generally categorized by the electron energy, and not by the electron speed), and m_e is the rest mass of an electron. The rest energy, $m_e c^2$, of an electron is 0.511 MeV. The NSLS operates at 2.8 GeV, meaning $E_{electron}=2.8$ GeV, so the cone of light has an opening angle of approximately 180 μ radians (0.0105 degrees). Because the electron is emitting light the entire time it is being accelerated by the bending magnet, the emitted light cone traces out a line in the plane of the electron acceleration. For this reason, the width of the x-ray beam is much greater than the height of the beam when it is allowed into the experimental safety enclosure (hutch).

2.1.2 Source to hutch

The bending magnet source is separated from the experimental hutch by 16.3 m at the NSLS beamline X15A. Because the x-rays are diverging from the source and because the electrons are emitting light throughout the time they pass through the bending magnet, the bending magnet source generates an x-ray beam that measures approximately 10 cm wide by 3 mm high when it enters the experimental hutch. Between the source and the experimental hutch is a tube that is kept at ultra-high vacuum ($\sim 10^{-8}$ torr) to minimize attenuation of the beam between the source and the hutch. Because the tube is kept at vacuum, it has to be capped by a material that minimally absorbs x-rays. A beryllium window is placed at the end of the pipe. The intensity of light as a function of photon energy is included in figure 2.2.

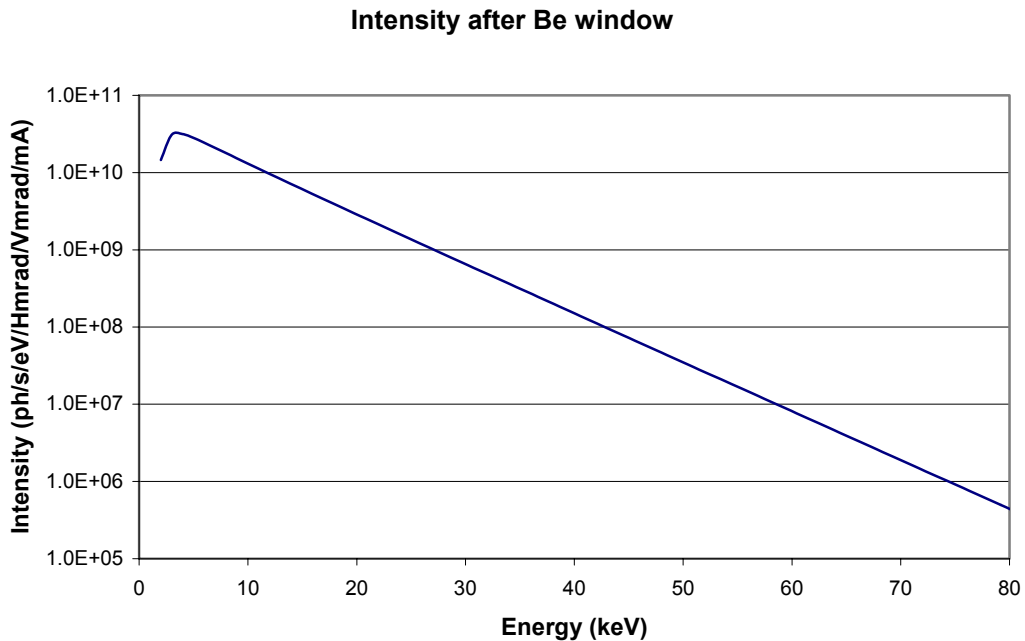


Figure 2.2. Spectral distribution of x-ray intensity at the NSLS beamline X15A

The power delivered to the hutch by the x-ray beam is the integral of the intensity curve.

2.1.3 Aluminum filters

In order to understand the importance of the aluminum filters, it is important to first consider the properties of the incident x-ray beam. From figure 2.2, it is clear that the intensity of light is very high for energies less than 10 keV, and because of that, a high percentage of the power delivered by the beam is from x-rays with energies under 10 keV. The properties of the monochromator crystal will be considered in the next section, but it is

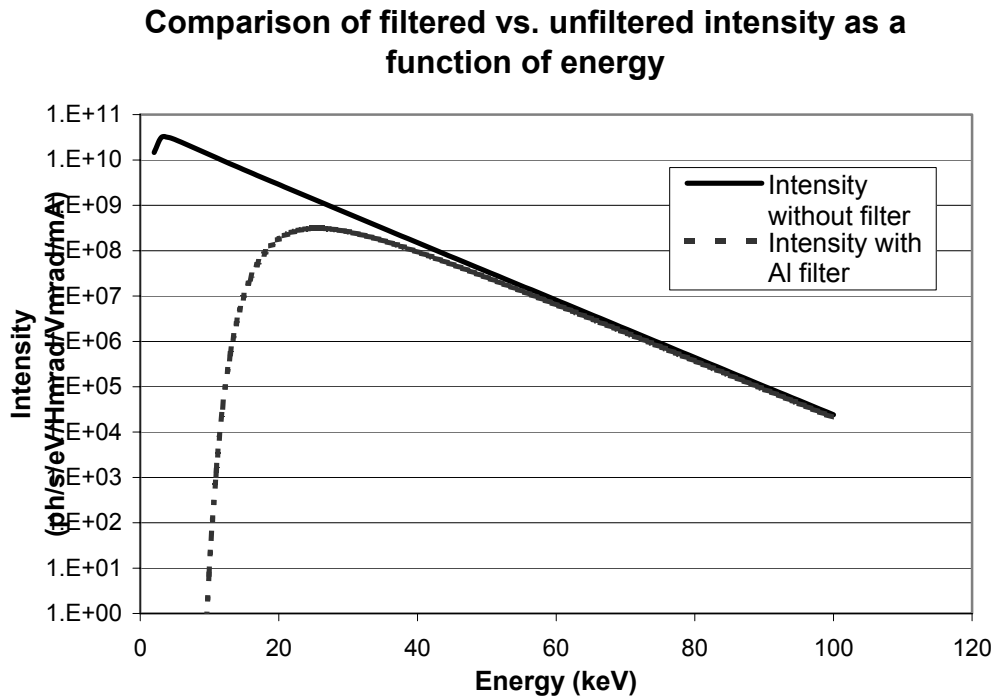


Figure 2.3. Comparison of pre- and post-filtered intensities.

sufficient for now to state that it is beneficial to minimize the power delivered to the monochromator. Because aluminum is highly absorbing for lower energy x-rays, it was used

to filter out lower energy x-rays while only minimally absorbing higher energy x-rays. With an aluminum filter thickness of 3mm, typically used when the desired x-ray energy for imaging is above 30 keV, the new spectral distribution of x-rays is shown in figure 2.3. Since the x-ray energies used for medical imaging start at around 20 keV, figure 2.4 displays the same plot as figure 2.3, but just for energies from 20-60 keV. From about 30 keV to 40 keV, the aluminum attenuates approximately half the incident x-rays.

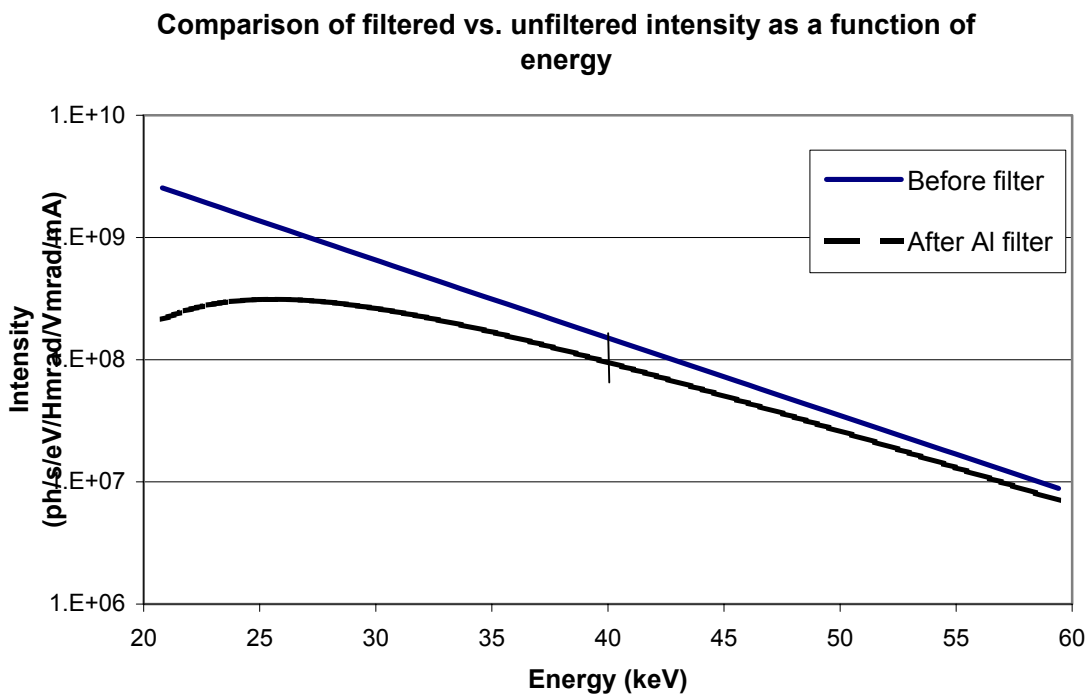


Figure 2.4. Comparison of pre- and post-filtered intensities for energies from 20 to 60 keV

2.1.4 Double crystal monochromator

The properties of the double crystal monochromator were considered in detail by Zhong et al,¹ so they will only be summarized here. The crystals are both perfect silicon

crystals. The first crystal measures 150 mm wide, 60 mm long, and 10 mm thick. The second crystal measures 150 mm wide, 90 mm long, and 10 mm thick. They are both cut so their [111] plane is parallel to the surface plane. To a first-order approximation, the crystals follow Bragg's law which states that

$$\lambda = 2d_{hkl} \sin \theta \quad \text{Equation 2.2}$$

where λ is the wavelength of the incident light, and θ is the angle the light makes with the diffracting plane. Since silicon crystals have a diamond structure with face-centered cubic symmetry,

$$d_{hkl}^2 = \frac{a^2}{h^2 + k^2 + l^2} \quad \text{Equation 2.3}$$

where a is the lattice spacing (which is 0.543 nm at room temperature) and h , k , and l are the Miller indices used to define the crystal plane (such as the [111] plane, where $h=k=l=1$). For the experiments described in this work, the x-ray energy used was primarily 40 keV which corresponds to a wavelength of approximately 0.031 nm. The experiments generally use the [333] reflection ($h=k=l=3$), so this means that the plane of the crystal surface has to be rotated so the beam makes a 8.5272 degree angle with the crystal surface. In addition to reflecting 40 keV x-rays at this angle, the crystal also has harmonic reflections. For the [333] plane in silicon, there are [111], [444], and [555] harmonics. These harmonics are at 1/3, 4/3, and 5/3, respectively, the energy of the [333] reflection (13.3, 53.3, and 66.7 keV). So, to a first-order approximation, the first monochromator crystal perfectly reflects 13.3, 40.0, 53.3, and 66.7 keV x-rays when its surface is at a 8.5272 degree angle with respect to the incoming polychromatic x-ray beam and x-rays of all other energies are either absorbed by or transmitted through the monochromator crystal. When determining the energy of light

reflected by the monochromator crystals, the divergence from the source must also be taken into account. Since the opening angle of the cone of x-ray light is 0.0105 degrees, the x-rays hit the crystal at an range of angles from $8.5272-0.0105/2$ to $8.5272+0.0105/2$ (8.5220 to 8.5325) degrees. From beam divergence alone, the $\Delta\theta/\theta$ is 0.001231 for when the crystal is at a 8.5272 degree angle with respect to the incoming polychromatic x-ray beam. This corresponds to a range of reflected wavelengths from 0.03098 to 0.031015 nm, or a $\Delta\lambda/\lambda$ of 0.001222. Because $E=hc/\lambda$ (where h is Planck's constant), $\Delta E/E$ is 0.001222.

Bragg's law and the x-ray beam divergence do not give a complete description of the x-ray interaction with the crystal though. Because the monochromator crystals are thick, perfect crystals, they reflect a very narrow range of energies surrounding the Bragg energies mentioned above. The crystal can equally be thought of as reflecting x-rays at a narrow range of angles surrounding the Bragg angle, θ_B . The width of that range of angles surrounding the Bragg angle is called the Darwin width. For the x-ray energies used for medical imaging, the Darwin width for the [333] reflection is on the order of 1-10 μ radians. The reflection curve for the perfect crystal is roughly box-shaped with a the box width equal to the Darwin width.^{2,3} The Darwin width, ω , decreases with an decrease in x-ray wavelength as

$$\omega = \frac{2\lambda^2}{\pi} \frac{V_c}{r_e} K F_H \sin(2\theta_B) \quad \text{Equation 2.4}$$

where V_c is the volume of a unit cell in the crystal, r_e is the classical electron radius, K is the polarization factor, and F_H is the structure factor.^{1,3} Equation 2.4 can be rewritten in terms of x-ray energy as

$$\omega = \frac{2(hc)^2}{\pi E^2} \frac{V_c}{r_e} K F_H \sin(2\theta_B) \quad \text{Equation 2.5}$$

which is more convenient here because x-ray energy is more commonly used than x-ray wavelength.

The x-ray beam that leaves the monochromator is affected by each of the above mentioned phenomena. The beam is the convolution of the incident beam, which has an intensity that is a function of x-ray energy and is diverging, with each of the reflectivity curves of the monochromator crystals. The reflectivity curves of the monochromator crystals are themselves a function of energy. The alignment of the monochromator crystals will be considered below.

2.1.5 *Ion chamber*

The transmitted x-rays then pass through an ion chamber. Since x-ray radiation is ionizing radiation, some x-rays will interact with the air in the ionization chamber causing electrons to be stripped from atoms. The ion chamber has top and bottom plates that generate a large electric field inside the chamber. The free electrons and positively charged ions can then flow towards the plates. The flow of ions and electrons is related to the amount of ionizing radiation that is passing through the chamber, so the measured current is proportional to the amount of ionizing radiation that is incident on the next—and most important—part of the imaging system, the sample. In medical imaging terms, the ion chamber can be used to determine the surface dose to the imaging sample.

2.1.6 *Imaging sample*

After passing through the ion chamber, the transmitted x-rays are incident on the imaging sample. The sample can interact with the incident x-rays in several ways. The different types of samples, and their interaction with the incident x-rays, are considered in detail in Chapters 3-6. What is important to consider for now is that the x-rays can be absorbed, scattered, or refracted within the sample and that each interaction mechanism is a function of energy. Because the x-ray beam that is incident on the sample is narrow along the vertical direction—the beam is about 3 mm high—the sample must be scanned through the x-ray beam in order to produce images that are greater than 3 mm high. The scanning stage that the sample is placed on allows the sample to be scanned through the fixed x-ray beam.

2.1.7 *Analyzer crystal*

The analyzer crystal is what sets DEI apart from all other types of x-ray imaging. As with the monochromator crystals, the analyzer crystal is a perfect silicon crystal with its surface plane parallel to the [111] plane. It measures 150 mm wide, 90 mm long, and 10 mm thick (the same as the second monochromator crystal). With no sample in the x-ray beam, the analyzer crystal can be tilted so the x-ray beam incident from the monochromator is at its Bragg angle. For the remainder of this work, the Bragg angle of the analyzer crystal will be where $\theta=0$, and all analyzer crystal angles are measured with respect to the Bragg angle. The analyzer crystal can be rotated to an angle, θ , with respect to its Bragg angle and the reflected intensity can be measured. The reflectivity profile of the analyzer crystal, $R(\theta)$, also referred to as the rocking curve, can be found by rotating the analyzer crystal and measuring the

reflected intensity as a function of the detuning angle, θ . The reflectivity profile is a combination of beam divergence from the source, the spectral intensity incident on the hutch, and the angular setting of the monochromator crystals (relative to the incident light and relative to each other). In mathematical terms, the reflectivity profile is the convolution of each of the imaging components.

The relative detuning of the monochromator crystals will now be considered. Plots of the analyzer reflectivity profile with the second monochromator crystal detuned from the first monochromator crystal by some amount, ε (meaning the second crystal is set such that the

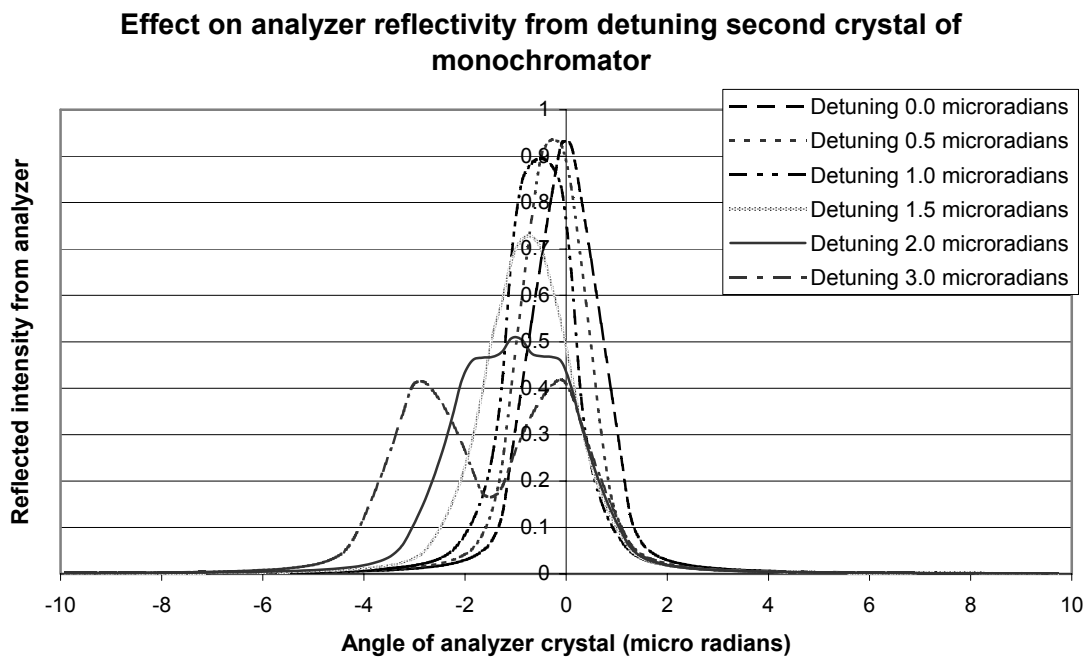


Figure 2.5. Reflectivity profiles from analyzer crystal for a range of detuning amounts for the second monochromator crystal.

beam from the first crystal is incident to the plane of the second crystal at some angle, $\theta_B + \epsilon$), are shown in figure 2.5. With slight detuning, the peak of the analyzer reflectivity profile shifts. With increasing amounts of detuning, there is a drop in peak reflectivity, an increase in the angular deviation of the peak, and an increase in the full-width half-maximum (FWHM) of the reflectivity curve. In practice, the effects of this monochromator crystal detuning have been observed as a drifting of the rocking curve. For the time scale of most of the imaging done in the subsequently described experiments, the observed drifting of the analyzer peak was around 0 to 0.4 μ radians.

All of the above considerations for the analyzer crystal are with no sample in the x-ray beam. With the sample in the beam, the analyzer crystal can be used to reject or selectively accept x-rays by rotating the analyzer crystal relative to the Bragg peak. The properties of the analyzer crystal, and how they are exploited to gain information about the sample, are considered in detail along with each of the subsequently described experiments.

2.1.8 Detectors

Three different detectors were used in the experiments described below. Each of the detectors gives a two-dimensional map of the intensity of x-rays incident on the detector. In order to measure the x-ray intensity, the detectors generally work in steps. In the case of the two different x-ray cameras that were used (Rad-Icon Shad-o-Box™ 2048 X-ray Camera and Photonic Science X-ray Imager VHR 150) a phosphor layer is coated onto a flat surface. The VHR 150 is coated with a phosphor that has 30 mg/cm² of Gd. X-rays that are incident on the surface are absorbed by the phosphor coating. The energy gained by the phosphor coating is then released in the form of visible light. For the Rad-Icon detector, the phosphor

material is coated directly on top of the CMOS detector. In the Photonic Science detector, fiber optic cables are placed on the side of the coating opposite the incident x-rays. The cables are then coupled to a CCD detector that measures the intensity of incident visible light. The intensity of the measured visible light is related to the intensity of the incident x-ray light. In the case of the image plate (Fuji HRV), the plate is covered with phosphor particles. When x-rays are incident on the phosphor particles, the particles transition to a metastable energy state. They stay in this metastable state until the image plate is read out using the image plate reader (Fuji BAS2500). The image plate reader works by shining a laser at the imaging plate which causes the phosphor to transition from the higher energy metastable state back to the lower energy ground state. In the process of returning to the ground state, the phosphor releases visible light, which is recorded by the image reader. The intensity of visible light released while reading the image plate is related to the intensity of x-rays incident on the image plate.

In order to better describe the detectors, the quantum efficiency needs to be taken into account. All three of the detectors use phosphor to translate the intensity of x-rays to the intensity measured by the camera. The quantum efficiency for measuring visible light is very high, so the camera and the scanner can be assumed to be close to 100% efficient at measuring the visible light released from the phosphor. What limits the quantum efficiency of the detectors then is the phosphor coating. In terms of incident x-ray intensity, the quantum efficiency is the percentage of the x-rays that are absorbed by the phosphor coating. Because the absorption coefficient of the phosphor is related to x-ray energy, the phosphor coating will have a quantum efficiency that is a function of the energy of the incident x-rays.

For the coatings used on the x-ray cameras, there is a quantum efficiency of approximately 20% for 40 keV x-rays.

2.2 Summary of past DEI work

In this section, key findings from several completed DEI experiments will be summarized. It will begin with looking at experiments that establish DEI, both theoretically and experimentally, as an imaging modality and will end with looking at applications of DEI.

2.2.1 Two-image DEI theory

In a study by Chapman et al,⁴ the theory behind two-image DEI was established. The theory will be considered in part here and in greater detail in the experiment descriptions in the subsequent sections. By taking images with the analyzer crystal detuned to its half intensity points (referred to at the high-angle and low-angle points) and combining them, it was shown that two new images could be created. It is important to understand what exactly is being measured at these half intensity points to have a firm grasp of the two-image DEI method. One can consider the analyzer crystal to act as an angular notch filter. When the crystal is detuned to one of its half intensity points, the notch filter accepts 50% of the x-rays that have no angular deviation. X-rays that have an angular deviation within the sample, can be directed towards or away from the angular acceptance of the notch filter. If the beam is directed towards the notch filter, then greater than 50% of the x-rays are reflected. If the beam is directed away from the notch filter, less than 50% of the x-rays are reflected. So the high-angle or low-angle images are combinations of the effects of absorption and refraction

within the sample. In the two image DEI method, the high-angle and low-angle images are combined in two different ways to separate the absorption information from the refraction information. One of these images is a scatter-reduced absorption image called an apparent absorption image. The apparent absorption image is calculated on a pixel-by-pixel basis using

$$I_R = \frac{I_L \left(\frac{dR}{d\theta} \right) \Big|_{\theta_H} - I_H \left(\frac{dR}{d\theta} \right) \Big|_{\theta_L}}{R(\theta_L) \left(\frac{dR}{d\theta} \right) \Big|_{\theta_H} - R(\theta_H) \left(\frac{dR}{d\theta} \right) \Big|_{\theta_L}} \quad \text{Equation 2.6}$$

where I_L and I_H are the measured low-angle and high-angle intensities, $R(\theta)$ is the reflectivity of the analyzer at an angle, θ , with respect to the Bragg angle, and $dR/d\theta$ is the slope of the rocking curve. All x-rays that were scattered outside of the angular acceptance range of the detuned analyzer crystal were not reflected by the analyzer crystal, so they were not measured by the detector. The high-angle and low-angle images can also be combined to form a refraction image. The refraction is calculated on a pixel-by-pixel basis using

$$\Delta\theta_z = \frac{I_H R(\theta_L) - I_L R(\theta_H)}{I_L \left(\frac{dR}{d\theta} \right) \Big|_{\theta_H} - I_H \left(\frac{dR}{d\theta} \right) \Big|_{\theta_L}} \quad \text{Equation 2.7}$$

where $\Delta\theta_z$ is the upward or downward (not leftward or rightward) angular deviation of the x-ray beam in the direction. For most biological specimens the angular deviation of the x-rays due to refraction were shown to be on the order of 10^{-6} - 10^{-7} radians.

In the derivation of the two DEI equations two major assumptions were made. The first major assumption is that the slope of the rocking curve is approximately linear near the analyzer crystal detuning angle, θ . This approximation allows for the reflectivity profile in

that region to be approximated using only the first two terms of the Taylor series expansion. The second major assumption is that there is little ultra-small angle x-ray scattering (USAXS) within the sample. If there is significant USAXS, then the x-ray beam diverges within the sample. Greater divergence of the x-ray beam means that the width of the reflectivity profile will increase and the slope of the rocking curve will decrease for a given analyzer crystal detuning angle.

2.2.2 *Wedge phantom*

As part of the test studies for the implementation of DEI at the NSLS and the Advanced Photon Source (APS), Zhong et al¹ describe the imaging of the a wedge phantom. The wedge phantom was made from an acrylic block that was cut to have slopes of -0.8 to +0.8 in steps of 0.2 with respect to the perpendicular to the beam direction. This means that the wedge phantom caused only an upward or downward deflection of the beam. The angular deviation of the beam due to refraction can be calculated by

$$\Delta\theta_z = 1.3 \times 10^{-4} \rho \lambda^2 \tan \alpha \quad \text{Equation 2.8}$$

where ρ is the electron density of the acrylic wedge (in g/cm³), λ is the x-ray wavelength (in nanometers), and α is the angle the incoming beam makes with the normal to the wedge surface. It was found that there was agreement between the theoretically predicted angular deviation and the angular deviation measured experimentally using DEI.

2.2.3 *Diffraction enhanced computed tomography theory*

Dilmanian et al⁵ showed that the two-image DEI method described by Chapman et al⁴ could be used in tomography mode to generate three dimensional information about the

sample. It was shown that, under the assumptions of DEI, the apparent absorption and refraction signals were linear and could therefore be reconstructed using filtered back projection (FBP). The apparent absorption projection images could be combined to generate a three dimensional map of the absorption coefficient within the sample. The refraction projection information could be combined to generate a three dimensional map of the out-of-plane gradient of the index of refraction. A cylindrical acrylic phantom was imaged in tomography mode. The phantom had drill holes cut into it at four different angles with respect to the cylinder axis. Each drill hole was filled with oil. The experimentally measured values for the out-of-plane gradient of the index of refraction and for the absorption coefficient were found to agree with their theoretically predicted values.

2.2.4 *DEI contrast*

In a study by Kiss et al⁶, DEI images of multiple different refracting cylinders were measured. The smaller radii cylinders were nylon wires (fishing line; diameters of 0.101, 0.2032, 0.5588, and 0.7112 mm). The largest radius cylinders were acrylic rods (diameters of 6.35, 12.7, and 25.4 mm). It was shown that DEI produces enhanced contrast as compared to comparably obtained synchrotron radiation (SR) radiographs. The contrast gains of DEI over SR radiography increased with a decrease cylinder diameter. It was also found that the experimentally obtained refraction and apparent absorption values agreed with the theoretically predicted values.

2.2.5 *Multiple image radiography*

Recently, Wernick et al^{7,8} have developed a variation of DEI called multiple image radiography (MIR) that generates attenuation, refraction, and ultra-small angle x-ray scattering images. Data collection in the MIR method is essentially the same as the process described to measure the intrinsic rocking curve of the system. The analyzer crystal is detuned by some angle, θ , and the sample is scanned through the x-ray beam. This is repeated multiple times for multiple analyzer angles. Corresponding pixels from the images taken at different analyzer crystal positions then represent the rocking curve through the corresponding section of the sample. If there is USAXS in the sample, then the rocking curve will be wider than the intrinsic rocking curve of the system. If there is refraction in the sample, then the peak of the rocking curve will shift with respect to the intrinsic peak. The MIR images are generated by mathematically processing the rocking curves on a pixel-by-pixel basis. The refraction for each pixel is the deviation of the centroid of the rocking curve from the centroid of the intrinsic rocking curve. The USAXS for each pixel is represented by the change in width of the rocking curve relative to the intrinsic rocking curve. The attenuation for each pixel is related to the total intensity measured from all the images (just adding all of the images together).

An experiment was performed in which the test object was an acrylic rod (refracting object) with varying numbers of paper strips (large amount of USAXS) behind it. Using the two-image DEI method to produce refraction images showed increasing errors, as compared to the theoretically predicted results, for increasing numbers of sheets of paper (error in refraction increased with the amount of scattering present). Though there was not exact

agreement between the MIR refraction image and the predicted refraction, the agreement was much better than the agreement between the two-image DEI refraction and predicted refraction.

2.2.6 Applications of DEI

Even though DEI is in its earlier stages of development as a medical imaging modality, it is already being used in several different medical imaging applications. The primary focus of DEI thus far has been towards its use in mammography⁹⁻¹⁴ where it has shown contrast advantages over SR radiography in both planar^{9,12} and tomography modes.¹³ DEI has also shown contrast advantages over SR radiography in imaging soft tissue in and around joints.¹⁵⁻²¹ It has also been used to image kidneys,²² thyroids,²³ and brain tumors.²⁴

2.3 The structure of bone

In a review article written by Wiener and Wagner,²⁵ seven different structure levels for bone are defined. In the following sections, each of these structure levels will be briefly described starting with the smallest structures (dahllite crystals and collagen fibrils) and ending with the largest structure level (whole bone). At each structure level, applicable current imaging modalities will be related.

2.3.1 Collagen fibrils and dahllite crystals

The smallest scale components that make up bone are Type I collagen, dahllite crystals, and water.²⁵ Individual collagen fibrils are cylindrical and measure approximately 300 nm in height and 2 nm in diameter.²⁶ The dahllite crystals are plates that measure on the

order of tens of nanometers high and wide and nanometers thick.²⁶ Transmission electron microscopy (TEM) or small-angle x-ray scattering (SAXS) must be used to measure these small structures.²⁵ Both these imaging types require the sample to be imaged *ex vivo* and require that the sample be very thin.

2.3.2 *Mineralized collagen fibrils*

The water, collagen, and dahllite from the first structure scale combine to form a composite material at the next structure scale. The mineralized collagen fibrils are cylindrical and approximately 100 nm in diameter and vary greatly in length.²⁷ Within the fibril, the long axis of the type I collagen aligns with the fibril axis. The dahllite crystals are interspersed between the collagen. The perpendicular to the plane of the crystal plate surface is perpendicular to the long axis of the cylindrical fibril. As with the last structure level, this structure level can only be measured *ex vivo* using TEM, SAXS, or atomic force microscopy (AFM).²⁵

2.3.3 *Fibril arrays*

The mineralized collagen fibrils pack closely together into fibril arrays. These arrays tend to align over a region and are best understood when considered at the next structure scale.

2.3.4 *Packed fibril arrays*

At this structure scale the fibril arrays of the previous structure scale are packed together in one of 3 types of ways. The weakest type of bone, woven-fibered bone, is comprised of randomly laid down fibril arrays.²⁸ There is no preferred orientation of the

fibril arrays,²⁵ but this type of structure has two main advantages over the subsequently described packed fibril arrays: it can be rapidly generated and it does not need to be laid down on existing bone.²⁸ In plexiform bone, the packed fibril arrays generally align with the long axis of the whole bone.²⁸ As with woven-fibered bone, plexiform bone can be laid down very rapidly, but plexiform has increased structural rigidity due to the greater fibril alignment.²⁸ Plexiform is primarily present in rapidly growing animals (e.g. cows²⁵). The Haversian canals that are present in osteonal bone (considered below) are surrounded by circular layers of aligned fibrils. Within a layer, the mineralized fibrils have a preferred orientation, but the preferred orientation varies from layer to layer in such a way as to make a plywood-like structure.^{25,26,28,29}

The alignment of the fibrils is generally measured using polarized light microscopy. Polarized visible light is incident on a thin-sectioned region of bone. A polarizing plate is placed on the opposite side of the bone and rotated to 90 degrees with respect to the incident light polarization. The fibrils that are aligned perpendicular to the plane of the sectioning do not rotate the polarization of the incident light so they appear black in the polarized light microscopy image. Fibrils that are aligned with the plane of the sectioning do rotate the polarization of the light so they are white in the image. Fibrils that are not either aligned parallel or perpendicular to the sectioning plane will appear gray in the image.

2.3.5 *Osteons, lacunae, and canaliculi*

Osteons are present primarily, and almost exclusively, in cortical bone (discussed below). They are regions that include a central vascular channel (50-90 μm in diameter²⁸), also referred to as a Haversian canal. Surrounding the Haversian canal are layers of aligned

mineralized fibrils called lamellae; the thickness of each lamellae is 3-7 μm .²⁸ In the more developed osteonal bone (secondary osteons), the individual osteons are separated by a cement line (\sim 1-5 μm thickness²⁸). Structures on this scale can be observed with a microscope. High resolution micro-CT can be used to visualize and characterize the Haversian canals.³⁰

Though they are not limited to osteonal bone, osteocyte lacunae and the canaliculi that connect them will be considered here. Osteocyte lacunae are roughly elliptical caverns that exist within bone. The major axis of the lacunae ellipse aligns with the mineralized collagen fibrils in the region.²⁸ When measured with the major axis of the lacunae perpendicular to the bone cross-section, the lacunae measure about 6 μm in diameter. The canaliculi are channels that extend outward from and connect the lacunae. These channels have been measured with AFM to be about 500 nm in diameter.³¹

2.3.6 *Trabecular and Cortical bone*

Whole bone is made up of two types of bone, trabecular and cortical. Distinguishing between the two types of bone can be done with the naked eye (though the bone has to be first removed from the animal). Trabecular bone, also called cancellous or spongy bone, consists of a spicular scaffolding. The individual trabeculae range from about 50 to 200 μm in diameter.³² Though visible with the naked eye, histological sectioning and microscopy or micro CT are usually used to assess trabecular structure. Cortical bone, also called compact bone, is mostly solid. Cortical bone runs along the shaft of long bones and provides structural rigidity. The structures present in cortical bone were considered in the previous sections.

2.3.7 Whole bone

This is the structure scale in which bone is considered as a whole (e.g. femur, tibia). The whole bone is a combination of all of the structures discussed in the previous sections. In vivo imaging of whole bone can be done with any one of many medical imaging modalities including planar x-ray imaging, CT, MRI, and ultrasound.

2.4 References

- ¹ Zhong Zhong, William Thomlinson, Dean Chapman, and Dale Sayers, "Implementation of diffraction-enhanced imaging experiments: at the NSLS and APS," *Nuclear Instruments and Methods in Physics Research A* **450**, 556 (2000).
- ² B. W. Batterman and H. Cole, "Dynamical Diffraction of X Rays by Perfect Crystals," *Reviews of Modern Physics* **36** (3), 681 (1964).
- ³ William H. Zachariasen, *Theory of x-ray diffraction in crystals*. (Dover Publications, New York, 1994).
- ⁴ D. Chapman, W. Thomlinson, R. E. Johnston, D. Washburn, E. Pisano, N. Gmur, Z. Zhong, R. Menk, F. Arfelli, and D. Sayers, "Diffraction enhanced x-ray imaging," *Physics in Medicine and Biology* **42** (11), 2015 (1997).
- ⁵ F. A. Dilmanian, Z. Zhong, B. Ren, X. Y. Wu, L. D. Chapman, I. Orion, and W. C. Thomlinson, "Computed tomography of x-ray index of refraction using the diffraction enhanced imaging method," *Physics in Medicine and Biology* **45** (4), 933 (2000).
- ⁶ M. Z. Kiss, D. E. Sayers, and Z. Zhong, "Measurement of image contrast using diffraction enhanced imaging," *Physics in Medicine and Biology* **48** (3), 325 (2003).
- ⁷ M. N. Wernick, O. Wirjadi, D. Chapman, Z. Zhong, N. P. Galatsanos, Y. Y. Yang, J. G. Brankov, O. Oltulu, M. A. Anastasio, and C. Muehleman, "Multiple-image radiography," *Physics in Medicine and Biology* **48** (23), 3875 (2003).

- 8 M. N. Wernick, O. Wirjadi, D. Chapman, Z. Zhong, O. Oltulu, and Y. Y. Yang, presented at the IEEE International Symposium on Biomedical Imaging, 2002 (unpublished).
- 9 E. D. Pisano, R. E. Johnston, D. Chapman, J. Geradts, M. V. Iacocca, C. A. Livasy, D. B. Washburn, D. E. Sayers, Z. Zhong, M. Z. Kiss, and W. C. Thomlinson, "*Human breast cancer specimens: Diffraction-enhanced imaging with histologic correlation - Improved conspicuity of lesion detail compared with digital radiography*," *Radiology* **214** (3), 895 (2000).
- 10 M. Z. Kiss, D. E. Sayers, Z. Zhong, C. Parham, and E. D. Pisano, "*Improved image contrast of calcifications in breast tissue specimens using diffraction enhanced imaging*," *Physics in Medicine and Biology* **49** (15), 3427 (2004).
- 11 M. O. Hasnah, C. Parham, E. D. Pisano, Z. Zhong, O. Oltulu, and D. Chapman, "*Mass density images from the diffraction enhanced imaging technique*," *Medical Physics* **32** (2), 549 (2005).
- 12 M. O. Hasnah, Z. Zhong, O. Oltulu, E. Pisano, R. E. Johnston, D. Sayers, W. Thomlinson, and D. Chapman, "*Diffraction enhanced imaging contrast mechanisms in breast cancer specimens*," *Medical Physics* **29** (10), 2216 (2002).
- 13 S. Fiedler, A. Bravin, J. Keyrilainen, M. Fernandez, P. Suortti, W. Thomlinson, M. Tenhunen, P. Virkkunen, and M. L. Karjalainen-Lindsberg, "*Imaging lobular breast carcinoma: comparison of synchrotron radiation DEI-CT technique with clinical CT, mammography and histology*," *Physics in Medicine and Biology* **49** (2), 175 (2004).
- 14 Dean Chapman, William Thomlinson, F. Arfelli, N. Gmür, Zhong Zhong, R. Menk, R.E. Johnston, D. Washburn, Etta Pisano, and Dale Sayers, "*Mammography imaging studies using a Laue crystal analyzer*," *Review of Scientific Instruments* **67** (9), (published on CD (1996)).
- 15 J. Li, Z. Zhong, R. Lidtke, K. E. Kuettner, C. Peterfy, E. Aliyeva, and C. Muehlemanll, "*Radiography of soft tissue of the foot and ankle with diffraction enhanced imaging*," *Journal of the American Podiatric Medical Association* **94** (3), 315 (2004).
- 16 S. Majumdar, A. S. Issever, A. Burghardt, J. Lotz, F. Arfelli, L. Rigon, G. Heitner, and R. H. Menk, "*Diffraction enhanced imaging of articular cartilage and*

- comparison with micro-computed tomography of the underlying bone structure,"* European Radiology **14** (8), 1440 (2004).
- ¹⁷ J. Mollenhauer, M. E. Aurich, Z. Zhong, C. Muehleman, C. C. Cole, M. Hasnah, O. Oltulu, K. E. Kuettner, A. Margulis, and L. D. Chapman, "*Diffraction-enhanced X-ray imaging of articular cartilage,*" Osteoarthritis and Cartilage **10** (3), 163 (2002).
- ¹⁸ C. Muehleman, M. Whiteside, Z. Zhong, J. Mollenhauer, M. Aurich, K. E. Kuettner, and L. D. Chapman, "*Diffraction enhanced imaging for articular cartilage,*" Biophysical Journal **82** (1), 470A (2002).
- ¹⁹ C. Muehleman, L. D. Chapman, K. E. Kuettner, J. Rieff, J. A. Mollenhauer, K. Massuda, and Z. Zhong, "*Radiography of rabbit articular cartilage with diffraction-enhanced imaging,*" Anatomical Record Part a-Discoveries in Molecular Cellular and Evolutionary Biology **272A** (1), 392 (2003).
- ²⁰ C. Muehleman, S. Majumdar, A. S. Issever, F. Arfelli, R. H. Menk, L. Rigon, G. Heitner, B. Reime, J. Metge, A. Wagner, K. E. Kuettner, and J. Mollenhauer, "*X-ray detection of structural orientation in human articular cartilage,*" Osteoarthritis and Cartilage **12** (2), 97 (2004).
- ²¹ A. Wagner, M. Aurich, N. Sieber, M. Stoessel, W. D. Wetzel, K. Schmuck, M. Lohmann, B. Reime, J. Metge, P. Coan, A. Bravin, F. Arfelli, L. Rigon, R. H. Menk, G. Heitner, T. Irving, Z. Zhong, C. Muehleman, and J. A. Mollenhauer, "*Options and limitations of joint cartilage imaging: DEI in comparison to MRI and sonography,*" Nuclear Instruments & Methods in Physics Research Section a-Accelerators Spectrometers Detectors and Associated Equipment **548** (1-2), 47 (2004).
- ²² L. Gang, Z. H. Chen, Z. Y. Wu, M. Ando, P. Lin, J. Y. Wang, and X. M. Jiang, "*Image quality dependence on thickness of sliced rat kidney taken by a simplest DEI construction,*" Nuclear Instruments & Methods in Physics Research Section a-Accelerators Spectrometers Detectors and Associated Equipment **548** (1-2), 200 (2004).
- ²³ H. S. Rocha, R. T. Lopes, P. M. Valiante, G. Tirao, I. Mazzaro, M. G. Honnicke, C. Cusatis, and C. Giles, "*Diagnosis of thyroid multinodular goiter using diffraction-enhanced imaging,*" Nuclear Instruments & Methods in Physics Research Section a-Accelerators Spectrometers Detectors and Associated Equipment **548** (1-2), 175 (2004).

- 24 K. A. Mannan, E. Schultke, R. H. Menk, K. Siu, K. Pavlov, M. Kelly, G. McLoughlin, T. Beveridge, G. Tromba, B. H. Juurlink, D. Chapman, L. Rigon, and R. W. Griebel, "*Synchrotron supported DEI/KES of a brain tumor in an animal model: The search for a microimaging modality*," Nuclear Instruments & Methods in Physics Research Section a-Accelerators Spectrometers Detectors and Associated Equipment **548** (1-2), 106 (2004).
- 25 S. Weiner and H. D. Wagner, "*The material bone: Structure mechanical function relations*," Annual Review of Materials Science **28**, 271 (1998).
- 26 S. Weiner and W. Traub, "*Bone-Structure - from Angstroms to Microns*," Faseb Journal **6** (3), 879 (1992).
- 27 P. Fratzl, H. S. Gupta, E. P. Paschalis, and P. Roschger, "*Structure and mechanical quality of the collagen-mineral nano-composite in bone*," Journal of Materials Chemistry **14** (14), 2115 (2004).
- 28 R. B. Martin and D. B. Burr, *Structure, function, and adaptation of compact bone*. (Raven Press, New York, 1989).
- 29 J. Black, R. Mattson, and Korostof.E, "*Haversian Osteons - Size, Distribution, Internal Structure, and Orientation*," Journal of Biomedical Materials Research **8** (5), 299 (1974).
- 30 D.M.L. Cooper, A.L. Turinsky, C.W. Sensen, and B. Hallgrímsson, "*Quantitative 3D analysis of the canal network in cortical bone by micro-computed tomography*," The Anatomical Record Part B: The New Anatomist **274B** (1), 169 (2003).
- 31 G. C. Reilly, H. F. Knapp, A. Stemmer, P. Niederer, and M. L. K. Tate, "*Investigation of the morphology of the lacunocanalicular system of cortical bone using atomic force microscopy*," Annals of Biomedical Engineering **29** (12), 1074 (2001).
- 32 T. M. Link, S. Majumdar, S. Grampp, G. Guglielmi, C. van Kuijk, H. Imhof, C. Glueer, and J. E. Adams, "*Imaging of trabecular bone structure in osteoporosis*," European Radiology **9** (9), 1781 (1999).

3 IDENTIFICATION OF FATIGUE DAMAGE IN CORTICAL BONE BY DIFFRACTION ENHANCED IMAGING

Written by D. M. Connor, D. Sayers, D. R. Sumner, and Z. Zhong

Published in *Nuclear Instruments and Methods in Physics Research Section A: Accelerators, Spectrometers, Detectors and Associated Equipment* on August 11, 2005



ELSEVIER

Available online at www.sciencedirect.com

SCIENCE @ DIRECT®

Nuclear Instruments and Methods in Physics Research A 548 (2005) 234–239

NUCLEAR
INSTRUMENTS
& METHODS
IN PHYSICS
RESEARCH

Section A

www.elsevier.com/locate/nima

Identification of fatigue damage in cortical bone by diffraction enhanced imaging

D.M. Connor^{a,*}, D. Sayers^a, D.R. Sumner^b, Z. Zhong^c

^aNorth Carolina State University, 2700 Stinson Drive, Box 8202, Raleigh, NC 27695, USA

^bRush Medical College, 600 South Paulina, Suite 507, Chicago, IL 60612, USA

^cBrookhaven National Laboratory, Building 725D, Upton, NY 11973, USA

Available online 22 April 2005

Abstract

In an effort to explore Diffraction Enhanced Imaging of bone tissue, experiments were performed to determine if it was possible to use Diffraction Enhanced Imaging to detect microdamage in bovine cortical bone. Measurements were made at the National Synchrotron Light Source where pre- and post-fatigue rocking curve widths of the bone were studied. The rocking curve widths were then compared. Since no consistent pattern of narrowing or broadening of the rocking curve emerged, it is likely that the ultra-small-angle X-ray scattering present in the bone overshadowed any additional changes to rocking curve caused by microdamage of the bone. Larger bone structures were able to be visualized which suggests that microdamage may be visualized with a higher resolution detector.

© 2005 Elsevier B.V. All rights reserved.

Keywords: Diffraction enhanced imaging; Darwin width; Fatigue damage; Microfracture; Rocking curve

1. Statement of problem

The purpose of this experiment was to determine if Diffraction Enhanced Imaging (DEI) could be used to detect microdamage that results from fatigue loading bovine cortical bone.

2. Background

2.1. Bone fracture

In order for fracture to occur in any material there needs to be small “seed” fractures called microfractures. Since microfractures can progress to macrofracture (“broken bone”) or can be symptomatic in and of themselves (“stress fracture”), an imaging modality that is capable of displaying microfractures, or at least signatures of them, would be a great help to the bone mechanics

*Corresponding author. Tel.: +1 919 515 5017;

fax: +1 919 515 7331.

E-mail address: dmcconnor@ncsu.edu (D.M. Connor).

research community. DEI is a new imaging modality that could potentially be capable of doing just that.

The existence and potential physiologic significance of microdamage accumulation in bone tissue has engendered considerable interest in the past 10 years. Part of the interest comes from the likely role of damage accumulation to the etiology of stress fractures [1–3]. In addition, microdamage accumulation may contribute to osteoporotic fractures [4] and loosening of dental or orthopedic implants [5]. Microdamage, in addition to having a direct role on the degradation of bone mechanical properties [6–8], may contribute to clinical fractures and implant loosening by inducing bone remodeling, which under certain circumstances could lead to failure [2]. Some current treatments for osteoporosis work by inhibiting bone remodeling and there are now a number of reports that these treatments lead to accumulation of microdamage, sometimes with associated decrements in bone mechanical properties [9]. There is good evidence that microdamage accumulation increases with age [3,10], is associated with decreased mechanical properties [6–8] and initiates bone remodeling [11–13].

Current methods of identifying and characterizing microdamage in bone include stiffness loss in mechanical testing [14,15] as well as a number of microscopic techniques [3,13]. Here, we propose to determine if DEI has the potential to serve as a non-invasive way of directly identifying and characterizing microdamage in bone. The DEI method currently depends on a synchrotron as the source of X-rays, but in principle could be adapted to work with conventional X-ray sources.

2.2. X-ray interaction with matter

When X-rays pass through an object they can interact in three ways. The first interaction mechanism, and the interaction mechanism for standard radiography, is photoelectric absorption. Regions of the object that are denser absorb more X-rays, so the contrast of standard radiography is due to variations in density and thickness. A second mechanism of interaction is refraction. As X-rays pass from a region of high electron density

to a region of lower electron density (or vice versa) the X-ray beam can deviate from its straight line path. The index of refraction for most biological structures differs from that of free space by one part in 10^6 . The deviation in the angle of the outgoing X-rays from that of the straight line path depends on the angle of the surface, the difference between indices, and the X-ray energy. For biological tissues, the deviations from straight line path are on the order of tenths of microradians. A third mechanism of interaction is scattering. As X-rays pass through the object, they can be elastically (coherently) or inelastically (incoherently) scattered. This scattering ranges from wide angle X-ray scattering (WAXS; on the order of tenths of radians to radians) to ultra-small angle X-ray scattering (USAXS; on the order of tenths of microradians). The amount of scattering that occurs in an object is related to the X-ray energy, to the density of the object, and to geometrical properties of the object. In standard radiography, scattering is considered to be a problem as it causes deterioration in image clarity. Since the only contrast mechanism of conventional radiography is absorption, any information contained in the scattering is lost.

2.3. DEI

Several papers have been written that relate the theory of DEI in far greater detail than will be presented here [16–18]. DEI was considered as a possible way of visualizing microdamage in bone because of its ability to filter out all but a very narrow range of angles and energies through the use of an analyzer crystal. In DEI, nearly collimated and monochromatic light exits the monochromator and passes through an object. A perfect Silicon analyzer crystal is placed between the object and the detector. For a given crystal reflection, e.g. [1 1 1], and energy, the analyzer crystal has a reflectivity profile, called a rocking curve, that is a function of angle and has a full-width at half-maximum (FWHM) that is highly energy dependent, but usually on the order of a few microradians [16,19]. The peak of the reflectivity profile is at the Bragg angle associated with that particular energy and reflection. The intrinsic

rocking curve of the whole system is the convolution of the analyzer reflectivity with the light leaving the monochromator. Since the analyzer crystal only reflects X-rays of a very narrow range of angles and energies, all X-rays that are outside that narrow range are no longer diffracted by the analyzer. If the analyzer is tuned at the Bragg peak, then any X-rays that are scattered by more than a few microradians are rejected by the analyzer. This property of DEI can be exploited in two different ways. First, it can be used to remove scattered X-rays from the image which should result in a sharper image. Secondly, and more importantly here, the analyzer can be tilted away from the peak and the intensity of X-rays scattered to this angle can be measured.

Placing an object in front of the X-ray beam before the analyzer crystal will result in a change in the measured rocking curve of the crystal. Consider an example of X-rays traversing through bone. Small scale structures in bone tissue (fibers, hydroxyapatite crystals, etc.) refract the X-rays. Since each X-ray is likely to be refracted by many of these structures as it passes through the bone, the overall effect on the X-ray beam is that there is a net angular spread about the straight-line path. This symmetric spreading of the beam due to multiple random refractions is referred to as ultra-small angle X-ray scattering (USAXS). In addition to the smaller scale structures, there are also structures within the bone that are larger than the imaging resolution of the system. Refraction from these larger structures should result in a measurable shift of the rocking curve peak angle.

The ultimate goal of this experiment was to take strides toward developing a system in which microfractures in bone can be visualized. Given the detector resolution, even ignoring further loss of resolution due to its intrinsic point spread function, one could not expect to be able to visualize the microfractures with the current system. What was proposed for this experiment was that the introduction of microdamage into bone through fatigue loading would cause a further broadening of the rocking curve width. Microdamage would be expected to introduce additional surfaces in the interior of the bone. It was hypothesized that the cumulative effect of the

X-ray beam passing through microdamage would be broadening of the rocking curve width.

3. Materials and methods

Machined bovine cortical bone samples were prepared at Rush University Medical College and shipped to the National Synchrotron Light Source (NSLS). The samples measured approximately 4 mm × 4 mm × 40 mm. The samples were secured to an aluminum sample holder, to minimize movement during the imaging process, and then placed in a water-filled Lucite container. Image sets were obtained for each of the bone samples. The bones were then shipped to Rush where some bones were fatigue loaded, while the control bones were not fatigue loaded. After the bones were shipped back to the NSLS, image sets were again obtained for all of the bones. The complete experiment took place in 4 parts over a 2-year period of time. For the first two parts one control bone and four fatigue-damaged bones were tested. For the third part, one control bone and ten fatigue-damaged bones were tested. For the fourth part, eight control bones and seven fatigue-damaged bones were tested. The total number of cortical bone samples for the study was 36 (control $n = 11$; fatigue damaged $n = 25$). The advantage of doing the experiments in steps was that it gave adequate time to process all of the data and time to make minor adjustments to the experiment.

All data were obtained at the NSLS Beamline X15A. A diagram of the experimental setup used to acquire all of the DEI and standard radiography data is included in Fig. 1. White light entered the hutch through the beryllium window. Aluminum filters reduced the intensity of light entering the monochromator, removing most of the lower X-ray energies. The monochromator then selected out 40 KeV X-rays using [3 3 3] diffraction. An ion chamber then read the radiation dose to which the sample was exposed during imaging.

For each image set, a group of 101 images was obtained. The sample was positioned such that both the ambient (water only) and bone (bone surrounded by water) were in the field of view. The sample position remained fixed during all of the

scans. Images were acquired for each analyzer crystal position as it was scanned from -10 to $+10 \mu\text{rad}$ in $0.2 \mu\text{rad}$ steps. The analyzer crystal was tilted using the tangent arm which has a minimum resolution of about $0.1 \mu\text{rad}$. The shutter was closed for the last 5 images in order to determine the detector background. The exposure

time for each image was 5 s. The detector that was used was a Rad-Icon Shad-o-Box™ 2048 X-ray Camera which generates 2048×1024 images at $50 \mu\text{m}$ resolution.

The rocking curve widths were obtained using Interactive Data Language (IDL). The portion of the image that contained data (approximately 500×30 pixels) was cut out of the original image and the rest was discarded. The median for each individual step of the scan was found in the y -, or vertical, direction. For each value in the x -direction the median y value for each step was fit to a Gaussian and the FWHM was found. The procedure was done both for the ambient and bone portion of each data set. Corrected rocking curve widths were calculated using Eq. (1).

$$\text{FWHM}_{\text{corrected}} = \sqrt{(\text{FWHM}_{\text{bone}})^2 - (\text{FWHM}_{\text{ambient}})^2} \quad (1)$$

4. Results and discussion

A sample of a rocking curve fit with images at several points on the rocking curve is included in

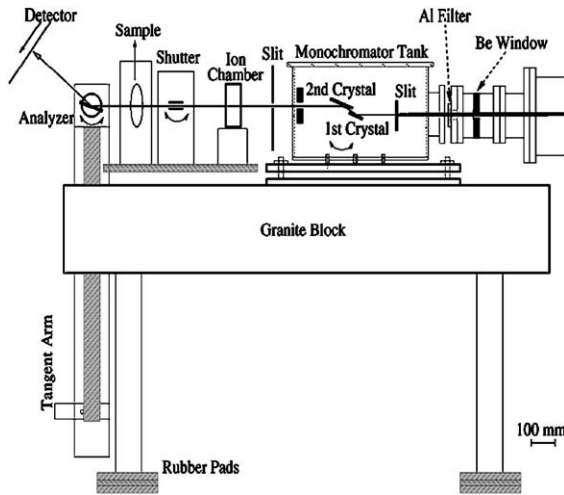


Fig. 1. Diagram of DEI experiment at NSLS Beamline X15A.

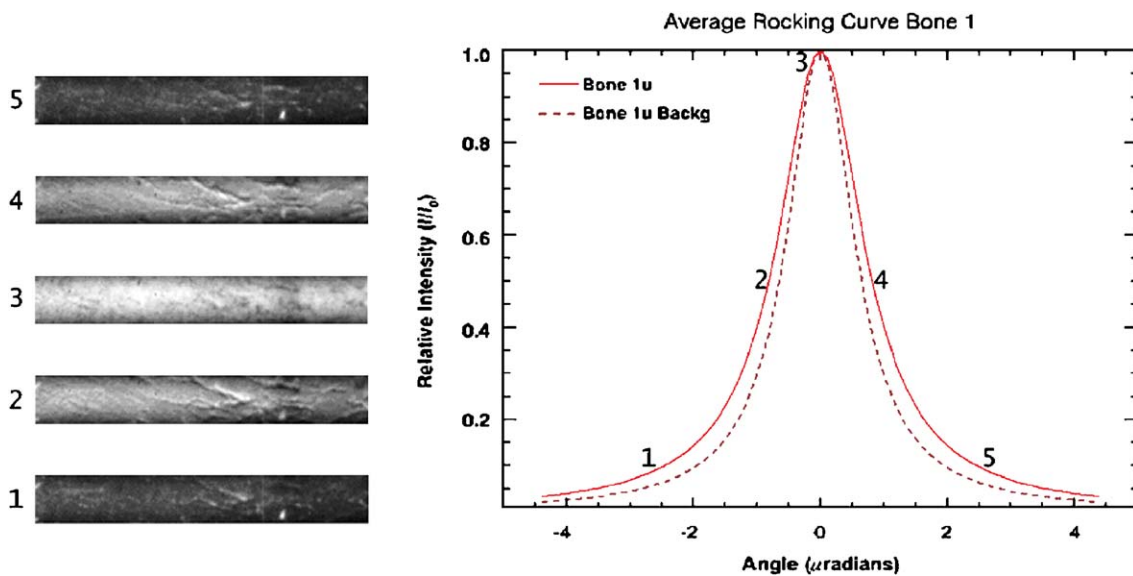


Fig. 2. Normalized plot of image intensity versus analyzer crystal angle relative to Bragg angle for pre-fatigue-loaded bovine cortical bone. Sample data for 5 different rocking curve angles are included on the left.

Fig. 2. The images are X-ray snapshots of the bone region of the image taken with the analyzer crystal tilted by an angle, θ , with respect to the Bragg angle. The graph includes the Gaussian fit to the rocking curve data. The peaks of both the ambient region and the bone region have been normalized. Note that, even though the sample bone had not yet been fatigue loaded, the rocking curve width of the bone is greater than the ambient rocking curve width. This broadening is expected because of USAXS occurring in the bone. There are clear structures (vascular channels) in the center of images 1, 2, 4, and 5. Refraction at the bone/vascular channel interface leads to an edge enhancement effect at the interface. The ability to image vascular channels with DEI is very important because they are objects that are close in size to the imaging resolution of the current DEI system. Since the ultimate goal of this experiment was to take strides toward developing a system in which microfractures can be visualized, these results suggest that, with a higher resolution detector, it should be possible to image microfractures.

Table 1 presents the mean results for the control and fatigue-loaded bones from each of the four experiments along with the mean results of all of the experiments combined. Experiment 1 showed narrowing of the rocking curve in three of the four

fatigued specimens from the first set of images (pre-fatigue loading) to the second set of images (post-fatigue loading) and narrowing in the control specimen from the first set of images to the second set of images. Experiment 2 showed an increase in the width of the rocking curve in all four fatigued specimens and the control specimen. Experiment 3 showed an increase in the width of the rocking curve in eight of nine fatigued specimens and the control specimen. Experiment 4 showed decreased rocking curve width in all seven fatigued specimens and all eight control specimens.

Even though all of the rocking curve widths tended to become narrower from image set 1 to image set 2 in experiments 1 and 4, this narrowing was less in the specimens that were fatigued, suggesting that there was evidence of relative broadening of the rocking curve in the damaged specimens in these two experiments. However, in experiments 2 and 3 the rocking curve width increased more in the controls than in the damaged specimens, suggesting that there was evidence of relative narrowing of the rocking curve in the damaged specimens in these two experiments. Thus, the data did not support the hypothesis that induction of fatigue damage would lead to broadening of the rocking curve width.

There are several factors that may have contributed to the measured rocking curve widths. Drifting of the monochromator crystal, which is caused by temperature changes in the crystal, will cause a net broadening or narrowing effect on the rocking curve width. Calculating the corrected FWHM of the rocking curve was done to ameliorate this, but possibly did not fully rectify the problem. A second factor that could have affected the results is physical change in bone hydration due to water seeping either into or out of the bone. A third possibility is physical deterioration of the bone during the experiments, but this does not seem likely since they were stored in a 10% formalin solution when they were not being imaged. Lastly, since the bones needed to be removed from the sample holder in order to be fatigue-loaded, it was not possible to fully preserve the bone's angular orientation with respect to the incoming X-ray beam between the two imaging sets.

Table 1
Adjusted differences of the FWHM between the first and second imaging sessions

Experiment dates	Type	<i>n</i>	Pre-fatigue loading minus post-fatigue loading (standard deviation)
07/02	C	1	0.27(0.15)
07/02	FL	4	0.18(0.32)
10/02	C	1	-0.33(0.27)
10/02	FL	4	-0.21(0.25)
02/03	C	1	-0.57(0.23)
02/03	FL	10	-0.14(0.18)
07/03	C	8	0.20(0.13)
07/03	FL	7	0.22(0.11)
Combined	C	11	0.12(0.15)
Combined	FL	25	-0.02(0.20)

Control bones are labeled C while fatigue loaded bones are labeled FL.

5. Conclusions and future research

Overall, the rocking curve width experiments did not confirm the hypothesis. No clear relationship between fatigue damage and rocking curve width could be determined. Several factors may have contributed in such a way as to make the results inconclusive. The experiments did have positive results in some respects. Images along the rocking curve clearly resolved objects of sizes that are within the resolving abilities of the detector. This, along with other DEI research [20,21], suggests that, with a higher resolution detector, microfractures within the bone could be directly imaged. This experiment also led to a redesign of the monochromator. Temperature controls have been added which greatly reduce the amount of crystal drift within the monochromator.

Acknowledgements

The authors would like to thank Dean Chapman, Miklos Kiss, and Christopher Parham for their contributions to our research. We would also like to thank the US Army whose Medical Research and Materiel Command funded this research through Grant number DAMD17-01-1-0811.

References

- [1] H. Frost, *J. Orthop. Sci.* 3 (1998) 272.
- [2] B. Martin, *J. Orthop. Res.* 13 (1995) 309.
- [3] M.B. Schaffler, K. Choi, C. Milgrom, *Bone* 17 (1995) 521.
- [4] D.B. Burr, M.R. Forwood, D.P. Fyhrie, R.B. Martin, M.B. Schaffler, C.H. Turner, *J. Bone Miner. Res.* 12 (1997) 6.
- [5] S.S. Huja, T.R. Katona, D.B. Burr, L.P. Garetto, W.E. Roberts, *Bone* 25 (1999) 217.
- [6] D.B. Burr, C.H. Turner, P. Naick, M.R. Forwood, W. Ambrosius, M.S. Hasan, R. Pidaparti, *J. Biomech.* 31 (1998) 337.
- [7] S.J. Hoshaw, D.D. Cody, A.M. Saad, D.P. Fyhrie, *J. Biomech.* 30 (1997) 323.
- [8] T.L. Norman, Y.N. Yeni, C.U. Brown, Z. Wang, *Bone* 23 (1998) 303.
- [9] T. Hirano, C.H. Turner, M.R. Forwood, C.C. Johnston, D.B. Burr, *Bone* 27 (2000) 13.
- [10] T.L. Norman, Z. Wang, *Bone* 20 (1997) 375.
- [11] V. Bentolila, T.M. Boyce, D.P. Fyhrie, R. Drumb, T.M. Skerry, M.B. Schaffler, *Bone* 23 (1998) 275.
- [12] D.B. Burr, M.R. Forwood, M.B. Schaffler, E.L. Radin, *J. Biomech.* 18 (1985) 189.
- [13] A. Parfitt, *Calcif. Tissue Int.* 53 (Suppl 1) (1993) S82.
- [14] D.R. Carter, D.M. Spengler, V.H. Frankel, *Acta Orthop. Scand.* 52 (1981) 481.
- [15] D.R. Carter, D.M. Spengler, V.H. Frankel, *J. Biomech.* 14 (1981) 461.
- [16] D. Chapman, et al., *Phys. Med. Biol.* 42 (11) (1997) 2015.
- [17] Z. Zhong, et al., *Nucl. Instr. and Meth. Phys. Res. A* 450 (2000) 556.
- [18] F.A. Dilmanian, et al., *Phys. Med. Biol.* 45 (4) (2000) 933.
- [19] W.H. Zachariasen, *Theory of X-ray Diffraction in Crystals*, Wiley, New York, 1945 vi, 255.
- [20] M.Z. Kiss, D.E. Sayers, Z. Zhong, *Phys. Med. Biol.* 48 (3) (2003) 325.
- [21] E.D. Pisano, et al., *Radiology* 214 (3) (2000) 895.

**4 DIFFRACTION ENHANCED IMAGING OF CONTROLLED DEFECTS
WITHIN BONE, INCLUDING BONE-METAL GAPS**

Written by D.M. Connor, D. Sayers, D.R. Sumner, and Z. Zhong

Submitted to *Physics in Medicine and Biology*

4.1 Abstract

Gap regions between a bone and an implant, whether existing upon insertion or developing over time, can lead to implant failure. Currently, planar x-ray imaging and CT are the most commonly used methods to evaluate the gap region. An alternative to these available clinical imaging modalities could help to better evaluate bone resorption. Previous experiments with Diffraction-Enhanced Imaging (DEI) have shown significant contrast advantages over monochromatic synchrotron radiation (SR) imaging. DEI and planar SR radiography images of bone samples with drill holes and gap regions of known geometry were acquired at the NSLS beamline X15A (Upton, NY, USA). The images acquired with DEI show measurable contrast-to-noise gains when compared to the images acquired using SR radiography.

4.2 Introduction

It is possible for interface gaps to develop in the region of a bone implant causing the implant to loosen and eventually fail. Interface gaps are a tissue layer between the bone and the implant that can compromise implant stability. Patients will often receive clinical x-rays to assess the development and growth of these interface gaps. Though these methods have shown to be helpful in assessing interface gap progression, a new medical imaging modality—diffraction enhanced imaging (DEI)—may prove to be more effective at evaluating interface gap progression. In previous studies, DEI has shown contrast advantages over monochromatic synchrotron radiation (SR) radiography. Of interest to the

present study, it has shown edge-enhancement as compared to planar SR radiography for the specific applications for which it has been tested. The synchrotron-generated x-ray beam used in SR radiography is highly collimated and can be tuned to the optimum x-ray energy for the subject being imaged. It has been shown both theoretically¹ and experimentally² to be superior to x-ray tube-based clinical x-rays. Thus, SR radiography, obtained at the same x-ray energy as DEI, is used as a gold standard for clinical x-rays. Few studies have specifically looked at the application of DEI to the imaging of gap regions in bone. As a preliminary probe into the possibility of using DEI to image interface gaps, the purpose of this experiment was to qualitatively and quantitatively compare images obtained using Diffraction Enhanced Imaging (DEI) with monochromatic, synchrotron radiation radiographs to determine if DEI has contrast advantages over SR radiography in imaging gap regions within bone. Towards this goal, three separate experiments were performed in which images were acquired of bone with holes drilled into them, bones with a shaved titanium pin press-fit into them, and a reamed human distal femur that had a stepped radius implant press-fit into it.

4.3 Background

4.3.1 Interface gaps in bone implants

Bone implants may be needed for a variety of reasons. Certain bone fractures require the use of pins or screws to stabilize the bone and aid in the healing process. Bone and cartilage degradation in joints can make joint replacement surgery (total joint arthroplasty) necessary. In total joint arthroplasty, affected regions of bone are removed and the remaining bone is reamed before the implant is fit into the reamed bone. Proper

alignment of the implant is needed to ensure that the mechanical loads encountered by the implant can be properly handled.³ Regardless of the type of implant used, the initial apposition of the implant to the bone is a necessary—but not sufficient—condition for its long-term success.³⁻⁵ If there is not initial apposition, an interface gap exists between the bone and the implant. Even if the implant initially abuts to and fixes with the surrounding bone, interface gaps can develop if there is net bone resorption at the bone-implant interface.^{3,6,7} These interface gaps allow relative motion between the implant and the bone. Any relative motion between the bone and the implant can cause wear debris from the implant to enter the interface gap region. This wear debris from the implant accelerates the resorption process.³⁻⁵

Two distinct geometries exist for interface gaps that develop through net bone resorption.³ In the linear geometry, the interface gap region runs parallel to the surface of the implant. In the expansive geometry, the interface gap extends outward from the implant into the surrounding bone. In order to assess the interface gap progression, clinical x-ray imaging is often used. Because the interface gap region is less absorbing than both the implant and the bone, it appears as either a dark line surrounding the implant (in the case of a linear gap region) or as a dark region extending outward from the implant (in the case of an expansive gap region). The key here is that the radiologist is assessing the development of the interface gap over time. A relatively narrow interface gap that is not expanding outward over time into the surrounding bone may pose little or no threat to the joint, whereas an interface gap that is expanding outward over time will likely be a threat to the survival of the artificial joint. Since the ability to assess the progression of the small interface gap into the

surrounding bone is key to assessing joint failure, a high-resolution, high-contrast imaging method that provides enhanced contrast at the edge between the bone and interface gap may prove to be more useful than clinical x-ray imaging.

4.3.2 X-ray interaction with matter

When x-rays pass through an object they can interact in four ways. Three of the interaction mechanisms, photoelectric absorption and coherent and incoherent scattering, are included in the absorption coefficient, μ , used in standard radiography and SR radiography. A fourth mechanism of interaction is refraction. Just as visible light can deviate from its straight line path when it encounters an interface between two different indices of refraction, transmitted x-rays passing from a region of high electron density to a region of lower electron density (or vice versa) deviate from their straight line path. The index of refraction at x-ray wavelengths for most biological structures differs from that of free space by one part in 10^6 . The deviation in the angle of the outgoing x-rays from that of the straight line path depends on the angle of the surface, the difference between indices, and the x-ray energy. For biological tissues, the deviations from straight line path are on the order of tenths of microradians.

4.3.3 Brief review of DEI experiments

Though still in its early stages of development and testing as a medical imaging modality, diffraction enhanced imaging (DEI) has shown much promise in several different areas of medical imaging. The largest thrust has been towards using DEI for mammography where it has shown contrast advantages over SR radiography for both planar⁸⁻¹³ and CT

imaging.¹⁴ DEI has also been shown to have contrast advantages over SR radiography for the imaging of soft tissue in joints.¹⁵⁻²² Other studies have been done testing DEI's effectiveness in imaging kidneys,²³ brain tumors,²⁴ thyroids,²⁵ and bone.²⁶ Three DEI experiments are particularly pertinent to the study presented here. Kiss et al²⁷ studied DE image contrast in comparison to SR radiography image contrast for test objects of a range of radii (three different radii fishing lines and one acrylic rod). For these refracting objects, DEI refraction images showed significant contrast gains over SR radiograph images, and the contrast gains increased with a decrease in test object radius. In another experiment by Connor et al,²⁶ it was shown that cortical bone has measurable ultra-small angle x-ray scatter (USAXS). The vulnerability of the two-image DEI method (discussed below) to USAXS and object orientation were presented in a series of papers by Wernick et al^{28,29} and Oltulu et al.³⁰ They showed that the measured refraction signal, as measured by the two-image DEI method, decreases with an increase in USAXS. They also showed that refraction contrast goes to zero—even for highly refracting objects—if they are oriented such that the refraction causes only a leftward or rightward angular deviation of the transmitted x-rays.

4.3.4 DEI description

4.3.4.1 General description of DEI

Several papers have been written that relate the theory of DEI in far greater detail than will be presented here.^{12,31-33} In DEI, nearly collimated and monochromatic x-rays exit the monochromator and pass through the subject. A perfect silicon analyzer crystal is placed between the subject and the detector. For a given crystal reflection, e.g. [111], and energy, the analyzer crystal has a reflectivity profile, called a rocking curve, that is a function of

angle and has a width that is energy dependent, but usually on the order of a few microradians.³⁴ The peak of the reflectivity profile is at the Bragg angle associated with that particular energy and reflection. Since the analyzer crystal only reflects x-rays of a very narrow range of angles and energies, all x-rays that are outside of that narrow range are not reflected by the analyzer. If the analyzer is tuned at the Bragg peak, then any x-rays that are scattered by more than a few microradians are rejected by the analyzer. The narrow reflectivity profile of the analyzer crystal can be exploited in two different ways. First, it can be used to remove scattered x-rays from the image which gives additional extinction contrast. Second, and more important here, the analyzer can be tilted away from the peak in order to extract refraction (described below) and scattering information from the sample as described in several DEI theory papers.^{9,12,28-30,32,35,36}

4.3.4.2 *Two-image DEI method*

Several different forms of DEI are now being used. In all DEI forms, the analyzer crystal is tilted to positions relative to its peak reflectivity position. For this study, the two-image DEI method, as described for planar imaging by Chapman et al,¹² is used. In the two-image method, the analyzer crystal is tilted to the high-angle and low-angles sides of the rocking curve that correspond to half the peak reflectivity. The DEI equations (presented below) convert the intensity at the high-angle and low-angle analyzer position into a measure of the angular deviation of the beam (in the case of the refraction image) and an image that combines absorption information with scatter-rejection (in the case of the apparent absorption image). In planar imaging, the refraction image represents the total angular deviation of the transmitted x-rays in the vertical direction as they pass through the sample—

upward deflection is white, while downward deflection is black and zero deflection is mid-tone gray. The apparent absorption image should be similar in appearance to a standard planar radiograph. The contrast in the apparent absorption image—as with the contrast in standard planar radiographs—is from variations in transmitted intensity due to absorption or scattering of the incident x-rays, though scattering objects will appear to be more absorbing in the apparent absorption image due to the additional extinction contrast. Under the approximation that the images are taken symmetrically about the rocking curve peak at the half-intensity points, the apparent absorption (I_r) and refraction ($\Delta\theta_z$) images can be calculated on a pixel-by-pixel basis using *equations* 4.1 and 4.2 (simplified versions of the DEI equations presented by Chapman et al¹²) below, where I_H and I_L are the pixel intensities in the high-angle and low-angle images, $R(\theta)$ is the reflectivity profile of the imaging system, θ is the angle of the analyzer crystal relative to the Bragg peak, and $dR/d\theta$ is the slope of the reflectivity profile.

$$I_R = I_H + I_L \quad \text{Equation 4.1}$$

$$\Delta\theta_z = \frac{1}{2 \left| \left(\frac{dR}{d\theta} \right) (\theta_H) \right|} \frac{I_H - I_L}{I_R} \quad \text{Equation 4.2}$$

4.3.4.3 DEI limitations

All forms of DEI have several limitations in common. As stated above, DEI is only sensitive to refraction that is either upward or downward in the diffraction plane of the analyzer (and not leftward or rightward, perpendicular to the diffraction plane). Because of this, refraction contrast is related to object orientation within the sample. There is an edge-

enhancement effect associated with DEI's additional refraction contrast, but because a planar image is an overlaying of all the refraction effects within the sample, objects one desires to see may be obscured by other refracting objects. There are other limitations specific to the two-image DEI method. The two-image DEI method assumes little USAXS in the sample,^{12,31,32} so USAXS from the sample will lead to a reduction in refraction contrast.^{10,36} Any mechanical vibrations or thermal variations cause a detuning of the analyzer from its set position. The two-image method assumes that images are taken symmetrically about the rocking curve peak. Since the reflectivity and the magnitude of the slope of the rocking curve are assumed to be equivalent at the two positions, any detuning of the system leads to a systematic error when calculating the refraction contrast using *equation 4.2*.

4.3.5 Experimental justifications

Prior to this experiment, it was not clear whether DE images, and specifically the refraction images, of bone would yield useful results because of USAXS in bone. To help determine if DEI might be a useful imaging modality for the assessment of interface gaps in bone, three separate experiments were performed. Since DEI of bone has not been thoroughly tested, a first experiment was performed with objects well within the resolving abilities of the imaging system. Since the detector used in the present study has a pixel size of 50 microns, the test objects (water-filled drill holes in bovine cortical bone) were chosen to be larger than 300 microns. The two goals in this experiment were to compare DE images to SR radiographs to determine if, for large refracting objects, the DEI refraction image had contrast-to-noise ratio (CNR) gains over the SR radiograph and to compare experimental data with the predicted absorption and refraction results from a computer model (presented

below). The second study was done to simultaneously mimic the conditions of a minimally-sized linear interface gap while also allowing the geometry to remain simple enough to reproduce with the computer model. For this study a shaved titanium pin was press-fit into drill hole in a machined piece of bovine cortical bone. As with the first experiment, the two goals were to compare image contrast and to compare experimental data with the computer model, but for this experiment the objects (the interface gaps) were sized near the imaging resolution of the detector.

In the third experiment, the intent was to recreate a more clinically relevant scenario. In this experiment, a human distal femur was reamed and a stepped radius cylindrical implant was press-fit into the femur (described in detail below). This represents a more physically meaningful scenario because the bone is of realistic diagnostic imaging thickness, the titanium implant is made of the same material and is the size of a real clinical implant, and the gap regions represent a realistic scenario in which the bone is overreamed prior to the press-fitting of the implant. The goal of this experiment was to compare images and CNR between the DE images and the SR radiograph. The computer model was not used for this experiment because of the complexity, in terms of the variation in shape and thickness, of the femur.

4.4 Materials and methods

4.4.1 Computer Model

A computer model of the experiment was developed to understand how the experimental results compare with theoretical predictions. It is based on a model described

by Kiss et al.²⁷ The original model was developed to predict the absorption and refraction due to an acrylic rod in air. It is a ray tracing program that measures both absorption and refraction of the ray along its path through the sample. It tracks the ray from the x-ray source, through the monochromator, through the sample, through the analyzer crystal (in the case of DEI), and to the detector. The underlying assumption of the model is that the bone, water, and titanium can be considered homogeneous materials, thus the only interactions that the x-rays experience with the materials are absorption in the bulk and refraction at the interfaces. The values used in the model for the mass-attenuation coefficient and electron density (used to calculate the index of refraction) for air, water, and cortical bone were taken from NIST's x-ray attenuation databases.³⁷ The value of the mass attenuation coefficient and electron density in the alloy were calculated by using individual mass attenuation coefficients of the elements and the weight percentages of the metals in the alloy. Since the model ignores the ultra small angle x-ray scattering (USAXS) caused by the non-homogeneity of the cortical bone,²⁶ it is expected that the results will not exactly match those obtained experimentally. In order to compare the theoretical results with those obtained experimentally, line profiles taken across the drill holes and interface gaps of the images were plotted with line profiles predicted by the computer model.

4.4.2 Bovine cortical bone experiments

Two experiments involving bovine cortical bone were performed. The bone samples measured approximately 4mm by 4mm by 40mm with square ends and rectangular sides. The sides were smoothed to minimize refraction effects at the surface of the bone. The sample for the drill hole experiment (figure 4.1a,b) had four parallel holes drilled

perpendicular to the axial direction. The holes were separated by about 5 mm and measured 0.37mm, 0.5mm, 0.75mm, and 1mm in diameter. For the shaved pin experiment (figure 4.1c,d), drill holes of radius 1mm were made through the center of the bone along the axial direction. Two titanium alloy (Ti6Al4V) pins of the same radius were obtained. This titanium alloy was chosen because it is commonly used for bone implants. Each pin was 1.0 mm in diameter and approximately 15 mm long. For pin 1 (figure 4.1c,d), 0.2mm was shaved off opposite sides of the rod along the length of the rod. For pin 2 (figure 4.1c,d), 0.1mm was shaved off opposite sides of the rod along the length of the rod. The pins were then press fit into 1 mm diameter drill holes. Thus, pin 1 had 200 μm gaps along opposite faces of the bone-implant interface and pin 2 had 100 μm gaps. The bone samples were placed so the x-ray beam went through the sample from left to right from the perspective in figure 4.1d (into the page from the perspective of figure 4.1c). The rotational orientation of both the drill hole and interface gap samples with respect to the imaging system correspond to the maximum upward or downward refraction. This means that this is the best-case scenario for DEI refraction contrast. The samples were secured to an aluminum sample holder, to minimize movement during the imaging process, and then placed in a water-filled acrylic container (TPP model # TP90075) to reduce refraction at the surface of the bone. The container had a flat front and back to limit the refraction at the boundary between the container and the surrounding air. The container measured 3.5 cm deep by 8.5 cm wide by about 9.0 cm high and acrylic wall thickness was 2 mm.

4.4.3 *Stepped implant in femur*

A femur was obtained from the Gift of Hope Organ and Tissue Donor Network. The distal aspect of the bone was drilled with progressively larger bits with the final 13 mm diameter cylindrical hole prepared with a 13 mm reamer. A 13mm diameter cylindrical titanium alloy (Ti6Al4V) implant was machined to have five different radius coaxial cylinders (see figure 4.2), so that 0 mm, 0.5 mm, 1.0 mm, 2.0 mm, and 3.0 mm gaps between the implant and the bone could be modeled. The distal femur was placed in a water-filled plastic container (Buddeez model # 00002R). The container measured approximately 8.5 cm deep by 18.0 cm wide by 18.0 high and had a wall thickness of approximately 2 mm.

4.4.4 *DEI experimental configuration*

The experimental configuration for DEI was implemented as described by Zhong et al.³¹. All data were obtained at the NSLS beamline X15A (figure 4.3). This beamline has a bending magnet source with high spectral brilliance up to an x-ray energy of approximately 60 keV. Polychromatic light from the bending magnet source entered the hutch through a beryllium window. Aluminum filters (total thickness of 3 mm) reduced the intensity of light entering the monochromator, removing most of the lower x-ray energies. This served to limit the power delivered to the monochromator and thereby minimizing the heat load. The double crystal silicon monochromator selected 40 keV x-rays using the [333] reflection. An additional benefit of the aluminum filters is that the 13.3 keV, [111] harmonic was effectively removed (intensity reduced by 99.99% by the filters) while the 40 keV x-rays were only minimally absorbed (only a 37% reduction in intensity). An ion chamber read the radiation dose to which the sample was exposed during imaging. A typical sample surface

dose incident on the sample and sample holder was 20 mrem for the bovine cortical bone experiments and 200 mrem for the stepped implant experiment. Depending on the overall bone thickness of the sample, the dose rate was adjusted by changing the sample scan speed, in order to achieve optimum exposure level on the detector. After passing through the ion chamber, the x-rays passed through the sample, which was on a sample stage that could be raised or lowered in 100 micron increments using a step motor. After passing through the sample, the x-rays still within the angular acceptance of the analyzer crystal are reflected. Like the monochromator, the analyzer crystal is a perfect silicon crystal which was also set to the 40 keV [333] reflection.

4.4.5 Acquiring diffraction enhanced images

For each image set, a subset of high angle, low angle and peak images were obtained. Prior to performing the experiments, the reflectivity profile, $R(\theta)$, was measured by measuring the intensity of the reflected x-ray beam as a function of angle, θ , with no sample along the x-ray beam path. The peak of the reflectivity profile, which is at the Bragg angle for a particular x-ray energy and reflection plane, is defined to be the $\theta=0$ point, so θ is always measured with respect to the reflectivity peak. Since the synchrotron source is a fixed source, samples larger than the beam must be moved through the beam. All scans were started with the beam passing through the acrylic container approximately 1 cm above the bone sample. The sample stage was raised until the beam was about 1 cm below the bone sample. As the sample was raised through the beam, the detector was lowered to account for the beam reflection from the analyzer crystal. The high angle images were obtained by first finding the peak of the analyzer crystal and then rotating it by +0.8 microradians. Low angle

images were obtained at -0.8 microradians from the peak. The angles (± 0.8 microradians) were chosen so the analyzer crystal was detuned to approximately half of its peak intensity where the rocking curve slope is the steepest, hence the most sensitivity to refraction. In order to determine the detector's dark current, four additional background images were obtained by keeping the shutter closed (no x-rays hitting the detector during the exposure time). The detector that was used for the bovine cortical bone experiments was a Rad-Icon Shad-o-Box™ 2048 X-ray Camera which generates 2048 by 1024 images with 50 micron pixel size. For the stepped implant experiment, a Photonic Science X-ray Imager VHR 150 with the a pixel size of 31.2 microns was used.

4.4.6 Acquiring SR radiographs

For SR radiography scans, an image-plate (Fuji HRV) was placed on the sample stage before the analyzer crystal. The x-ray energy and surface dose were as described above. The same region was scanned through the beam as in the DEI configuration. The image-plate was scanned with a Fuji BAS2500 image-plate reader. The image reader was set to read at 50 micron resolution. As a point of clarification, the intent of the SR radiographs is not to reproduce clinical imaging, but rather it is to hold constant as many variables (x-ray energy and dose) as possible to make the image comparisons more meaningful.

4.4.7 Image analysis

Image reconstruction was performed with Interactive Data Language (IDL). First, a median background image was created using the four background images. The background was then subtracted from each of the DE images. For the stepped implant experiment, the

images were resized to half their original size using the *rebin* function in IDL. The pixels in the resized image correspond to a 62.4 micron pixel size to better match the 50 micron pixel size of the SR images. The refraction and apparent absorption images were then created using *equations 1* and *2*. The bone regions were isolated in all of the images and comparison images were created. The contrast-to-noise ratio (CNR) was computed for each of the images. A window that included bone and a drill hole or interface gap was selected from each image. For the bovine cortical bone experiments, this region was approximately 15 pixels wide by 100 pixels high. For the stepped implant experiment, this region was 100 pixels wide by 455 pixels high. The median value was found across the width, so the 2D bone region was reduced to a 1D intensity profile. For the SR radiograph and apparent absorption images, the CNR is defined by *equation 4.3*, where I_{bone} is the intensity of the x-ray beam that passes through the thickest part of the bone (and not through a drill hole or interface gap), I_{max} is the maximum x-ray intensity through the region of interest. The standard deviation of the background, $\sigma_{background}$, for each image was calculated using the *stdev* function in IDL and applying it to a 50 by 50 pixel water region of the image.

$$CNR = \frac{|\ln(I_{bone}) - \ln(I_{min})|}{\sigma_{background}} \quad \text{Equation 4.3}$$

For the refraction images, the CNR was calculated according to *equation 4.4* where $\Delta\theta_{z,max}$ and $\Delta\theta_{z,min}$ are the maximum and minimum values, respectively, of the refraction profile across the drill hole or interface gap region of the image.

$$CNR = \frac{\Delta\theta_{z,max} - \Delta\theta_{z,min}}{\sigma_{background}} \quad \text{Equation 4.4}$$

4.5 Results

4.5.1 Drill hole experiment

A comparison of the SR radiograph, peak, apparent absorption, and refraction drill hole images is shown in Figure 4.4. A table of contrast-to-noise ratio (CNR) gains is included in Table 4.1. Plots of line profiles for the drill holes are included in Figure 4.5. Note that, since the measure of interest is the difference between absorption of bone and that of the water in the drill hole, the absorption of the bone is set to zero. If a region is less absorbing than bone, it will have a value less than zero. Setting the bone absorption to zero also allows the incident x-ray intensity to vary between the experiment and the model.

All four drill holes can be observed in each image (Figure 4.4). The refraction image clearly has the best drill hole contrast. This is due to the reversal of contrast in the refraction image. The contrast reversal occurs because the top half of the drill hole causes the x-rays to be refracted downward while the bottom half causes an upward refraction. Overall for the drill hole images, DEI images show large CNR gains over the SR radiograph images, an effect that is most evident for the smaller drill hole diameters with a CNR 17 times higher in the refraction image than in the SR radiographic image (Table 4.1).

4.5.2 Shaved pin experiment

For the shaved pin experiment, comparisons of the SR radiograph, peak, apparent absorption, and refraction interface gap images are included in Figure 4.6. The samples were oriented so that the gap regions should appear above and below the titanium pins. Table 4.1 also displays the comparison of CNR gains across the interface gap. Line profiles taken from

the images are compared to those predicted by the computer model and are included in figure 4.7.

As with the drill hole experiment, DEI shows substantial CNR gains when compared to the SR radiograph images. The interface gap region at the top and bottom edges of Pin #1 (200 μm gap) is barely visible in the SR radiograph, but appears very clearly in the refraction and apparent absorption images. The narrower interface gap surrounding Pin #2 (100 μm) cannot be seen in the SR radiograph image, but can be seen in the refraction and apparent absorption images and is most noticeable in the refraction image. The CNR gains for the DEI images confirm the visual observations (Table 4.1), where large gains in CNR were found with the DEI images compared to SR radiographs.

4.5.3 *Stepped implant experiment*

For the stepped implant experiment, comparisons of the SR radiograph, peak, apparent absorption, and refraction interface gap images are included in Figure 4.8. The samples were oriented so that the gap regions should appear above and below the titanium pins. Table 4.1 also displays the comparison of CNR gains across the top interface gap. Line profiles taken through the 1 mm gap region are included in Figure 4.9.

As with the other two experiments, DEI shows substantial CNR gains when compared to the SR radiograph images. As seen by Kiss et al,²⁷ the refraction contrast gains over the SR radiographs is greatest for smaller objects (where the object imaged here is the gap region). Unlike the first two experiments, the apparent absorption and peak images both show consistent CNR gains over the SR radiograph.

4.6 Discussion

The results of the drill hole experiment clearly point to DEI as producing increased contrast for bone gaps in comparison to SR radiographs. These results alone are limited in their medical significance, but they do suggest that DEI may be an effective imaging modality for bone. In particular, it suggests that the small angle scattering does not overwhelm the refraction gains. It is important to note here that, though the SR radiograph and apparent absorption line profiles match up consistently with their predicted values, the refraction profile peak values are consistently lower than predicted, meaning that the measured and predicted values of $\Delta\theta_z$ are different. This discrepancy will be considered below. What is important here is that, even though the amplitudes of the measured and predicted values are not completely consistent, the drill holes can be easily resolved and the drill hole diameters can be correctly measured.

In the shaved pin experiment, as in the drill hole experiment, there were significant differences between the predicted and measured values of $\Delta\theta_z$. The computer model used to predict $\Delta\theta_z$ accounts for many properties of the system (beam divergence, detector point spread function, etc.), but it does not take into account USAXS. This spreading of the beam is USAXS, which is symmetric about the rocking curve peak,²⁸⁻³⁰ results in loss of peak intensity and an increase in intensity on the wings of the rocking curve. Rocking curves taken of the x-rays after they have passed through bone show an increase in FWHM.²⁶ In theory, images taken symmetrically about the rocking curve peak should only be affected by the angular spread of intensity due to USAXS. Even though the high-angle and low-angle images contain USAXS, they should contain equal parts due to the symmetric nature of

USAXS. Thus the subtraction of the high-angle and low-angle images should eliminate the USAXS. In practice, crystal detuning makes taking images symmetrically about the peak nearly impossible. If, for example, the crystal is at +0.7 and -0.9 microradians for the high-angle and low-angle images respectively, then the high-angle image will contain more USAXS than the low-angle image, causing some scattering to remain in the refraction image. The net result of this effect is that USAXS can be falsely registered as refraction. The angular spreading and peak reduction caused by USAXS also can, in principle, cause a reduction or, in cases of large amounts of USAXS, elimination of the refraction signal. Scattering can cause a reduction in the measured value of $\Delta\theta_z$, up to the point that $\Delta\theta_z$ is indistinguishable from noise.

The importance of exact knowledge of $\Delta\theta_z$ can only be answered on an application-by-application basis. Multiple Image Radiography can be used to measure $\Delta\theta_z$ more accurately by acquiring images with the analyzer on multiple points on the rocking curve and fitting for the centroid of intensity versus angle, on a pixel-by-pixel basis.²⁸ Since for the interface gap experiment the primary concern was whether or not the interface gap can be resolved using DEI, it was not essential to have a quantitatively correct result for $\Delta\theta_z$. The significant finding here is not the value of the refraction angle in the interface gap region, but that the interface gap region can be visualized with significant CNR gains over SR radiography.

4.7 Conclusions and future research

These experiments are excellent tests of DEI contrast levels because the structures being imaged were well within the resolving abilities of the detector. DEI showed CNR gains over comparably obtained SR radiographs in all three experiments. Thus, DEI has contrast advantages over comparably obtained SR radiographs for this type of samples. The limited scope of this proof-of-principle study provides the impetus to explore DEI's full potential for imaging of bone-implant interface gaps with further research. This future research will require a significant reduction in the amount of drifting in the monochromator crystals, which should lead to more consistent DEI images and a better separation of refraction and apparent absorption effects. The current DEI system is a testing ground for a new medical imaging modality. Efforts are underway to develop a clinical DEI system. Clearly, a clinical system would need to be developed prior to this becoming a viable diagnostic medical imaging modality.

4.8 Acknowledgements

Thanks to the Gift of Hope Organ and Tissue Donor Network for providing the human bone samples. The authors would also like to thank the Department of the Army (Grant DAMD170110811) and North Carolina State University (Faculty Research and Professional Development grant). One of the authors (DRS) was partially supported by NIH grant AR48292. The authors also acknowledge Bob Urban, Department of Orthopedic Surgery, Rush University Medical Center, for help with the stepped implant model. Use of the X15A beamline at the National Synchrotron Light Source, Brookhaven National

Laboratory was supported by the U.S. Department of Energy contract No. DE-AC02-98CH10886, and by Brookhaven National Laboratory LDRD 05-057.

4.9 References:

- ¹ J. M. Boone and J. A. Seibert, "*A Comparison of Mono-Energetic and Poly-Energetic X-Ray-Beam Performance for Radiographic and Fluoroscopic Imaging*," *Medical Physics* **21** (12), 1853 (1994).
- ² R. E. Johnston, D. Washburn, E. Pisano, C. Burns, W. C. Thomlinson, L. D. Chapman, F. Arfelli, N. F. Gmur, Z. Zhong, and D. Sayers, "*Mammographic phantom studies with synchrotron radiation*," *Radiology* **200** (3), 659 (1996).
- ³ T. W. Bauer and J. Schils, "*The pathology of total joint arthroplasty - II. Mechanisms of implant failure*," *Skeletal Radiology* **28** (9), 483 (1999).
- ⁴ J. H. Boss, I. Shajrawi, and D. G. Mendes, "*The Nature of the Bone - Implant Interface*," *Medical Progress through Technology* **20** (3-4), 119 (1994).
- ⁵ C. S. Moucha, R. M. Urban, T. M. Turner, J. J. Jacobs, and D. R. Sumner, in *Joint replacements and bone resorption: pathology, biomaterials and clinical practice*, edited by A. Shanbhag, H. E. Rubash, and J. J. Jacobs (Marcel Dekker, New York, 2005 (in press)), pp. 13.
- ⁶ D. R. Sumner, in *The Adult Knee*, edited by J. J. Callaghan, A. G. Rosenberg, H. E. Rubash et al. (Lippincott Williams & Wilkins, Philadelphia, 2003), pp. 289.
- ⁷ E. M. Schwarz, D. Campbell, S. Totterman, A. Boyd, R. J. O'Keefe, and R. J. Looney, "*Use of volumetric computerized tomography as a primary outcome measure to evaluate drug efficacy in the prevention of peri-prosthetic osteolysis: a 1-year clinical pilot of etanercept vs. placebo*," *Journal of Orthopaedic Research* **21** (6), 1049 (2003).
- ⁸ M. O. Hasnah, Z. Zhong, O. Oltulu, E. Pisano, R. E. Johnston, D. Sayers, W. Thomlinson, and D. Chapman, "*Diffraction enhanced imaging contrast mechanisms in breast cancer specimens*," *Medical Physics* **29** (10), 2216 (2002).
- ⁹ M. O. Hasnah, C. Parham, E. D. Pisano, Z. Zhong, O. Oltulu, and D. Chapman, "*Mass density images from the diffraction enhanced imaging technique*," *Medical Physics* **32** (2), 549 (2005).

- 10 M. Z. Kiss, D. E. Sayers, Z. Zhong, C. Parham, and E. D. Pisano, "*Improved image contrast of calcifications in breast tissue specimens using diffraction enhanced imaging*," *Physics in Medicine and Biology* **49** (15), 3427 (2004).
- 11 E. D. Pisano, R. E. Johnston, D. Chapman, J. Geradts, M. V. Iacocca, C. A. Livasy, D. B. Washburn, D. E. Sayers, Z. Zhong, M. Z. Kiss, and W. C. Thomlinson, "*Human breast cancer specimens: Diffraction-enhance imaging with histologic correlation - Improved conspicuity of lesion detail compared with digital radiography*," *Radiology* **214** (3), 895 (2000).
- 12 D. Chapman, W. Thomlinson, R. E. Johnston, D. Washburn, E. Pisano, N. Gmur, Z. Zhong, R. Menk, F. Arfelli, and D. Sayers, "*Diffraction enhanced x-ray imaging*," *Physics in Medicine and Biology* **42** (11), 2015 (1997).
- 13 Dean Chapman, William Thomlinson, F. Arfelli, N. Gmür, Zhong Zhong, R. Menk, R.E. Johnston, D. Washburn, Etta Pisano, and Dale Sayers, "*Mammography imaging studies using a Laue crystal analyzer*," *Review of Scientific Instruments* **67** (9), (published on CD (1996)).
- 14 S. Fiedler, A. Bravin, J. Keyrilainen, M. Fernandez, P. Suortti, W. Thomlinson, M. Tenhunen, P. Virkkunen, and M. L. Karjalainen-Lindsberg, "*Imaging lobular breast carcinoma: comparison of synchrotron radiation DEI-CT technique with clinical CT, mammography and histology*," *Physics in Medicine and Biology* **49** (2), 175 (2004).
- 15 J. Li, Z. Zhong, R. Lidtke, K. E. Kuettner, C. Peterfy, E. Aliyeva, and C. Muehlemanll, "*Radiography of soft tissue of the foot and ankle with diffraction enhanced imaging*," *Journal of the American Podiatric Medical Association* **94** (3), 315 (2004).
- 16 S. Majumdar, A. S. Issever, A. Burghardt, J. Lotz, F. Arfelli, L. Rigon, G. Heitner, and R. H. Menk, "*Diffraction enhanced imaging of articular cartilage and comparison with micro-computed tomography of the underlying bone structure*," *European Radiology* **14** (8), 1440 (2004).
- 17 J. Mollenhauer, M. E. Aurich, Z. Zhong, C. Muehleman, C. C. Cole, M. Hasnah, O. Oltulu, K. E. Kuettner, A. Margulis, and L. D. Chapman, "*Diffraction-enhanced X-ray imaging of articular cartilage*," *Osteoarthritis and Cartilage* **10** (3), 163 (2002).

- 18 C. Muehleman, M. Whiteside, Z. Zhong, J. Mollenhauer, M. Aurich, K. E. Kuettner, and L. D. Chapman, "*Diffraction enhanced imaging for articular cartilage*," Biophysical Journal **82** (1), 470A (2002).
- 19 C. Muehleman, L. D. Chapman, K. E. Kuettner, J. Rieff, J. A. Mollenhauer, K. Massuda, and Z. Zhong, "*Radiography of rabbit articular cartilage with diffraction-enhanced imaging*," Anatomical Record Part a-Discoveries in Molecular Cellular and Evolutionary Biology **272A** (1), 392 (2003).
- 20 C. Muehleman, S. Majumdar, A. S. Issever, F. Arfelli, R. H. Menk, L. Rigon, G. Heitner, B. Reime, J. Metge, A. Wagner, K. E. Kuettner, and J. Mollenhauer, "*X-ray detection of structural orientation in human articular cartilage*," Osteoarthritis and Cartilage **12** (2), 97 (2004).
- 21 C. Muehleman, D. R. Sumner, and Z. Zhong, "*Refraction effects of diffraction enhanced radiographic imaging - A new look at bone*," Journal of the American Podiatric Medical Association **94** (5), 453 (2004).
- 22 A. Wagner, M. Aurich, N. Sieber, M. Stoessel, W. D. Wetzel, K. Schmuck, M. Lohmann, B. Reime, J. Metge, P. Coan, A. Bravin, F. Arfelli, L. Rigon, R. H. Menk, G. Heitner, T. Irving, Z. Zhong, C. Muehleman, and J. A. Mollenhauer, "*Options and limitations of joint cartilage imaging: DEI in comparison to MRI and sonography*," Nuclear Instruments & Methods in Physics Research Section a-Accelerators Spectrometers Detectors and Associated Equipment **548** (1-2), 47 (2004).
- 23 L. Gang, Z. H. Chen, Z. Y. Wu, M. Ando, P. Lin, J. Y. Wang, and X. M. Jiang, "*Image quality dependence on thickness of sliced rat kidney taken by a simplest DEI construction*," Nuclear Instruments & Methods in Physics Research Section a-Accelerators Spectrometers Detectors and Associated Equipment **548** (1-2), 200 (2004).
- 24 K. A. Mannan, E. Schultke, R. H. Menk, K. Siu, K. Pavlov, M. Kelly, G. McLoughlin, T. Beveridge, G. Tromba, B. H. Juurlink, D. Chapman, L. Rigon, and R. W. Griebel, "*Synchrotron supported DEI/KES of a brain tumor in an animal model: The search for a microimaging modality*," Nuclear Instruments & Methods in Physics Research Section a-Accelerators Spectrometers Detectors and Associated Equipment **548** (1-2), 106 (2004).

- 25 H. S. Rocha, R. T. Lopes, P. M. Valiante, G. Tirao, I. Mazzaro, M. G. Honnicke, C. Cusatis, and C. Giles, "*Diagnosis of thyroid multinodular goiter using diffraction-enhanced imaging*," Nuclear Instruments & Methods in Physics Research Section a-Accelerators Spectrometers Detectors and Associated Equipment **548** (1-2), 175 (2004).
- 26 D. M. Connor, D. Sayers, D. R. Sumner, and Z. Zhong, "*Identification of fatigue damage in cortical bone by diffraction enhanced imaging*," Nuclear Instruments & Methods in Physics Research Section a-Accelerators Spectrometers Detectors and Associated Equipment **548** (1-2), 234 (2004).
- 27 M. Z. Kiss, D. E. Sayers, and Z. Zhong, "*Measurement of image contrast using diffraction enhanced imaging*," Physics in Medicine and Biology **48** (3), 325 (2003).
- 28 M. N. Wernick, O. Wirjadi, D. Chapman, Z. Zhong, N. P. Galatsanos, Y. Y. Yang, J. G. Brankov, O. Oltulu, M. A. Anastasio, and C. Muehleman, "*Multiple-image radiography*," Physics in Medicine and Biology **48** (23), 3875 (2003).
- 29 M. N. Wernick, O. Wirjadi, D. Chapman, Z. Zhong, O. Oltulu, and Y. Y. Yang, presented at the IEEE International Symposium on Biomedical Imaging, 2002 (unpublished).
- 30 O. Oltulu, Z. Zhong, M. Hasnah, M. N. Wernick, and D. Chapman, "*Extraction of extinction, refraction and absorption properties in diffraction enhanced imaging*," Journal of Physics D-Applied Physics **36** (17), 2152 (2003).
- 31 Zhong Zhong, William Thomlinson, Dean Chapman, and Dale Sayers, "*Implementation of diffraction-enhanced imaging experiments: at the NSLS and APS*," Nuclear Instruments and Methods in Physics Research A **450**, 556 (2000).
- 32 F. A. Dilmanian, Z. Zhong, B. Ren, X. Y. Wu, L. D. Chapman, I. Orion, and W. C. Thomlinson, "*Computed tomography of x-ray index of refraction using the diffraction enhanced imaging method*," Physics in Medicine and Biology **45** (4), 933 (2000).
- 33 M N; Wirjadi Wernick, O; Chapman, D; Zhong, Z; Galatsanos, N; Yang, Y; Brankov, J; Oltulu, O; Anastasio, M; Muehleman, C, "*Multiple-image radiography*," Physics in Medicine and Biology **48**, 3875 (2003).

- ³⁴ William H. Zachariasen, *Theory of X-ray diffraction in crystals*. (J. Wiley, New York, 1945).
- ³⁵ E. Pagot, P. Cloetens, S. Fiedler, A. Bravin, P. Coan, J. Baruchel, J. Hartwig, and W. Thomlinson, "A method to extract quantitative information in analyzer-based x-ray phase contrast imaging," *Applied Physics Letters* **82** (20), 3421 (2003).
- ³⁶ K. M. Pavlov, C. M. Kewish, J. R. Davis, and M. J. Morgan, "A variant on the geometrical optics approximation in diffraction enhanced tomography," *Journal of Physics D-Applied Physics* **34** (10A), A168 (2001).
- ³⁷ J. H. Hubbell and S. M. Seltzer, *Tables of X-Ray Mass Attenuation Coefficients and Mass Energy-Absorption Coefficients (version 1.3)*, Retrieved April, 2004, from <http://physics.nist.gov/xaamdi>.

Table 4.1 Summary of CNR gains from drill hole, shaved pin, and stepped implant experiments

	Gain (CNR_i/CNR_{radio})		
	Peak	App. Ab.	Refraction
Drill Hole 1 (370 μ m)	0.5	0.4	17.6
Drill Hole 2 (500 μ m)	1.2	0.7	16.8
Drill Hole 3 (750 μ m)	1.6	0.6	13.4
Drill Hole 4 (1000 μ m)	1.3	0.7	11.7
Pin 1- 200 μ m top gap	4.6	0.2	6.4
Pin 1- 200 μ m bottom gap	0.2	0.4	13.0
Pin 2- 100 μ m top gap	13.1	4.3	172.0
Pin 2- 100 μ m bottom gap	2.3	1.1	6.9
Stepped implant 0.5 mm top gap	22.6	10.1	24.8
Stepped implant 1.0 mm top gap	3.3	2.6	5.6
Stepped implant 2.0 mm top gap	4.2	3.9	2.0
Stepped implant 3.0 mm top gap	3.5	3.2	1.9

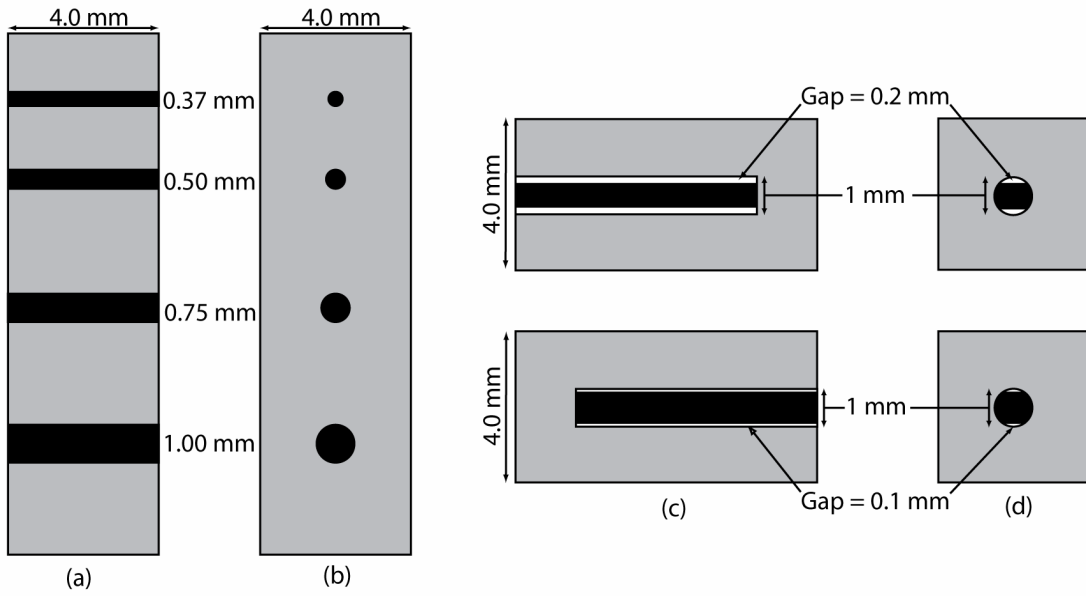


Figure 4.1 Diagram of the bone configurations for (a), (b) the drill hole experiment and (c), (d) the shaved pin experiment.

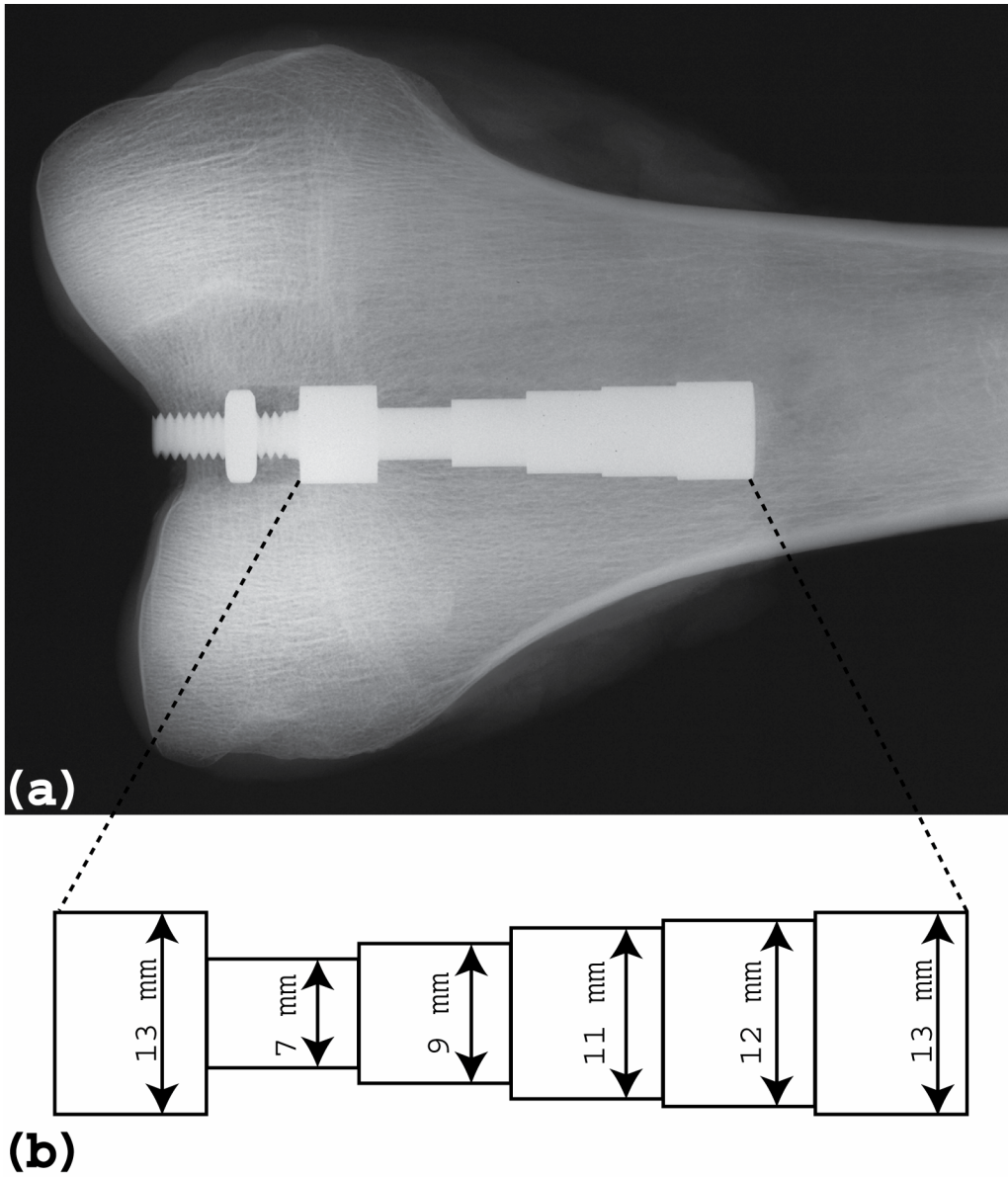


Figure 4.2 (a) A contact x-ray (Faxitron) of the distal femur with the stepped titanium implant inserted. Taken with Kodak Oncology Film (Kodak Portal Pack PP-L) using a tube source set to 110 KVP for 30 second. (b) A diagram of the stepped titanium implant.

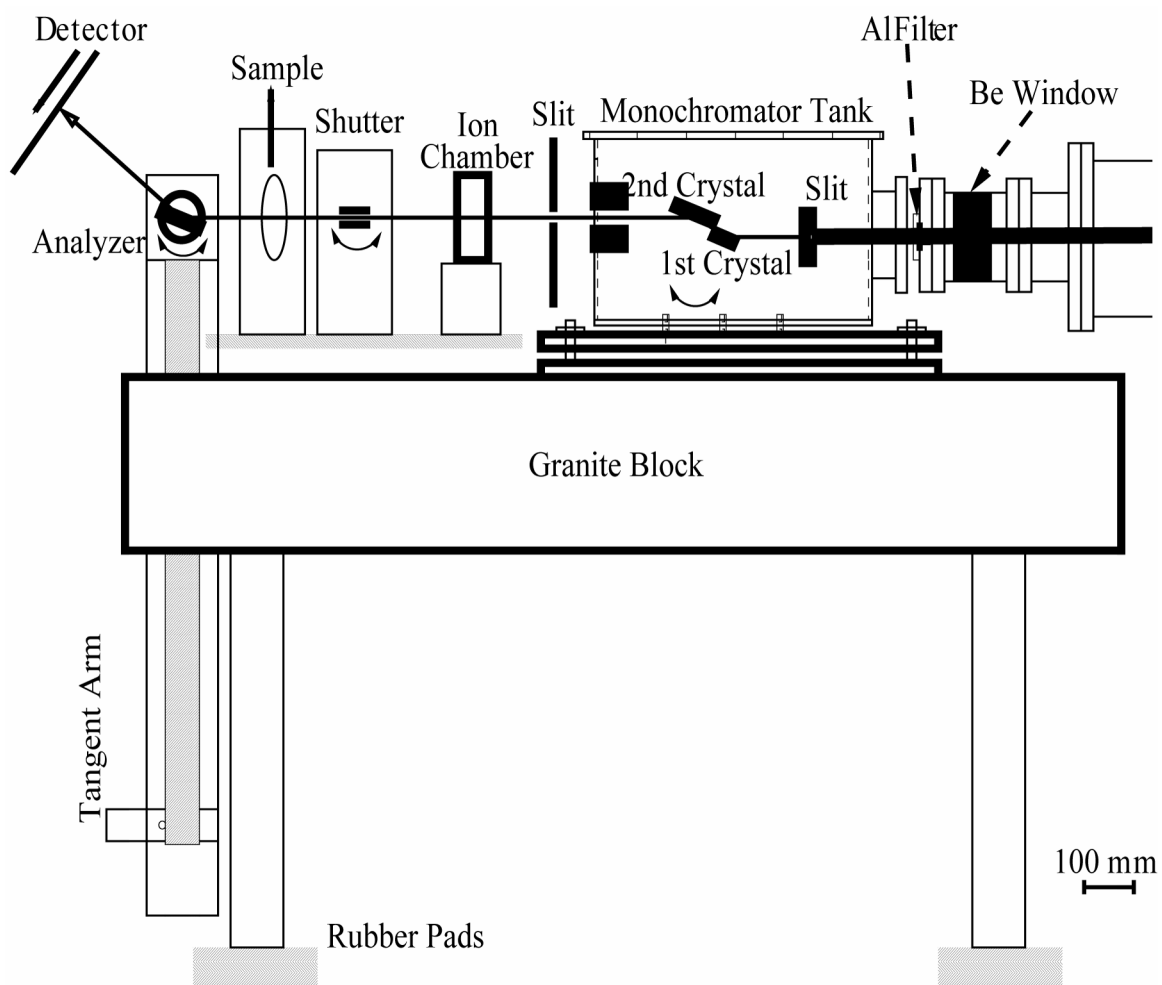


Figure 4.3 Diagram of the DEI experimental configuration at NSLS beamline X15A.

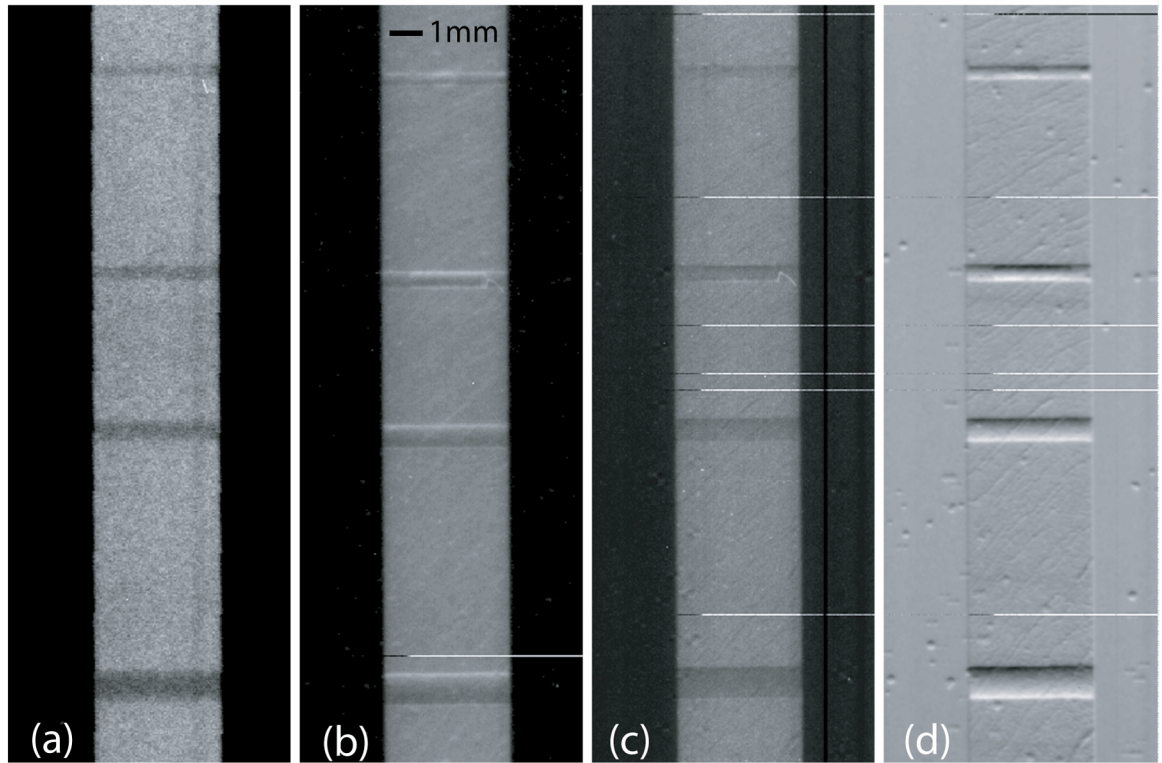


Figure 4.4 Images from the drill hole experiment. Images (a)-(d) are the radiograph, peak, apparent absorption, and refraction images, respectively, taken from the drill hole experiment.

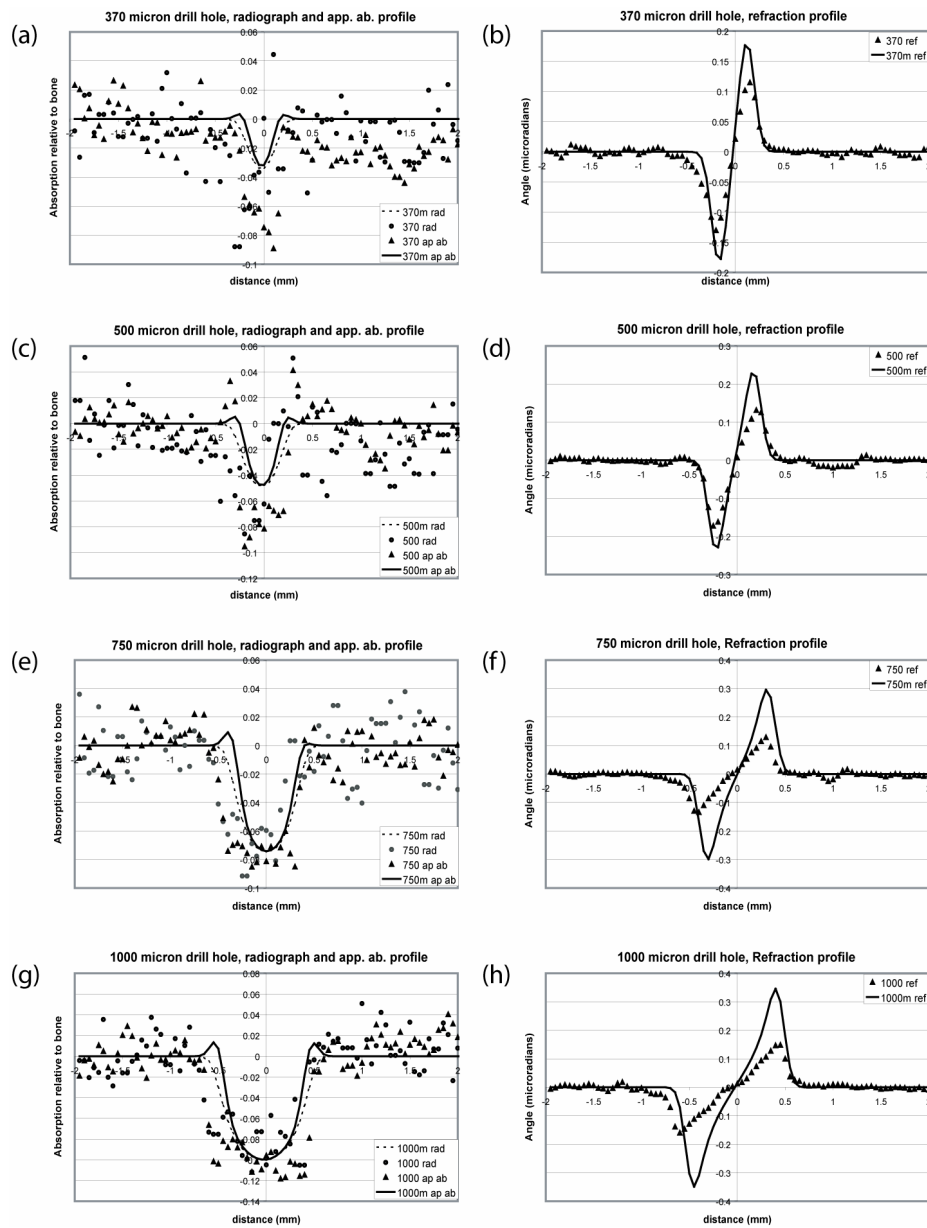


Figure 4.5 Line profiles taken from the drill hole experiment. Profiles (a), (c), (e), and (g) are the predicted (dashed line) and experimental (dots) SR radiograph results as well as the predicted (solid line) and experimental (triangles) apparent absorption results for the 370, 500, 750 and 1000 micron drill holes respectively. Profiles (b), (d), (f), and (h) are the predicted (solid line) and experimental (triangles) refraction results for the 370, 500, 750 and 1000 micron drill holes respectively.

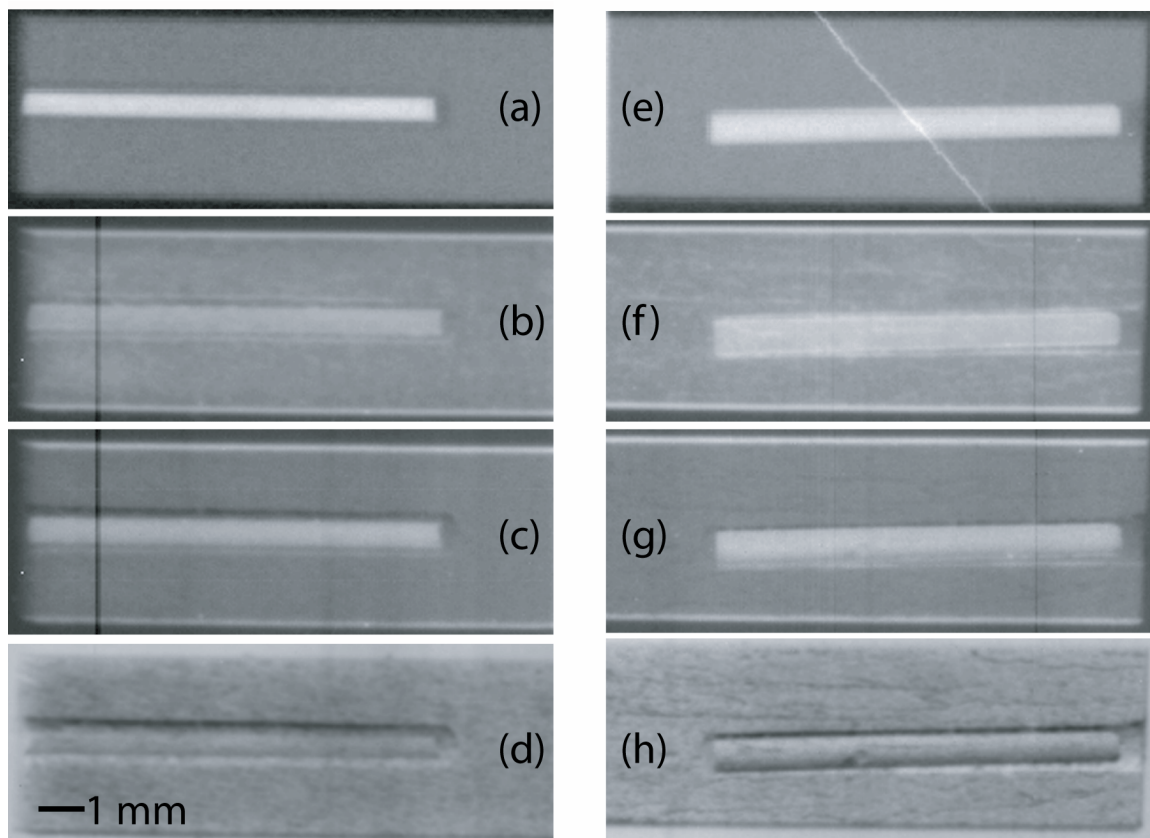


Figure 4.6 Images from the shaved pin experiment. Images (a)-(d) are the SR radiograph, peak, apparent absorption, and refraction images, respectively, of the 200 micron interface gap. Images (e)-(h) are the radiograph, peak, apparent absorption, and refraction images, respectively, of the 100 micron interface gap.

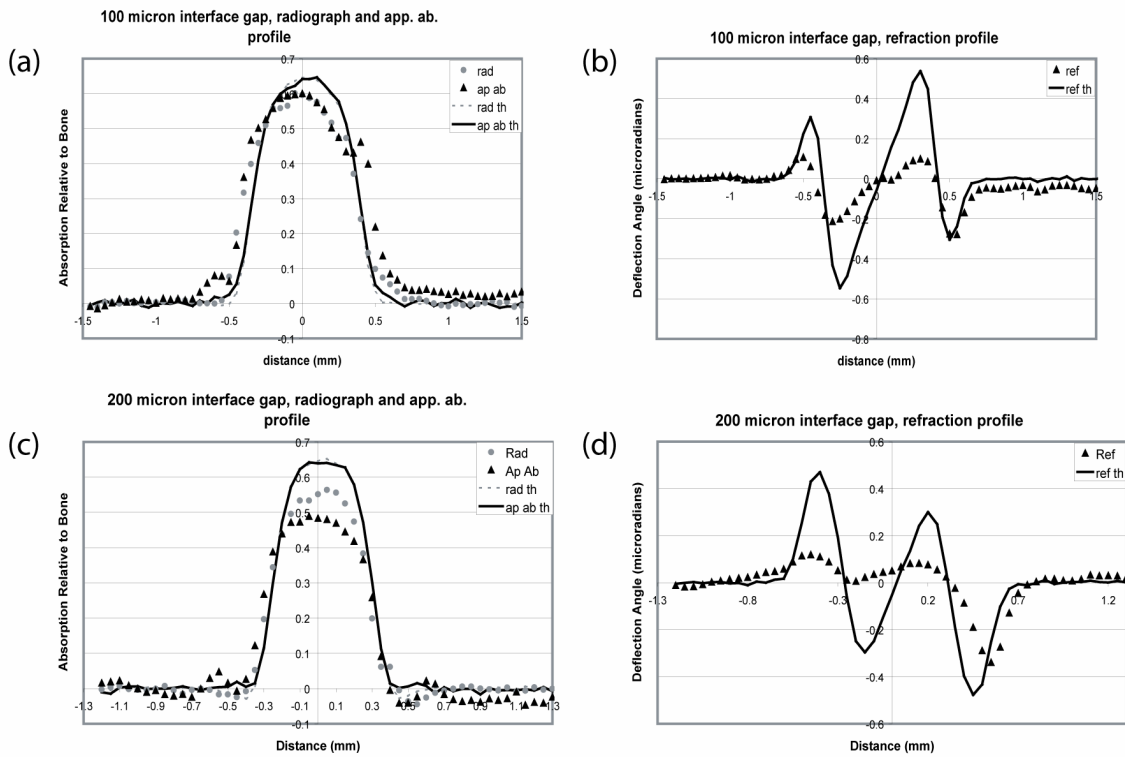


Figure 4.7 Line profiles taken from the shaved pin experiment. Profiles (a) and (c) are the predicted (dashed gray line) and experimental (gray dots) SR radiograph results as well as the predicted (solid black line) and experimental (black triangles) apparent absorption results for the 100 and 200 micron interface gaps respectively. Profiles (b) and (d) include the predicted (solid black line) and experimental (black triangles) refraction results for the 370, 500, 750 and 1000 micron drill holes respectively.

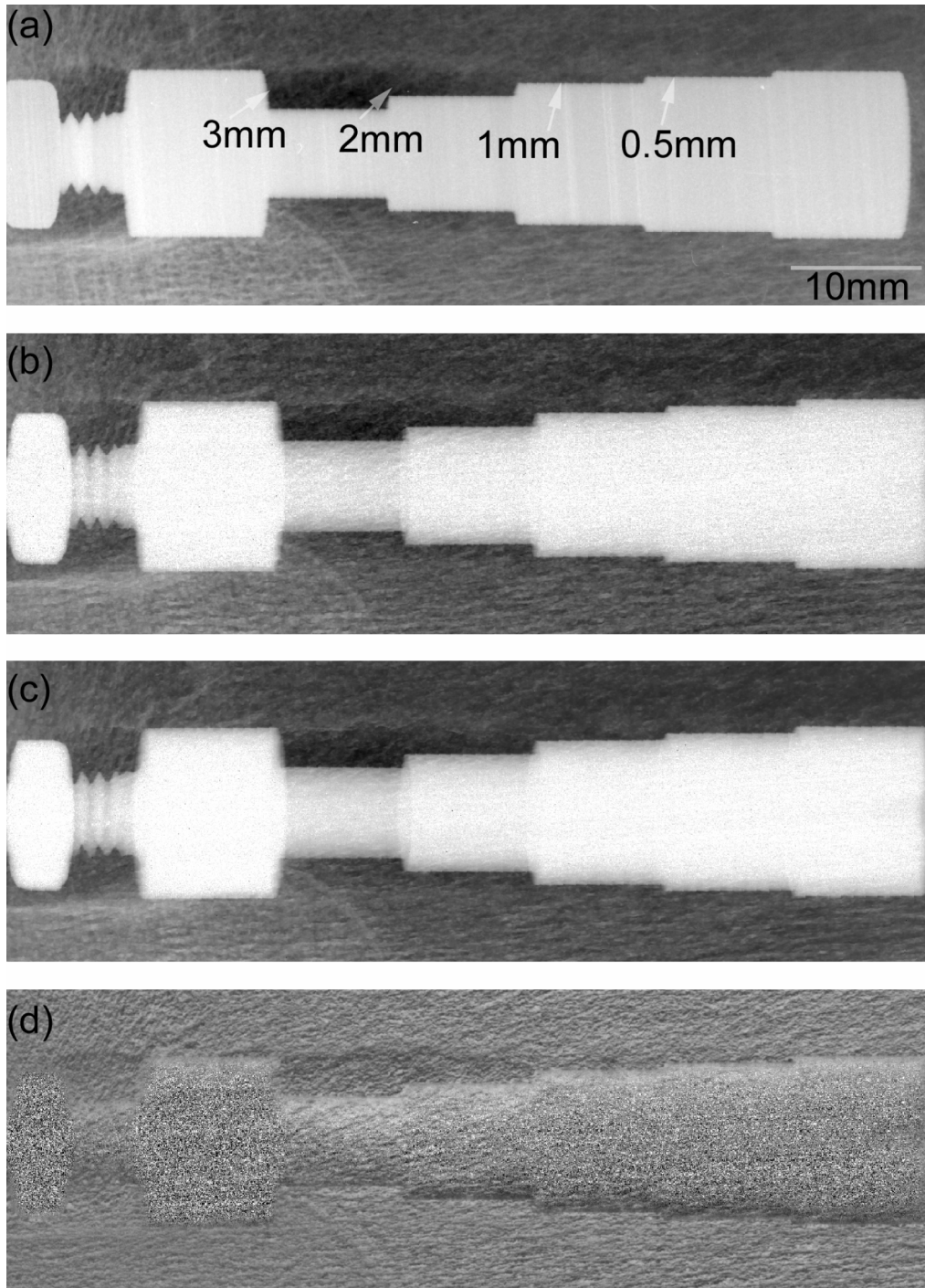


Figure 4.8 Images from the stepped implant experiment. Images (a)-(d) are the SR radiograph, peak, apparent absorption, and refraction images respectively.

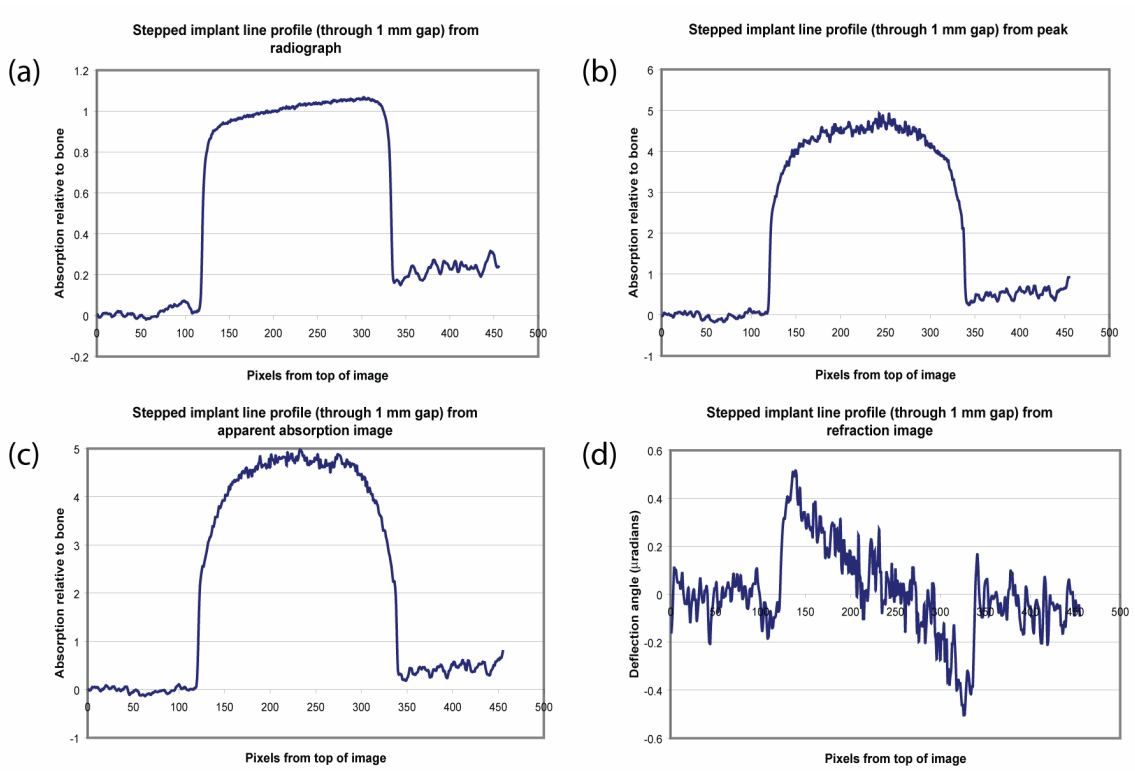


Figure 4.9 Line profiles taken through the 1 mm gap in the stepped implant experiment. Profiles (a)-(d) are from the SR radiograph, peak, apparent absorption, and refraction images respectively.

**5 COMPARISON OF DIFFRACTION-ENHANCED COMPUTED
TOMOGRAPHY AND MONOCHROMATIC SYNCHROTRON RADIATION
COMPUTED TOMOGRAPHY OF HUMAN TRABECULAR BONE**

Written by D.M. Connor, H.D. Hallen, D.S. Lalush, D.R. Sumner, and Z. Zhong

Submitted to *Medical Physics*

5.1 Abstract

Diffraction-enhanced imaging (DEI) is an x-ray-based medical imaging modality that incorporates the use of an analyzer crystal both to retrieve refraction information from a sample and to reject scattered x-rays. When used in tomography mode, DEI can be used to create a three dimensional map of the out-of-plane gradient of the index of refraction of the sample. The goal of this experiment was to compare images of human trabecular bone acquired using monochromatic synchrotron radiation computed tomography (SRCT) with images acquired using diffraction-enhanced computed tomography (DECT). Trabecular bone was chosen both for the fact that its structure is on a scale that can be visualized using the current DE imaging system and because the structure is both refracting and scattering making it a good test of the approximations of two-image DEI. All images were acquired at the National Synchrotron Light Source (Upton, NY, USA) at beamline X15A at an x-ray energy of 40keV. To create a full DECT image set, two sets of projection images were taken with the analyzer crystal detuned to its half-intensity points. The SRCT images were also acquired at X15A, but with the analyzer crystal removed. SRCT, apparent absorption DECT, and refraction DECT slice images of the trabecular bone were created using filtered back-projection. Though the appearance of the trabecular structure is consistent between the apparent absorption and SRCT slice images, the apparent absorption DECT images have a higher resolution and a higher contrast-to-noise ratio than the corresponding SRCT images. Though similar structures are present in the refraction DECT slices, their appearance is much different due to the difference in contrast mechanism.

5.2 Introduction

Osteoporosis is a disease of the bone that leads to a reduction in bone mass and a decrease in bone strength. It most severely affects trabecular bone—the spicular scaffolding present at the end of long bones and in vertebrae—where osteoporotic fractures often occur. Imaging methods that can accurately determine bone strength are essential to diagnose osteoporosis, to evaluate bone deterioration, and to assess the effectiveness of treatment methods. Computed tomography (CT) has been shown to be an effective method to predict bone strength and to assess trabecular structure. The goal of this experiment was to compare contrast and resolution of images of human trabecular bone acquired using monochromatic synchrotron radiation computed tomography (SRCT) with those acquired using diffraction-enhanced computed tomography (DECT) to determine if DECT offers advantages for the assessment of trabecular structure.

5.3 Background

5.3.1 *Assessing trabecular structure*

Correlations have been drawn between the biomechanical strength of trabecular bone and certain trabecular measures.¹⁻³ The most common of these morphological parameters are the average spacing between the trabeculae (Tb.Sp), the average trabecular thickness (Tb.Th), the number of trabeculae in a region (Tb.N), and the ratio of the bone volume to total volume in a region of trabecular bone (BV/TV). When measuring these parameters with CT, the data must first be thresholded—a process whereby each voxel is marked as

being either bone or marrow—then proprietary software is used to determine the morphological parameters. The spatial resolution of the imaging system affects the ability to accurately measure these parameters.^{4,5} For this study, it is assumed that the contrast-to-noise ratio (CNR) in the imaging system limits the effectiveness of the thresholding procedure.

5.3.2 *Diffraction enhanced imaging experiments*

Though still in its early stages of development and testing as a medical imaging modality, diffraction enhanced imaging (DEI) has shown much promise in several different areas of medical imaging. The largest thrust has been towards using DEI for mammography where it has shown contrast advantages over standard radiography for both planar⁶⁻¹¹ and CT imaging¹². DEI has also been shown to have contrast advantages over standard radiography for the imaging of soft tissue in joints.¹³⁻²⁰ Other studies have been done testing DEI's effectiveness in imaging kidneys,²¹ brain tumors,²² thyroids,²³ and bone.²⁴ Of these experiments, three are particularly pertinent to this study. Kiss et al⁸ have shown that DEI, because of additional extinction contrast, has considerable contrast gains over standard radiography for the imaging of calcifications in breast tissue. This is pertinent because the calcifications are dense and scattering and lying in a bed of soft tissue, not unlike trabecular bone (dense and scattering) lying in a bed of marrow. Fiedler et al¹² were the first to report on DECT of biological tissue. They showed that DECT achieves appreciable contrast gains over SRCT in the imaging of invasive lobular carcinoma in adipose tissue in the breast. In a prior study, the author (DMC) has shown that bone has measurable ultra-small angle scattering (USAXS).²⁴

5.3.3 *DEI description*

In DEI, physical properties of an analyzer crystal are exploited to reject or selectively accept scattered x-rays and to retrieve refraction information from a sample.^{10,11,25-29} For x-ray energies that are usable in medical imaging (20-60 keV), an analyzer crystal has a reflectivity profile, called a rocking curve, with a width on the order of microradians.³⁰ Any transmitted x-rays that deviate by more than a few microradians from the analyzer crystal's Bragg peak will not be reflected by the analyzer crystal. This means that all small-angle x-ray scattering (SAXS; on the order of milliradians) and all but a very narrow range of ultra-small angle x-ray scattering (USAXS; on the order of microradians) is rejected by the analyzer crystal. This rejection of scattered x-rays leads to additional contrast, called extinction contrast, in the DEI projection image.

Several different forms of DEI are now being used. In all DEI forms, the analyzer crystal is tilted to positions relative to its peak reflectivity position. For this study, the two-image DEI method, as described for planar imaging by Chapman et al¹⁰ and for CT by Dilmanian et al,²⁶ is used. In the two-image method, the analyzer crystal is tilted to the high-angle and low-angles sides of the rocking curve that correspond to half the peak reflectivity. By combining these high-angle and low-angle projection images, an apparent absorption image and a refraction image can be created. The apparent absorption image should appear similar to a standard radiography image, but with additional extinction contrast. Scattering materials (like bone) will appear to be more absorbing in the apparent absorption image than they would in a standard radiograph. As with SRCT, the apparent absorption images are used to create a three dimensional map of the absorption coefficient in the sample. In

tomography mode, the refraction projection images are used to create a three dimensional map of the out-of-plane gradient of the index of refraction within the sample,²⁶ so image contrast is related to the change in index of refraction along the vertical direction.

Because trabecular bone has a structure on a scale that can be visualized using the current diffraction-enhanced imaging (DEI) system and its structure both refracts and scatters, it is a good test of two-image DEI.

5.4 Materials and methods

Human trabecular bone samples were obtained from the Gift of Hope Organ and Tissue Donor Network with institutional IRB approval. The samples were cut into cylindrical cores measuring about 0.5 cm in diameter and about 1 cm in height and fixed to a small metal platform using epoxy. The metal platform was placed in a water-filled acrylic cylinder that was attached to a rotating sample stage which was attached to a scanning stage.

The data were obtained at the National Synchrotron Light Source (NSLS) beamline X15A. A diagram of the experimental setup at X15A is included in Fig. 5.1. Two major changes have been made to the original DEI setup:²⁵ the rotation stage has been added to the scanning stage to allow for CT and the imaging plate has been replaced by a Rad-Icon Shad-o-Box™ 2048 X-ray Camera which generates 2048 by 1024 images with a 50 μm by 50 μm pixel size. The double-crystal monochromator and analyzer crystal of the DEI system were tuned to 40 keV using the silicon [333] reflection. To create a full DECT image set, 720 projection images were taken rotating the sample in 0.5 degree increments with the analyzer crystal tuned to +0.8 μrad and then -0.8 μrad with respect to the Bragg peak. The exposure

time for each projection image was one second. Since there was a delay of about one second between each of the images, the total acquire time for each 720 image set was approximately 20 minutes. Prior to CT reconstruction, the projection images were combined to form refraction and apparent absorption images using the *equations* 5.1 and 5.2, respectively, defined by Chapman et al¹⁰ where I_R is the calculated intensity of the apparent absorption image, $\Delta\theta_Z$ is the angular deviation of the x-rays, I_H and I_L are the measured intensities in the high-angle and low-angle images, and $R(\theta_H)$ and $R(\theta_L)$ are the reflectivity of the rocking curve at the high-angle and low-angle positions.

$$I_R = \frac{I_L \left(\frac{dR}{d\theta} \right) (\theta_H) - I_H \left(\frac{dR}{d\theta} \right) (\theta_L)}{R(\theta_L) \left(\frac{dR}{d\theta} \right) (\theta_H) - R(\theta_H) \left(\frac{dR}{d\theta} \right) (\theta_L)} \quad \text{Equation 5.1}$$

$$\Delta\theta_Z = \frac{I_H R(\theta_L) - I_L R(\theta_H)}{I_L \left(\frac{dR}{d\theta} \right) (\theta_H) - I_H \left(\frac{dR}{d\theta} \right) (\theta_L)} \quad \text{Equation 5.2}$$

Under the assumption that the images are taken symmetrically about the rocking curve peak at the half-intensity points, these equations reduce down to *equations* 5.3 and 5.4.

$$I_R = I_H + I_L \quad \text{Equation 5.3}$$

$$\Delta\theta_Z = \frac{1}{2 \left| \left(\frac{dR}{d\theta} \right) (\theta_H) \right|} \frac{I_H - I_L}{I_R} \quad \text{Equation 5.4}$$

The SRCT images were acquired as described above, but with the analyzer crystal removed. Apparent absorption DECT, refraction DECT, and SRCT reconstructions of the trabecular bone were created using filtered back-projection with a Shepp-Logan filter and ring artifact correction using a modification of IDL code developed by Rivers.³¹ These 2D

slices were then exported from IDL as 8-bit TIFF files. The files were imported to Photoshop where they were histogram- and gamma-corrected.

As a measure of system resolution, line profiles were taken through the smallest trabecular features that were perceptible in the apparent absorption DECT, refraction DECT, and SRCT slices. The line profiles from both the apparent absorption DECT and SRCT profiles were fit to a Gaussian and the FWHM from each was recorded. All three line profiles were also used to determine an average contrast-to-noise ratio (CNR) for these small features in bone. For the apparent absorption and SR profiles, the CNR was determined using

$$CNR = \frac{\mu_{\max} - \mu_{\min}}{\sigma_{\text{back}}} \quad \text{Equation 5.5}$$

where σ_{back} is the standard deviation in a 30 by 30 pixel section of the slice containing only water, and μ_{\max} and μ_{\min} are the maximum and minimum values, respectively, of the absorption coefficient along the line profile. For the refraction profiles, the CNR was determined using

$$CNR_{\text{refr}} = \frac{\Delta\theta_{z,\max} - \Delta\theta_{z,\min}}{\sigma_{\text{back}}} \quad \text{Equation 5.6}$$

where σ_{back} is the standard deviation in a 30 by 30 pixel section of the slice containing only water, and $\Delta\theta_{z,\max}$ and $\Delta\theta_{z,\min}$ are the maximum and minimum values, respectively, of the refraction signal along the line profile. The apparent absorption and refraction gains, defined as the ratio of the CNR from the DECT slices to the CNR from the SRCT slices ($CNR_{\text{appab}}/CNR_{\text{SR}}$ and $CNR_{\text{refr}}/CNR_{\text{SR}}$), were then recorded.

5.5 Results

Four SRCT and apparent absorption DECT slice images of corresponding sections of bone are displayed in Fig. 5.2. Qualitatively, the apparent absorption image appears sharper than the radiograph image. The SR image shows more connectedness between trabecular structure than the apparent absorption slice does.

Figure 5.3 includes slice image comparisons between corresponding apparent absorption and refraction slice images. The trabecular structures that can be seen as a dot in the apparent absorption image can be seen at the same location in the refraction image, but as a white and black dot surrounded by gray. Because the refraction slice presents a measure of the out-of-plane gradient of the index of refraction, the refraction image contains information on the orientation of the trabecular structures within the slice.

The average FWHM for the line profiles in the apparent absorption DECT slice was $160 \pm 20 \mu\text{m}$ and for the SRCT slice was $200 \pm 40 \mu\text{m}$ using a total of 18 line profiles from each image set. Line profile plots from a corresponding feature in an SRCT slice and an apparent absorption and refraction DECT slice are shown in Figures 5.4(a), 5.4(c), and 5.4(e), respectively. The region of each image used to create the line profile is circled in the corresponding SRCT, apparent absorption DECT, or refraction DECT image [Figures 5.4(b), 5.4(d), and 5.4(f)]. A paired t-test was performed with the alternative hypothesis that the true mean $\text{FWHM}_{\text{appabDECT}}$ was less than the true mean $\text{FWHM}_{\text{SRCT}}$ and a confidence interval of 99%. The paired t-test showed the difference between the feature widths to be statistically significant ($p < 0.001$). The narrower FWHM for the apparent absorption DECT images suggests that it is higher resolution than the SRCT image. The average apparent absorption

CNR gain of 2.2 +/- 0.7 compared to SRCT was found. A paired t-test was performed with the alternative hypothesis that the true mean $CNR_{appabDECT}$ was greater than the true mean CNR_{SRCT} and a confidence interval of 99%. The paired t-test showed the difference between the CNR values to be statistically significant ($p < 0.0001$), so the CNR gain was statistically significant. A gain in CNR means that the bone region of the apparent absorption DECT slice stands out more against the background (surrounding water) than it does in an SRCT slice. An average refraction CNR gain of 3.7 +/- 1.4 compared to SRCT was found. A paired t-test was performed with the alternative hypothesis that the true mean $CNR_{refrDECT}$ was greater than the true mean CNR_{SRCT} and a confidence interval of 99%. The paired t-test showed the difference between the CNR values to be statistically significant ($p < 0.0001$), so the CNR gain of refraction DECT over SRCT was statistically significant.

5.6 DISCUSSION

The results of this experiment are promising, but it is important to keep in mind the scope of these findings. It has been shown here that DECT has CNR and resolution gains over SRCT but only for the specific case of imaging bone in water. The CNR results may seem to be contradictory to the findings of Dilmanian et al²⁶ where apparent absorption DECT was shown to not have contrast gains over SRCT. In their experiment, they imaged an acrylic cylinder with an angularly cut drill hole that was filled with olive oil. Olive oil is far less scattering than bone so we should expect there to be very little extinction contrast gain. So what little was gained with extinction contrast was lost through the addition of noise caused by adding two images together to form the apparent absorption DECT image.

There are considerable limitations to the two-image DECT method. The two-image DECT method assumes little USAXS in the sample,^{10,25,26} so USAXS from the sample will lead to a reduction in refraction contrast.^{8,32} Any mechanical vibrations or thermal variations cause a detuning of the system. The two-image method assumes that images are taken symmetrically about the rocking curve peak. Since the reflectivity and the magnitude of the slope of the rocking curve are equivalent at the two positions, any detuning of the system leads to a reduction in contrast in the DE images through a mixing of refraction and absorption signals. Another limitation of DEI is that it is only sensitive to the out-of-plane gradient of the index of refraction. This means that the refraction contrast is not only related to the difference in indices of refraction between two materials, but also to the orientation of the interface between the materials. If there is a vertical interface—meaning the interface between the two indices of refraction is perpendicular to the plane of the x-ray beam—within a voxel, then there is no refraction contrast.

The rejection of scatter that leads to additional contrast in the apparent absorption images leads to a reduction in contrast in the refraction image. The large amount of USAXS in bone means that the refraction image results must be considered qualitatively rather than quantitatively, which limits the usefulness of the results. What can be inferred from the data is whether the index of refraction is increasing, decreasing, or remaining the same along the vertical direction within the voxel. If one assumes there is no variation in index of refraction within materials (the entire region is composed of either n_{bone} or n_{water}), then a black or white pixel means there is an interface between materials within that voxel. A black pixel in the

refraction slice image means there is an interface between water and bone in which the water region of that volume is above the bone region of that volume.

5.7 Conclusions

In this preliminary investigation of DECT of trabecular bone, we have found here that apparent absorption DECT has modest but statistically significant gains in both resolution and contrast-to-noise ratio over monochromatic synchrotron radiation CT for imaging trabecular structure. Because measures for the morphological parameters in trabecular bone are affected by system resolution, an increase in system resolution suggests the DECT could produce more accurate morphological parameters than SRCT. Significant contrast-to-noise ratio gains were also found for the small structures in the refraction DECT image as compared to the SRCT image. Further studies are needed to more thoroughly compare the two imaging methods.

5.8 Acknowledgements

Thanks to the Gift of Hope Organ and Tissue Donor Network for providing the samples. The research was supported by an NCSU FRPD grant, by the Department of the Army grant DAMD170110811, by the U.S. Department of Energy contract No. DE-AC02-98CH10886, by NIH grants R01 AR48292 and AR039239, and by the Brookhaven National Laboratory LDRD grant #05-057.

5.9 References

- ¹ D. Ulrich, B. Van Rietbergen, A. Laib, and P. Ruegsegger, "*The ability of three-dimensional structural indices to reflect mechanical aspects of trabecular bone*," *Bone* **25** (1), 55 (1999).
- ² T. M. Keaveny, E. F. Morgan, G. L. Niebur, and O. C. Yeh, "*Biomechanics of trabecular bone*," *Annual Review of Biomedical Engineering* **3**, 307 (2001).
- ³ T. M. Link, S. Majumdar, S. Grampp, G. Guglielmi, C. van Kuijk, H. Imhof, C. Glueer, and J. E. Adams, "*Imaging of trabecular bone structure in osteoporosis*," *European Radiology* **9** (9), 1781 (1999).
- ⁴ M. Kothari, T. M. Keaveny, J. C. Lin, D. C. Newitt, H. K. Genant, and S. Majumdar, "*Impact of spatial resolution on the prediction of trabecular architecture parameters*," *Bone* **22** (5), 437 (1998).
- ⁵ R. Muller, M. Hahn, M. Vogel, G. Delling, and P. Ruegsegger, "*Morphometric analysis of noninvasively assessed bone biopsies: Comparison of high-resolution computed tomography and histologic sections*," *Bone* **18** (3), 215 (1996).
- ⁶ M. O. Hasnah, Z. Zhong, O. Oltulu, E. Pisano, R. E. Johnston, D. Sayers, W. Thomlinson, and D. Chapman, "*Diffraction enhanced imaging contrast mechanisms in breast cancer specimens*," *Medical Physics* **29** (10), 2216 (2002).
- ⁷ M. O. Hasnah, C. Parham, E. D. Pisano, Z. Zhong, O. Oltulu, and D. Chapman, "*Mass density images from the diffraction enhanced imaging technique*," *Medical Physics* **32** (2), 549 (2005).
- ⁸ M. Z. Kiss, D. E. Sayers, Z. Zhong, C. Parham, and E. D. Pisano, "*Improved image contrast of calcifications in breast tissue specimens using diffraction enhanced imaging*," *Physics in Medicine and Biology* **49** (15), 3427 (2004).
- ⁹ E. D. Pisano, R. E. Johnston, D. Chapman, J. Geradts, M. V. Iacocca, C. A. Livasy, D. B. Washburn, D. E. Sayers, Z. Zhong, M. Z. Kiss, and W. C. Thomlinson, "*Human breast cancer specimens: Diffraction-enhance imaging with histologic correlation -*

- Improved conspicuity of lesion detail compared with digital radiography," Radiology* **214** (3), 895 (2000).
- ¹⁰ D. Chapman, W. Thomlinson, R. E. Johnston, D. Washburn, E. Pisano, N. Gmur, Z. Zhong, R. Menk, F. Arfelli, and D. Sayers, "*Diffraction enhanced x-ray imaging,*" *Physics in Medicine and Biology* **42** (11), 2015 (1997).
- ¹¹ Dean Chapman, William Thomlinson, F. Arfelli, N. Gmür, Zhong Zhong, R. Menk, R.E. Johnston, D. Washburn, Etta Pisano, and Dale Sayers, "*Mammography imaging studies using a Laue crystal analyzer,*" *Review of Scientific Instruments* **67** (9), (published on CD (1996).
- ¹² S. Fiedler, A. Bravin, J. Keyrilainen, M. Fernandez, P. Suortti, W. Thomlinson, M. Tenhunen, P. Virkkunen, and M. L. Karjalainen-Lindsberg, "*Imaging lobular breast carcinoma: comparison of synchrotron radiation DEI-CT technique with clinical CT, mammography and histology,*" *Physics in Medicine and Biology* **49** (2), 175 (2004).
- ¹³ J. Li, Z. Zhong, R. Lidtke, K. E. Kuettner, C. Peterfy, E. Aliyeva, and C. Muehleman, "*Radiography of soft tissue of the foot and ankle with diffraction enhanced imaging,*" *Journal of the American Podiatric Medical Association* **94** (3), 315 (2004).
- ¹⁴ S. Majumdar, A. S. Issever, A. Burghardt, J. Lotz, F. Arfelli, L. Rigon, G. Heitner, and R. H. Menk, "*Diffraction enhanced imaging of articular cartilage and comparison with micro-computed tomography of the underlying bone structure,*" *European Radiology* **14** (8), 1440 (2004).
- ¹⁵ J. Mollenhauer, M. E. Aurich, Z. Zhong, C. Muehleman, C. C. Cole, M. Hasnah, O. Oltulu, K. E. Kuettner, A. Margulis, and L. D. Chapman, "*Diffraction-enhanced X-ray imaging of articular cartilage,*" *Osteoarthritis and Cartilage* **10** (3), 163 (2002).
- ¹⁶ C. Muehleman, M. Whiteside, Z. Zhong, J. Mollenhauer, M. Aurich, K. E. Kuettner, and L. D. Chapman, "*Diffraction enhanced imaging for articular cartilage,*" *Biophysical Journal* **82** (1), 470A (2002).
- ¹⁷ C. Muehleman, L. D. Chapman, K. E. Kuettner, J. Rieff, J. A. Mollenhauer, K. Massuda, and Z. Zhong, "*Radiography of rabbit articular cartilage with diffraction-enhanced imaging,*" *Anatomical Record Part a-Discoveries in Molecular Cellular and Evolutionary Biology* **272A** (1), 392 (2003).

- 18 C. Muehleman, S. Majumdar, A. S. Issever, F. Arfelli, R. H. Menk, L. Rigon, G. Heitner, B. Reime, J. Metge, A. Wagner, K. E. Kuettner, and J. Mollenhauer, "*X-ray detection of structural orientation in human articular cartilage*," *Osteoarthritis and Cartilage* **12** (2), 97 (2004).
- 19 C. Muehleman, D. R. Sumner, and Z. Zhong, "*Refraction effects of diffraction enhanced radiographic imaging - A new look at bone*," *Journal of the American Podiatric Medical Association* **94** (5), 453 (2004).
- 20 A. Wagner, M. Aurich, N. Sieber, M. Stoessel, W. D. Wetzel, K. Schmuck, M. Lohmann, B. Reime, J. Metge, P. Coan, A. Bravin, F. Arfelli, L. Rigon, R. H. Menk, G. Heitner, T. Irving, Z. Zhong, C. Muehleman, and J. A. Mollenhauer, "*Options and limitations of joint cartilage imaging: DEI in comparison to MRI and sonography*," *Nuclear Instruments & Methods in Physics Research Section a-Accelerators Spectrometers Detectors and Associated Equipment* **548** (1-2), 47 (2004).
- 21 L. Gang, Z. H. Chen, Z. Y. Wu, M. Ando, P. Lin, J. Y. Wang, and X. M. Jiang, "*Image quality dependence on thickness of sliced rat kidney taken by a simplest DEI construction*," *Nuclear Instruments & Methods in Physics Research Section a-Accelerators Spectrometers Detectors and Associated Equipment* **548** (1-2), 200 (2004).
- 22 K. A. Mannan, E. Schultke, R. H. Menk, K. Siu, K. Pavlov, M. Kelly, G. McLoughlin, T. Beveridge, G. Tromba, B. H. Juurlink, D. Chapman, L. Rigon, and R. W. Griebel, "*Synchrotron supported DEI/KES of a brain tumor in an animal model: The search for a microimaging modality*," *Nuclear Instruments & Methods in Physics Research Section a-Accelerators Spectrometers Detectors and Associated Equipment* **548** (1-2), 106 (2004).
- 23 H. S. Rocha, R. T. Lopes, P. M. Valiante, G. Tirao, I. Mazzaro, M. G. Honnicke, C. Cusatis, and C. Giles, "*Diagnosis of thyroid multinodular goiter using diffraction-enhanced imaging*," *Nuclear Instruments & Methods in Physics Research Section a-Accelerators Spectrometers Detectors and Associated Equipment* **548** (1-2), 175 (2004).
- 24 D. M. Connor, D. Sayers, D. R. Sumner, and Z. Zhong, "*Identification of fatigue damage in cortical bone by diffraction enhanced imaging*," *Nuclear Instruments & Methods in Physics Research Section a-Accelerators Spectrometers Detectors and Associated Equipment* **548** (1-2), 234 (2004).

- 25 Zhong Zhong, William Thomlinson, Dean Chapman, and Dale Sayers, "Implementation of diffraction-enhanced imaging experiments: at the NSLS and APS," *Nuclear Instruments and Methods in Physics Research A* **450**, 556 (2000).
- 26 F. A. Dilmanian, Z. Zhong, B. Ren, X. Y. Wu, L. D. Chapman, I. Orion, and W. C. Thomlinson, "Computed tomography of x-ray index of refraction using the diffraction enhanced imaging method," *Physics in Medicine and Biology* **45** (4), 933 (2000).
- 27 M. N. Wernick, O. Wirjadi, D. Chapman, Z. Zhong, N. P. Galatsanos, Y. Y. Yang, J. G. Brankov, O. Oltulu, M. A. Anastasio, and C. Muehleman, "Multiple-image radiography," *Physics in Medicine and Biology* **48** (23), 3875 (2003).
- 28 O. Oltulu, Z. Zhong, M. Hasnah, M. N. Wernick, and D. Chapman, "Extraction of extinction, refraction and absorption properties in diffraction enhanced imaging," *Journal of Physics D-Applied Physics* **36** (17), 2152 (2003).
- 29 E. Pagot, P. Cloetens, S. Fiedler, A. Bravin, P. Coan, J. Baruchel, J. Hartwig, and W. Thomlinson, "A method to extract quantitative information in analyzer-based x-ray phase contrast imaging," *Applied Physics Letters* **82** (20), 3421 (2003).
- 30 William H. Zachariasen, *Theory of X-ray diffraction in crystals*. (J. Wiley, New York, 1945).
- 31 M. Rivers, *Tutorial Introduction to X-ray Computed Microtomography Data Processing*, Retrieved August 13, 2003, from <http://www-fp.mcs.anl.gov/xray-cmt/rivers/tutorial.html>.
- 32 K. M. Pavlov, C. M. Kewish, J. R. Davis, and M. J. Morgan, "A variant on the geometrical optics approximation in diffraction enhanced tomography," *Journal of Physics D-Applied Physics* **34** (10A), A168 (2001).

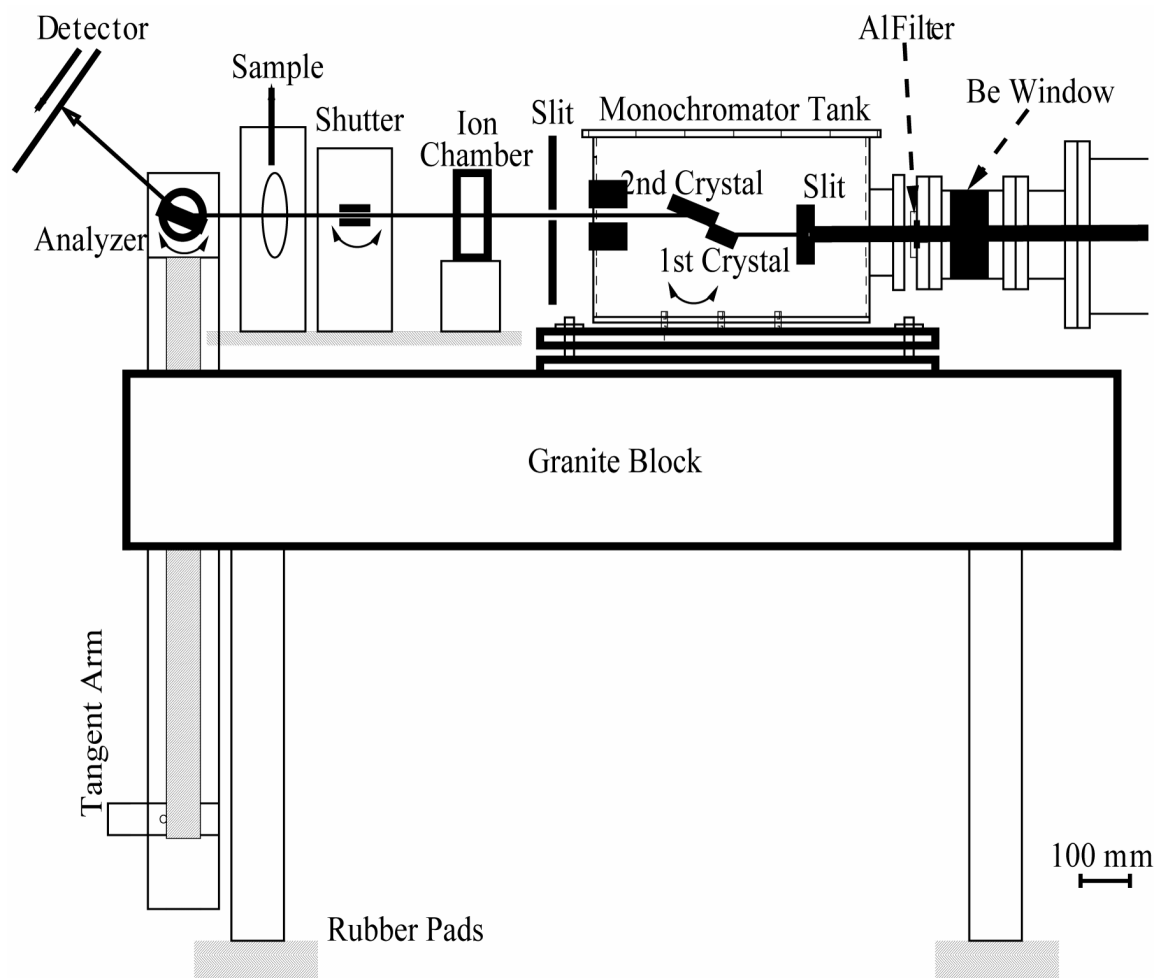


Figure 5.1 Diagram of experimental setup at Beamline X15A at the National Synchrotron Light Source, Upton, NY, USA

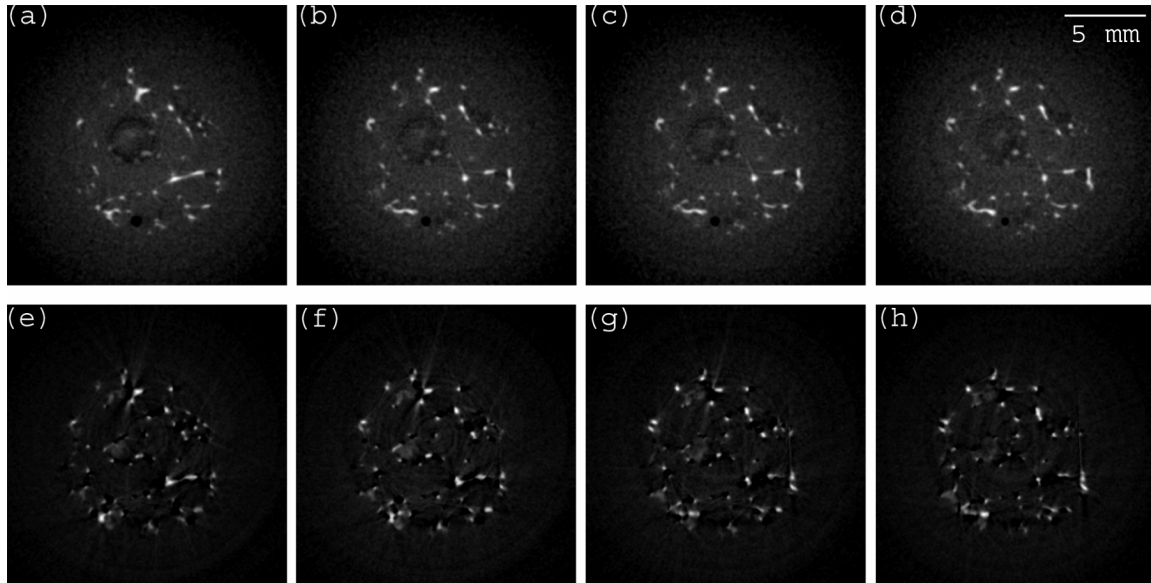


Figure 5.2 Example slice images of trabecular bone. Images (a)-(d) are consecutive slices from monochromatic synchrotron radiation computed tomography. Images (e)-(h) are from apparent absorption diffraction enhanced computed tomography.

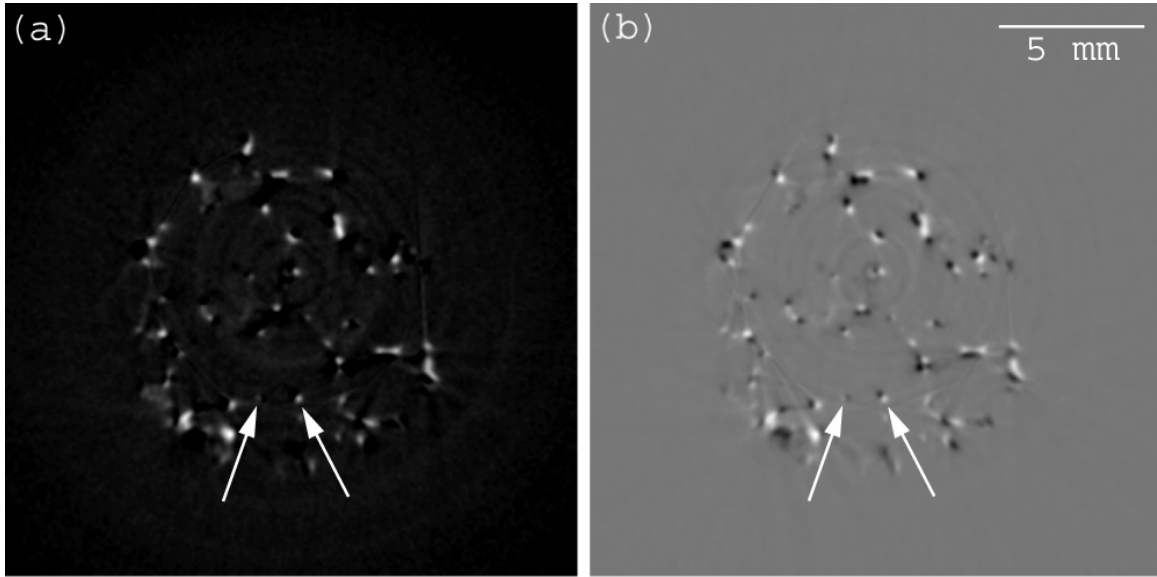


Figure 5.3 Comparison slice images of trabecular bone from (a) apparent absorption DECT and (b) refraction DECT.

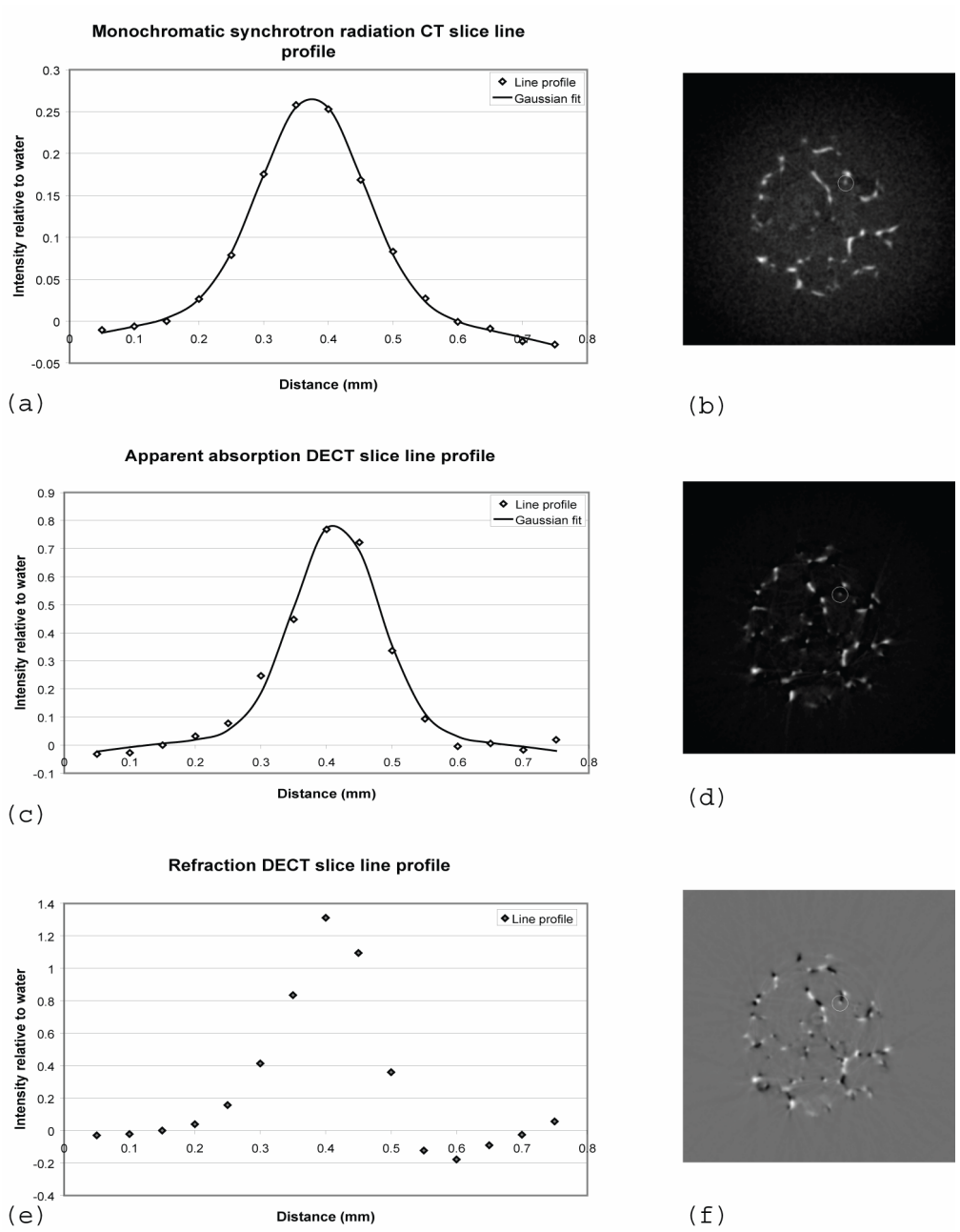


Figure 5.4 Example line profiles from small features in the trabecular bone slice images. Plots (a), (c), and (e) are from the SRCT slice, the apparent absorption DECT slice, and the refraction DECT slice. The Gaussian fit is shown for the (a) SR and (b) apparent absorption profile. The slice image is shown in (b), (d), and (f) for SRCT, apparent absorption DECT, and refraction DECT images with the trabecular feature from the line profile encircled.

**6 DEVELOPMENT OF A COMPUTER MODEL TO PREDICT ULTRA-SMALL
ANGLE X-RAY SCATTERING IN CORTICAL BONE**

Written by D.M. Connor, H.D. Hallen, D.R. Sumner, Z. Zhong, and L.D. Chapman

Submitted to *Bone*

6.1 Abstract

A computer model was developed to help determine what structures within bone were causing the experimentally measured ultra-small angle x-ray scattering (USAXS) from bone. A Monte Carlo ray tracing algorithm is incorporated into the model. The model simulates the USAXS by calculating the x-ray refraction from multiple randomly placed structures within the bone. The results of the model were compared to the angular spreading of x-rays transmitted through bone as measured using diffraction enhanced imaging. When the scattering is modeled as being from osteocyte lacunae which are small cavities in bone, the predicted angular spreading width (0.888 μ radians) agreed with the experimentally measured angular spreading width (0.62 \pm 0.24 μ radians).

6.2 Introduction

X-ray scattering has been used for almost a century to probe objects and reveal information about their internal structure. Small-angle x-ray scattering (SAXS) has revealed the size of a variety of nanometer-scale objects ranging from colloidal gold¹ to mineral crystals within bone.^{2,3} Ultra-small angle x-ray scattering (USAXS) can be used to reveal information about structures within an object that are too large to be studied by SAXS. Under the geometric optics approximation, USAXS can be viewed as the result of multiple random refractions from structures of different elemental composition (different indices of refraction) within an object. The multiple refractions lead to an angular spreading of the transmitted x-ray beam. A new x-ray imaging technique called diffraction enhanced imaging

(DEI) has shown the ability to measure the angular spreading of the x-ray beam, and hence can produce a measure of the USAXS within an object.^{4,5} The measured USAXS could prove to be useful if the angular spreading of the transmitted x-rays that is observed can be traced back to a structure within the object. In order to trace the scattering back to structures within the bone, a model that predicts the scattering profile from these structures will need to be developed. The purpose of this work is to develop a model to predict the USAXS width from structures within bone and to compare the model with experimental measurements of USAXS.

6.3 Background

6.3.1 Structure of plexiform bone

In order to determine what structures within bone cause the measured USAXS, it is important to first look at bone structure. The bones used in the previous experiment were bovine cortical bone. Because bovine bone needs to develop very rapidly, bovine cortical bone is a specific type of cortical bone called plexiform, or fibrolamellar, bone. The building blocks of all types of bone are strands of type I collagen and plate-like dahllite crystals. Individual type I collagen molecules are cylindrical and measure approximately 300 nm in length and 2 nm in diameter.⁶ The dahllite crystals measure on the order of tens of nanometers in length and width and approximately 2 nm thick.⁶ The collagen and crystals combine to form a composite mineralized collagen fibril. These cylindrical mineralized collagen fibrils measure approximately 100 nm in diameter⁷ and are greatly varied in length. In plexiform bone, these mineralized collagen fibrils are roughly aligned with the long bone

axis.⁸ So the bulk of plexiform bone is composed of close-packed arrays of approximately aligned collagen fibrils. Interspersed within the bulk of the plexiform bone are elliptically shaped cavities called osteocyte lacunae. The major axis of the lacunae aligns roughly with the mineralized fibrils⁹ and therefore aligns with the long axis of the bone. When a cross-section of cortical bone is made such that the long axis of the bone is perpendicular to the cross-section plane, the average measured lacunae radius is about 3 μm .¹⁰ Within a cross-section of cortical bone there are approximately 450 lacunae/ mm^2 .¹⁰

6.3.2 Model description

6.3.2.1 Assumptions and approximations

Several assumptions and approximations had to be made in the development of the USAXS computer model. The first major approximation is that the USAXS observed in DEI can be modeled using geometric optics. This is a reasonable approximation because the smallest structures being modeled have sizes three orders of magnitude greater than the x-ray wavelength. Because of this assumption, all scattering is presumed to be from multiple refractions. It was assumed that sufficient random refraction events would occur to justify the application of the central limit theorem. In other words, it is assumed that the scattering leads to a normally distributed angular spread of the transmitted x-rays. There are sufficient densities of mineralized collagen fibrils and osteocyte lacunae—the structures being modeled in bone—for the assumption of multiple refractions to be a valid one. The refracting objects are approximated as having a circular cross-section. It was assumed that the circles were randomly placed through the scattering region and did not overlap. The circles were

assumed to all be of the same radius. The scattering region was assumed to consist of only two different, uniform materials—the uniform density ambient region and the uniform density scattering circles. It was assumed that the x-ray beam was monoenergetic. Lastly, the path of the photons was assumed to be a straight-line path.

6.3.2.2 Model algorithm

This algorithm is a variation of an IDL code developed by Dean Chapman. It is a Monte Carlo ray tracing algorithm consisting of two major procedures. The first procedure randomly places a total of $n_{circles}$ circles of radius, $r_{circles}$, into a rectangle n_x pixels across and n_z pixels high. It checks to ensure that all circles are non-overlapping. The positions of the circles are defined by random floating-point (~6-7 decimal places of significance) numbers generated using the *randomu* function in IDL which is a variation of a random number generator developed by Park et al.¹¹ The procedure passes the positions of the circles to the second procedure.

The second procedure models the photon interaction with the refracting circles. All photons are modeled as moving horizontally (in the $+x$ -direction). All of the z -coordinates of the circles' centers are saved in to an array, $z_{circles}$. The function *randomu* is used again to pick the z -value of the incident photon, z_{photon} . The procedure first checks to see if there are any circles within $\pm r_{circles}$ of z_{photon} . The array position of all the circles within $\pm r_{circles}$ of z_{photon} are saved into a separate array. Then, one-by-one, the angular deflection from each circle, $\Delta\theta$, is determined. The angular deflection from each circle is related to the difference between z_{photon} and z_{circle} by equation 6.1.¹²

$$\Delta\theta = 2(\delta_{circle} - \delta_{ambient}) \frac{|z_{photon} - z_{circle}|}{\sqrt{r_{circle}^2 - (z_{photon} - z_{circle})^2}} \quad \text{Equation 6.1}$$

The index of refraction, n , is defined by equation 6.2, so δ_{circle} and $\delta_{ambient}$ are the

$$n = 1 - \delta - i\alpha \quad \text{Equation 6.2}$$

difference from unity of the real part of the index of refraction (the imaginary part of the index of refraction, α , will be ignored since it is related to absorption). This is repeated n_{photon} times. For each of the n_{photon} photons, a value of the total angular deflection, $\Delta\theta_{total}$, is saved into an array. The n_{photon} -dimensioned array of $\Delta\theta_{total}$ values is then binned using the *histogram* procedure in IDL with a bins size of s_{bin} (generally 0.001 μrad). The normalized histogram, $P_N(\theta_m)$, represents the probability the N^{th} photon will be scattered through an angle of θ_m to $\theta_m + s_{bin}$. The histogram was fit to a Gaussian using the *gaussfit* function in IDL.

6.3.3 DEI description

6.3.3.1 General DEI description

It is important to understand the properties of the DEI system to determine what is causing the USAXS. Several papers have been written that relate the theory of DEI in far greater detail than will be presented here.¹³⁻¹⁷ In DEI, nearly collimated, monochromatic light is incident on an object. A perfect silicon analyzer crystal is placed between the object and the detector. For a given crystal reflection, e.g. [111], and energy, the analyzer crystal has a reflectivity profile, called a rocking curve, that is a function of angle and has a width that is highly energy dependent, but usually on the order of a few microradians.¹⁸ The peak

of the reflectivity profile is at the Bragg angle associated with that particular energy and reflection. Since the analyzer crystal only reflects x-rays of a very narrow range of angles and energies, all x-rays that are outside of that narrow range are not reflected by the analyzer. For this reason, the analyzer crystal can be thought of as a very narrow (in both angle and energy) notch filter.

6.3.3.2 *Rocking curves studies*

The narrow angular acceptance of the analyzer crystal can be exploited to measure the USAXS from a sample. If the analyzer is tuned at the Bragg peak, then any transmitted x-rays that are scattered by more than a few microradians are rejected by the analyzer. If detuned from its Bragg peak by some angle, θ , then the analyzer crystal will only reflect x-rays that are either scattered or reflected within a very narrow range of that same angle, θ . To extract USAXS information, the intensity of light reflected by the analyzer crystal as a function of detuning angle, θ , can be measured. The intrinsic rocking curve of the system can be found by measuring the reflected intensity as a function of detuning angle with no sample along the beam path. The rocking curve can then be measured as a function of angle with a sample in the beam path. If there is USAXS within the sample, then the width of the rocking curve with a sample present will be larger than the intrinsic rocking curve.

This method of measuring USAXS has a significant limitation—it is only sensitive to angular deflections that are upward or downward (and not left or right deviations). This limitation means that the measured USAXS signal can be dependent on the sample orientation.

This study evolved from another experiment performed by Connor et al ¹⁹. In the previous experiment, bovine cortical bones were studied prior to and after fatigue loading to determine if a signature of microfracture could be seen. Rocking curve measurements were made prior to and after the samples were fatigue loaded. It was found that there was indeed significant USAXS in the bones. The genesis of this study was trying to find that answer to the question: If USAXS can indeed be explained by—or at least approximated as—multiple random refractions within the sample, what structures within bone cause the x-rays to refract?

6.4 Materials and methods

6.4.1 General model attributes

In order to understand the general attributes of the computer model, the parameters were varied and the model response was documented. To test the model's dependence upon circle radius, the circle radius was adjusted while keeping all other parameters constant. For a box size of 2,000 pixels (along the x-direction) by 1,000 pixels (along the z-direction), one million photons ($n_{photons}=1,000,000$), 4,000 circles ($n_{circles}=4,000$), a photon energy, E_{photon} , of 40 keV, an ambient material of bone, and a circle material of water, r_{circle} was varied from 0.5 to 3 pixels in 0.1 pixel steps. For each point, the width of the scattering, $\sigma_{scatter}$, was simulated.

A separate test was performed to determine system response to variations in $n_{circles}$. For the same box size, number of photons, photon energy, ambient material, and circle

material as above, and for an r_{circle} of 1.5 pixels, $n_{circles}$ was varied from 1,000 to 6,700 in steps of 100 and $\sigma_{scatter}$ was simulated for each n_{circle} value.

The energy dependence of the model was measured as well. For the same box size, number of photons, ambient material, and circle material as above, and for an r_{circle} of 1.5 pixels and for 4,000 photons, the energy was varied from 15 to 100 keV and $\sigma_{scatter}$ was measured for each photon energy. The amount of refraction from the individual circles depends on the difference between the indices of refraction of the ambient and circle material ($\Delta\delta$), so to test the model's response to different materials, the ambient material was chosen to be bone and the δ of the circle was set to be a scalar multiple of δ_{bone} ($\delta_{circle} = \delta_{bone} * SF$). For the same parameters as the previous experiment, and for an photon energy of 40 keV, the scale factor was varied from 0.1 to 3.0 in steps of 0.1 and $\sigma_{scatter}$ was simulated for each scale factor.

6.4.2 *Modeling structures in plexiform bone*

In plexiform bone, the structures that could be causing the measured USAXS are mineralized collagen fibrils (diameter of about 100 nm) or osteocyte lacunae (diameter of about 6 μm). Because the scattering experiment measured the scatter from 4 mm thick sections of bone, the model parameters were designed to mimic the full bone thickness. For modeling the collagen fibrils, there should be on the order of 10^9 fibrils passing through the 4 mm by 4 mm cross section. Because it would be too computationally intensive to model a full 4mm by 4 mm segment of bone at once, a 10 μm by 10 μm section of bone was modeled. There are about 9,000 fibrils that would pass through this smaller section of bone. The

photon energy was set to 40 keV (to match the x-ray energy used in the experiment). The ambient material was chosen to be water and the circle material was set to bone. The value of δ_{water} and δ_{bone} were calculated using material composition data from NIST²⁰. The net angular deflection of one million photons were measured. The measured scattering was only for a 10 μm by 10 μm section of bone. In order to model the full 4 mm thickness of bone, the scattering Gaussian for the smaller section was convolved with itself 400 times. Because the scattering was normally distributed, the total scatter width, $\sigma_{\text{scatter,total}}$, is just $20\sigma_{\text{scatter}}$.

The lacunae are much larger than the fibrils and much more sparse, so modeling them was simpler. The scattering region was chosen to be 2,000 pixels by 1,000 pixels corresponding to a 4 mm by 2 mm segment of bone. The scale was 1 pixel for every 0.002 mm, so the circle radius was set to 1.5 pixels. Since the lacunae density is about 450 lacunae/ mm^2 , there would be about 3,600 lacunae in a 4 mm by 2 mm section of bone. Therefore, n_{circle} was set to 3,600. The ambient material was set to bone and the circle material was set to water. The photon energy was set to 40 keV. For one million incident photons, the scattering was measured.

6.4.3 DEI experiment

Machined bovine cortical bone samples, measuring approximately 4mm by 4mm by 40mm, were prepared at Rush University Medical College. The bone samples were fixed in a 10% formalin solution. The long axis of the sample corresponds to the long axis of the bovine femur. They were secured to an aluminum sample holder, to minimize movement during the imaging process, and then placed in a water-filled acrylic container. The samples were oriented such that the long axis of the sample was in the plane of the beam. This

sample orientation was chosen because the major axis of the lacunae and the axis of the collagen fibrils generally align with the long axis of the sample which means the system was most sensitive to USAXS from the sample in this orientation. Image sets were acquired for a total of 39 bovine cortical bone samples. All data were obtained at the NSLS Beamline X15A. The bending magnet source at X15A produces a polychromatic beam of light that measures about 2 mm high and 10 cm wide in the experimental hutch. The experimental setup (figure 6.1) was as described by Zhong et al¹⁴ with the exception that a new detector was used. Polychromatic light entered the hutch through the beryllium window. Aluminum filters (total thickness of approximately 3mm) reduced the intensity of light entering the monochromator. Because aluminum effectively absorbs lower energy x-rays, the filters greatly reduced the power delivered to the monochromator. The monochromator then selected out 40 keV x-rays using [333] diffraction. An ion chamber then read the surface dose to which the sample and sample holder were exposed during imaging. After next passing through the sample, the transmitted x-ray beam was then incident upon the analyzer crystal where it was either reflected or absorbed depending on the angle at which the analyzer crystal was set. The intensity of reflected x-rays was then recorded by a Rad-Icon Shad-o-Box™ 2048 X-ray Camera which generates 2048 by 1024 images at 50 micron pixel size.

For each bone sample, a set of 101 images was obtained. The sample was positioned such that both the ambient (water only) and bone (bone surrounded by water) were in the field of view in each image. The sample position remained fixed during all of the scans. Images were acquired for each analyzer crystal position as it was scanned from -10 to +10

μ radians in 0.2 μ radian steps. The analyzer crystal was tilted using the tangent arm which has a resolution of 0.1 μ radians. The shutter was closed for the last five images in order to determine the detector background. The exposure time for each individual image was five seconds. Reading out the detector and then moving the analyzer crystal took approximately one second, so the total time to acquire the image set was approximately ten minutes.

The rocking curve widths were obtained using Interactive Data Language (IDL). The median for each individual step of the scan was found in the y -, or vertical, direction. For each value in the x -direction the median y value for each step was fit to a Gaussian and the Gaussian width, σ , was found. The procedure was done separately both for the ambient and bone image regions in each data set. The ambient rocking curve is the intrinsic rocking curve of the system, or the zero-scatter reflectivity profile of the system. The Gaussian width of the measured rocking curve through bone is the combination of the ambient, or intrinsic, rocking curve with and the scattering rocking curve width. This combination can be thought of as the convolution of the scattering (which is a Gaussian) with the intrinsic rocking curve (which can be approximated as being a Gaussian). In order to find the scattering, the Gaussian fit to the rocking curve through the bone had to be deconvolved with the Gaussian fit to the ambient rocking curve. Because both the curves were approximated as being Gaussian, the width of the scattering Gaussian, $\sigma_{scatter}$, was calculated using equation 6.3.

$$\sigma_{scatter} = \sqrt{(\sigma_{bone})^2 - (\sigma_{ambient})^2} \quad \text{Equation 6.3}$$

6.5 Results

6.5.1 General model attributes

A representative image of the placement of 1,000 circles of radius 20.0 pixels into a 2,000 by 2,000 pixel region is included in figure 6.2a. For the circle configuration from figure 6.2a, with a photon energy of 40 keV, an ambient region of water, a circle material of adipose tissue, and one million photons the resulting histogram and the Gaussian fit to the histogram are included in figure 6.2b.

A plot showing $\sigma_{scatter}$ as a function of circle radius is included in figure 6.3a. It was found that $\sigma_{scatter}$ varied as about $r_{circle}^{0.69}$. An increase in $\sigma_{scatter}$ with an increase in r_{circle} is reasonable because with an increase in circle size, there is an increased likelihood that a photon will hit the circle. A plot showing $\sigma_{scatter}$ as a function of the number of circles is included in figure 6.3b. It was found that $\sigma_{scatter}$ varied as about $n_{circle}^{0.72}$. Again, as with an increasing circle radius, it is reasonable that the amount of scattering will increase with an increase in the number of circles, since the photons are likely to be refracted by more circles. A plot showing $\sigma_{scatter}$ as a function of photon energy is included in figure 6.3c. It was found that $\sigma_{scatter}$ varied as E_{photon}^{-2} . This is reasonable because the angular deviation from refraction from each circle is proportional to $1/E^2$ since δ is proportional to $1/E^2$. A plot showing $\sigma_{scatter}$ as a function of the absolute value of difference between the ambient δ and the circle δ is included in figure 6.3d. It was found that $\sigma_{scatter}$ varied linearly with $|\Delta\delta|$. This is reasonable since the refraction from each individual circle is linearly proportional to $|\Delta\delta|$. To summarize the findings of the model, the spreading of the x-ray beam is related to the size

of the scattering circles, the density of scattering circles, and the difference between the indices of refraction of the ambient and scattering materials. Also, USAXS is dependent upon x-ray energy.

6.5.2 *Experimental results*

A sample plot of normalized intensities of x-rays transmitted through water and bone as a function of the detuning angle of the analyzer crystal is included as figure 6.4. The experimentally measured scattering from the bone samples, σ_{scatter} , was 0.62 ± 0.24 $\mu\text{radians}$.

6.5.3 *Modeling structures in plexiform bone*

For the mineralized collagen fibril modeling experiment, the scattering width was found to be 70.4 ± 1.2 $\mu\text{radians}$. This is about 100 times the measured scattering width from the experiment. For the lacunae modeling experiment, the scattering width was found to be 0.888 ± 0.005 $\mu\text{radians}$. This is slightly larger than, but within an order of magnitude of, the experimental results.

It appears as though the mineralized collagen fibrils are not causing the measured USAXS signal. In the model, it is assumed that the mineralized collagen fibrils are discrete and separated from the neighboring fibrils by an ambient material. The ambient region surrounding the mineralized collagen fibrils has been shown to itself be mineralized,^{8,21} so it is likely there is no appreciable difference in index of refraction between the mineralized collagen fibrils and the surrounding material. The model was repeated keeping the scattering material as bone, but changing the ambient material. It was found that with a δ_{ambient} of

99.5% of δ_{bone} the scattering width, σ_{scatter} , was on the order of the experimentally measured scattering width (0.77 +/- 0.01 μ radians).

6.6 Discussion

The results from the model point towards the osteocyte lacunae as the structures that lead to the experimentally measured USAXS from the bone samples. Though parameters in the mineralized collagen fibril model were able to be varied in such a way as to generate scattering results that were consistent with the experimental results, δ of the ambient material was chosen to fit the experimental data and not to correspond to an experimentally measured value for δ in the region surrounding mineralized collagen fibrils in bone.

The slight overestimation of the scattering width in the computer model as compared to the experimentally obtained scattering width can be caused by a combination of factors. The difference between δ_{lacunae} and $\delta_{\text{plexiform bone}}$ could be smaller than the difference between δ_{water} and δ_{bone} since the actual chemical composition in the lacunae region in formalin-fixed bone is not known exactly. The average value of lacunae radius was used to calculate the scattering, but in an actual cross section of bone one would find a range of lacunae radii. Because the scattering width varies as $r_{\text{circle}}^{0.69}$, the lacunae with radii less than the average radius will cause there to be less scattering than if all lacunae had a radius equal to the average lacunae radius.

If indeed it is the osteocyte lacunae that are causing the measured USAXS from bone, then these results are promising. Vashishth et al²² showed that, for cortical bone, a decrease in lacunae density was accompanied by an increase microcracks, a increase in porosity, and

an overall decrease in bone strength. For their study, histological sections had to be used to count the lacunae and determine a lacunae density. If indeed the USAXS related to lacunae density, DEI would provide a non-invasive means of measuring lacunae density.

To design future experiments to further test the model, the only parameter that can be varied is the x-ray energy (the size, density, and material types are properties of the bone that is being imaged). The width of the intrinsic rocking curve of the DEI system is a function of energy and drops off as $1/E$.¹⁴ What is measured experimentally is the combination of the intrinsic rocking curve with the angular spreading of the x-rays due to USAXS. USAXS contrast is then related to the difference between the intrinsic rocking curve width and the rocking curve width as measured through the bone sample. The maximum USAXS contrast will occur where the difference between the intrinsic rocking curve width and the combined rocking curve width is the greatest. Since the USAXS width has been shown with the model to drop off as $1/E^2$, the difference between intrinsic rocking curve width and the combined rocking curve width will be greater the lower the x-ray energy. This needs to be balanced both with the fact that bone is highly absorbing for low energy x-rays (figure 6.5) and that the spectral brilliance of the x-ray source drops off significantly with increased energy.

6.7 Conclusions

A Monte Carlo ray tracing program was developed and tested for predicting ultra-small angle x-ray scattering from materials with a circular cross section. The response to the model to variations in parameters was recorded. The model was then used to determine what

structures in bovine cortical bone caused the experimentally measured USAXS. The USAXS was attributed to refractions from osteocyte lacunae in bone.

6.8 Acknowledgements

The research was supported by an NCSU FRPD grant, by the Department of the Army grant DAMD170110811, by the U.S. Department of Energy contract No. DE-AC02-98CH10886, and by the Brookhaven National Laboratory LDRD grant #05-057.

6.9 References

- ¹ J. Schmitt, P. Machtle, D. Eck, H. Mohwald, and C. A. Helm, "*Preparation and optical properties of colloidal gold monolayers*," *Langmuir* **15** (9), 3256 (1999).
- ² P. Fratzl, N. Fratzlzelman, K. Klaushofer, G. Vogl, and K. Koller, "*Nucleation and Growth of Mineral Crystals in Bone Studied by Small-Angle X-Ray-Scattering*," *Calcified Tissue International* **48** (6), 407 (1991).
- ³ N. P. Camacho, S. Rinnerthaler, E. P. Paschalis, R. Mendelsohn, A. L. Boskey, and P. Fratzl, "*Complementary information on bone ultrastructure from scanning small angle X-ray scattering and Fourier-transform infrared microspectroscopy*," *Bone* **25** (3), 287 (1999).
- ⁴ M. N. Wernick, O. Wirjadi, D. Chapman, Z. Zhong, N. P. Galatsanos, Y. Y. Yang, J. G. Brankov, O. Oltulu, M. A. Anastasio, and C. Muehleman, "*Multiple-image radiography*," *Physics in Medicine and Biology* **48** (23), 3875 (2003).
- ⁵ M. N. Wernick, O. Wirjadi, D. Chapman, Z. Zhong, O. Oltulu, and Y. Y. Yang, presented at the IEEE International Symposium on Biomedical Imaging, 2002 (unpublished).
- ⁶ S. Weiner and W. Traub, "*Bone-Structure - from Angstroms to Microns*," *Faseb Journal* **6** (3), 879 (1992).

- 7 P. Fratzl, H. S. Gupta, E. P. Paschalis, and P. Roschger, "*Structure and mechanical quality of the collagen-mineral nano-composite in bone*," *Journal of Materials Chemistry* **14** (14), 2115 (2004).
- 8 S. Weiner and H. D. Wagner, "*The material bone: Structure mechanical function relations*," *Annual Review of Materials Science* **28**, 271 (1998).
- 9 R. B. Martin and D. B. Burr, *Structure, function, and adaptation of compact bone*. (Raven Press, New York, 1989).
- 10 V. Cane, G. Marotti, G. Volpi, D. Zaffe, S. Palazzini, F. Remaggi, and M. A. Muglia, "*Size and Density of Osteocyte Lacunae in Different Regions of Long Bones*," *Calcified Tissue International* **34** (6), 558 (1982).
- 11 S. K. Park and K. W. Miller, "*Random Number Generators - Good Ones Are Hard to Find*," *Communications of the Acm* **31** (10), 1192 (1988).
- 12 M. Z. Kiss, D. E. Sayers, and Z. Zhong, "*Measurement of image contrast using diffraction enhanced imaging*," *Physics in Medicine and Biology* **48** (3), 325 (2003).
- 13 D. Chapman, W. Thomlinson, R. E. Johnston, D. Washburn, E. Pisano, N. Gmur, Z. Zhong, R. Menk, F. Arfelli, and D. Sayers, "*Diffraction enhanced x-ray imaging*," *Physics in Medicine and Biology* **42** (11), 2015 (1997).
- 14 Zhong Zhong, William Thomlinson, Dean Chapman, and Dale Sayers, "*Implementation of diffraction-enhanced imaging experiments: at the NSLS and APS*," *Nuclear Instruments and Methods in Physics Research A* **450**, 556 (2000).
- 15 F. A. Dilmanian, Z. Zhong, B. Ren, X. Y. Wu, L. D. Chapman, I. Orion, and W. C. Thomlinson, "*Computed tomography of x-ray index of refraction using the diffraction enhanced imaging method*," *Physics in Medicine and Biology* **45** (4), 933 (2000).
- 16 M N; Wirjadi Wernick, O; Chapman, D; Zhong, Z; Galatsanos, N; Yang, Y; Brankov, J; Oltulu, O; Anastasio, M; Muehleman, C, "*Multiple-image radiography*," *Physics in Medicine and Biology* **48**, 3875 (2003).

- 17 K. M. Pavlov, C. M. Kewish, J. R. Davis, and M. J. Morgan, "*A variant on the geometrical optics approximation in diffraction enhanced tomography*," *Journal of Physics D-Applied Physics* **34** (10A), A168 (2001).
- 18 William H. Zachariasen, *Theory of X-ray diffraction in crystals*. (J. Wiley, New York, 1945).
- 19 D. M. Connor, D. Sayers, D. R. Sumner, and Z. Zhong, "*Identification of fatigue damage in cortical bone by diffraction enhanced imaging*," *Nuclear Instruments & Methods in Physics Research Section a-Accelerators Spectrometers Detectors and Associated Equipment* **548** (1-2), 234 (2004).
- 20 J. H. Hubbell and S. M. Seltzer, *Tables of X-Ray Mass Attenuation Coefficients and Mass Energy-Absorption Coefficients (version 1.3)*, Retrieved April, 2004, from <http://physics.nist.gov/xaamdi>.
- 21 E. P. Katz and S. Li, "*Structure and Function of Bone Collagen Fibrils*," *Journal of Molecular Biology* **80** (1), 1 (1973).
- 22 D. Vashishth, O. Verborgt, G. Divine, M. B. Schaffler, and D. P. Fyhrie, "*Decline in osteocyte lacunar density in human cortical bone is associated with accumulation of microcracks with age*," *Bone* **26** (4), 375 (2000).

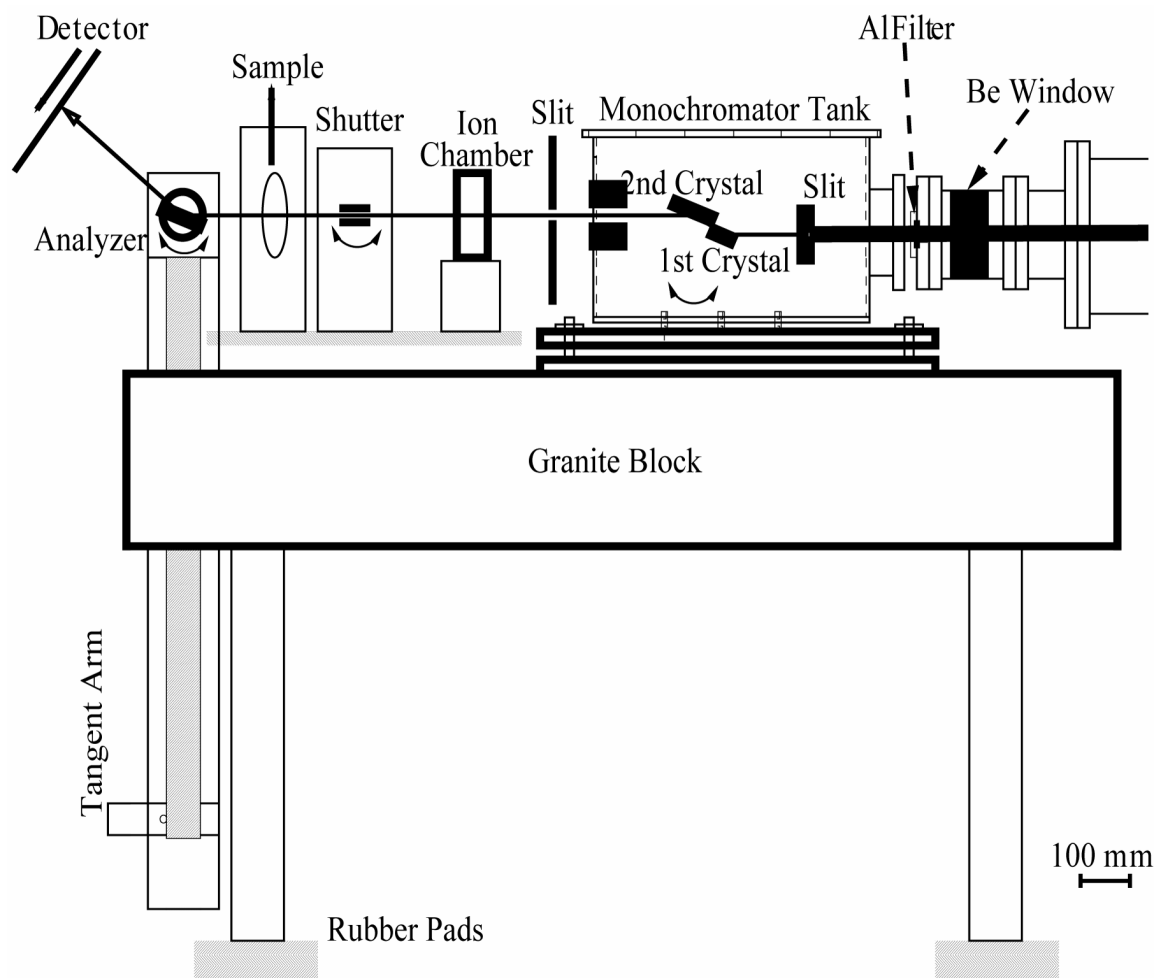


Figure 6.1 Experimental setup at NSLS beamline X15A, Upton, NY, USA

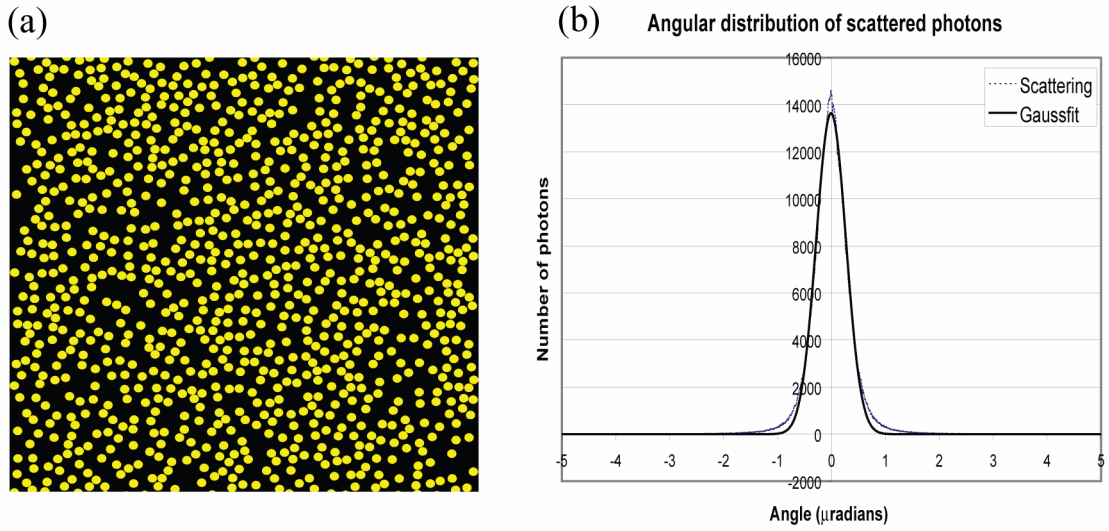


Figure 6.2 (a) Image of circles in a sample scatter region in the computer model. (b) Histogram of the photon scattering angles (dotted line) and the Gaussian fit to the histogram (solid line) for one million photons transmitted through sample scattering region.

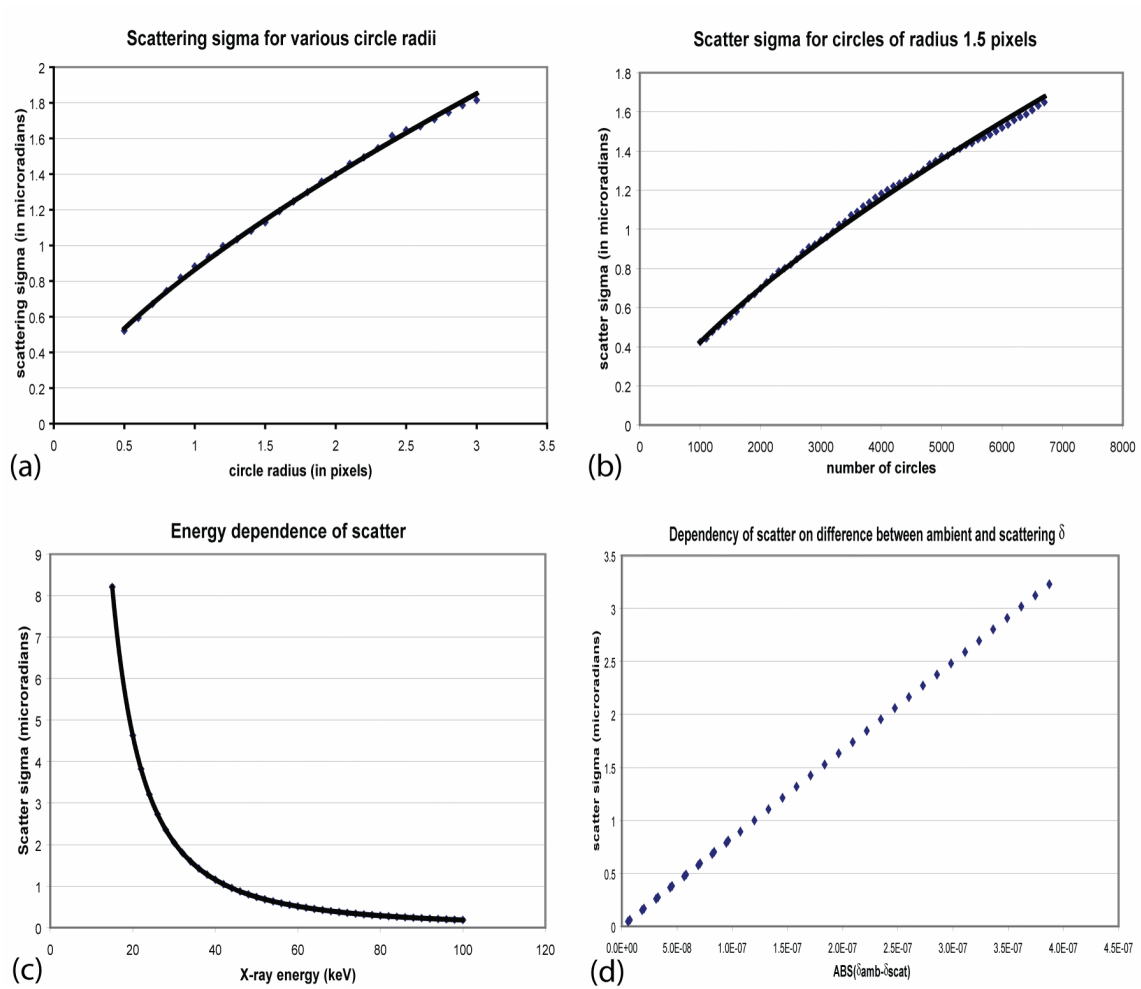


Figure 6.3 Results of varying parameters in the computer model. Plots of the predicted $\sigma_{scatter}$ as a function of (a) the scattering circle radius, r_{circle} ($n_{circles}=4000$, $E_{photon}=40$ keV, $\Delta\delta=1.33 \times 10^{-7}$), (b) the number of scattering circles, n_{circle} ($r_{circle}=1.5$ pixels, $E_{photon}=40$ keV, $\Delta\delta=1.33 \times 10^{-7}$), (c) the photon energy, E_{photon} ($n_{circles}=4000$, $r_{circle}=1.5$ pixels, $\Delta\delta=1.33 \times 10^{-7}$), and (d) the difference between the real part of index of refraction of the ambient and scattering regions $\Delta\delta$ ($r_{circle}=1.5$ pixels, $n_{circles}=4000$, $E_{photon}=40$ keV).

Comparison of ambient and bone rocking curves

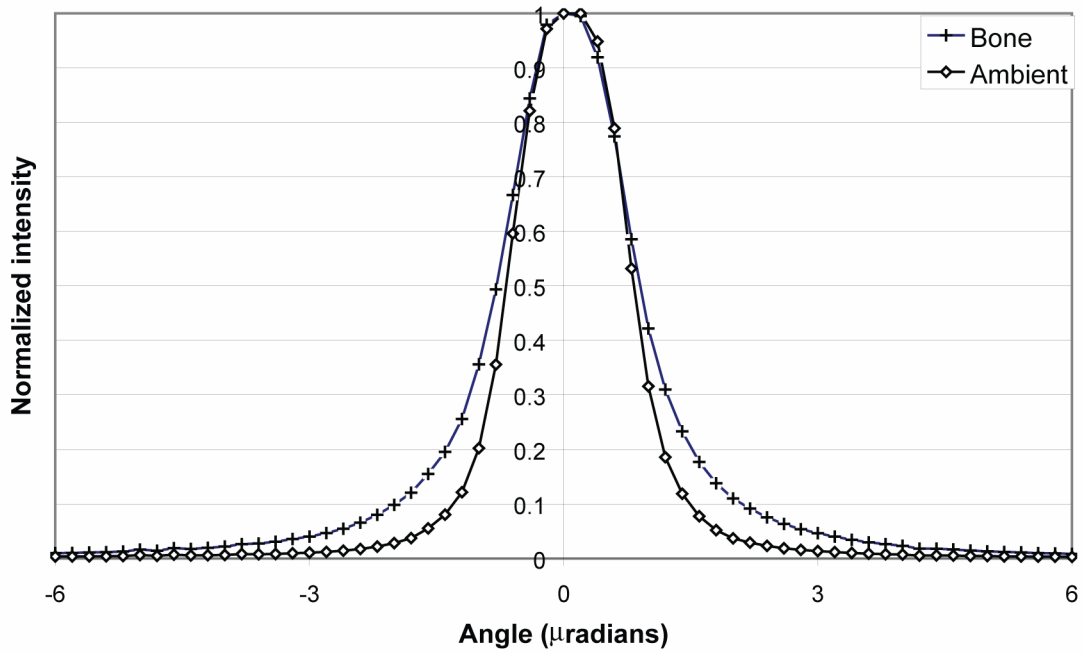


Figure 6.4 Plot of the normalized rocking curves through bone (plus sign) and through water (ambient region; diamonds).

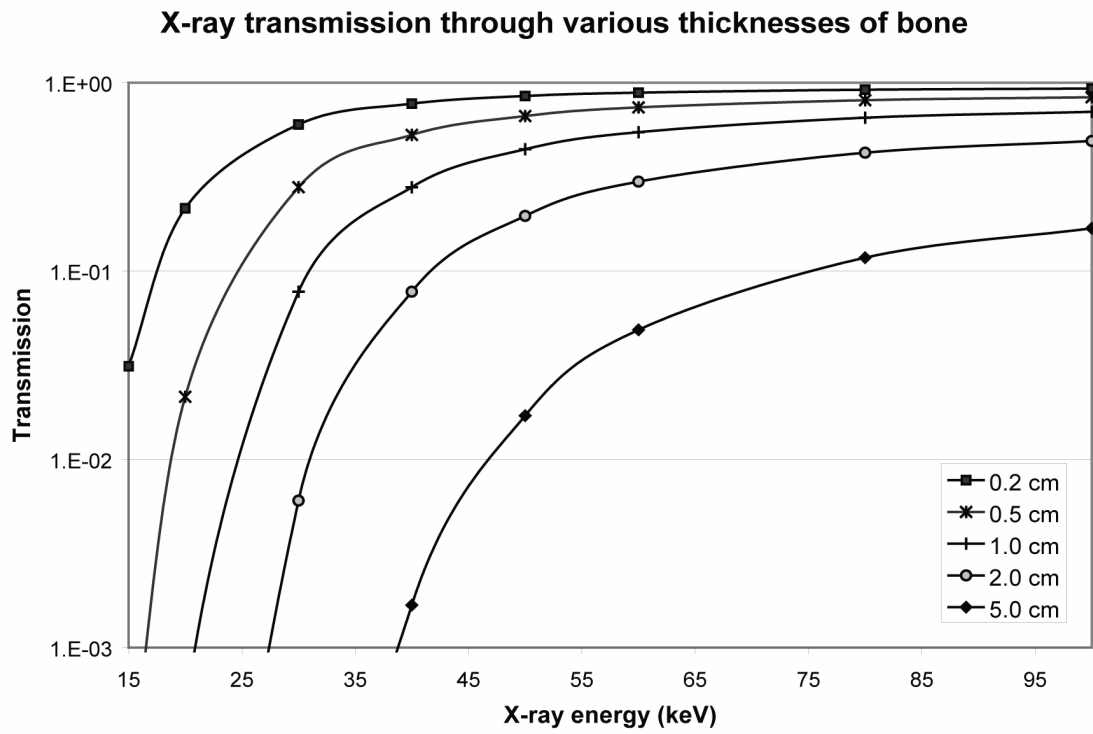


Figure 6.5 Plots of the x-ray transmission as a function of x-ray energy through a variety of bone thicknesses.

7 CONCLUSIONS AND FUTURE WORK

Because DEI is in its infancy, much work has to be done before it can be established as a medical imaging modality. As stated earlier, the overall goal of these experiments was to help lay a foundation for future DEI of bone. Each experiment sheds some light onto DEI of bone and its potential usefulness. In the pre- and post-fatigue loaded bone experiment, it was found that, though no significant change in rocking curve width could be found, the refraction signal within bone was not overwhelmed by the USAXS present. This finding led to the second two experiments. In the interface gap experiment, it was determined that the DEI refraction image showed significant contrast-to-noise ratio gains over comparably obtained SR radiographs. The refraction measured with DEI, though somewhat degraded by the USAXS, was still present to the extent that the refraction images showed CNR gains and the measured refraction values were consistent with their theoretically predicted value. In the third experiment, both apparent absorption and refraction DECT slice images were shown to have both contrast and resolution gains over comparably obtained SRCT slice images. In the final experiment, the computer model developed to predict USAXS in bone was able to produce an USAXS signal that was consistent with experimentally measured USAXS values.

These four experiments are just the starting point. The x-ray interaction with bone will need to be further characterized in order to have a more full understanding of the potential use for—and the limitations of—DEI in bone imaging applications. Though the experiments summarized here have shown DEI to have contrast advantages over SR radiography, the studies were done as proof-of-principle studies, so only a very limited number of samples were imaged. A much greater number of samples will need to be imaged

in the future. In the final experiment, the results suggest that lacunae are causing the measured USAXS, but further experiments will need to be done to confirm this.

Decisions will have to be made as to whether DEI is best used as clinical imaging modality or if it is better suited for ex vivo imaging (such as current micro CT systems).

Ultimately, in order for DEI to be a diagnostically useful tool, a clinical DEI system—or at least a non-synchrotron-based system—will need to be developed.

8 REFERENCES

J. Als-Nielsen and D. McMorrow, *Elements of Modern X-Ray Physics*. (Wiley, New York, 2001).

B. W. Batterman and H. Cole, "Dynamical Diffraction of X Rays by Perfect Crystals," *Reviews of Modern Physics* **36** (3), 681 (1964).

T. W. Bauer and J. Schils, "The pathology of total joint arthroplasty - II. Mechanisms of implant failure," *Skeletal Radiology* **28** (9), 483 (1999).

J. Black, R. Mattson, and Korostof.E, "Haversian Osteons - Size, Distribution, Internal Structure, and Orientation," *Journal of Biomedical Materials Research* **8** (5), 299 (1974).

J. M. Boone and J. A. Seibert, "A Comparison of Mono-Energetic and Poly-Energetic X-Ray-Beam Performance for Radiographic and Fluoroscopic Imaging," *Medical Physics* **21** (12), 1853 (1994).

J. H. Boss, I. Shajrawi, and D. G. Mendes, "The Nature of the Bone - Implant Interface," *Medical Progress through Technology* **20** (3-4), 119 (1994).

N. P. Camacho, S. Rinnerthaler, E. P. Paschalis, R. Mendelsohn, A. L. Boskey, and P. Fratzl, "Complementary information on bone ultrastructure from scanning small angle X-ray scattering and Fourier-transform infrared microspectroscopy," *Bone* **25** (3), 287 (1999).

V. Cane, G. Marotti, G. Volpi, D. Zaffe, S. Palazzini, F. Remaggi, and M. A. Muglia, "Size and Density of Osteocyte Lacunae in Different Regions of Long Bones," *Calcified Tissue International* **34** (6), 558 (1982).

D. Chapman, W. Thomlinson, R. E. Johnston, D. Washburn, E. Pisano, N. Gmur, Z. Zhong, R. Menk, F. Arfelli, and D. Sayers, "Diffraction enhanced x-ray imaging," *Physics in Medicine and Biology* **42** (11), 2015 (1997).

Dean Chapman, William Thomlinson, F. Arfelli, N. Gmür, Zhong Zhong, R. Menk, R.E. Johnston, D. Washburn, Etta Pisano, and Dale Sayers, "*Mammography imaging studies using a Laue crystal analyzer*," Review of Scientific Instruments **67** (9), (published on CD (1996).

D. M. Connor, D. Sayers, D. R. Sumner, and Z. Zhong, "*Identification of fatigue damage in cortical bone by diffraction enhanced imaging*," Nuclear Instruments & Methods in Physics Research Section a-Accelerators Spectrometers Detectors and Associated Equipment **548** (1-2), 234 (2004).

D.M.L. Cooper, A.L. Turinsky, C.W. Sensen, and B. Hallgrímsson, "*Quantitative 3D analysis of the canal network in cortical bone by micro-computed tomography*," The Anatomical Record Part B: The New Anatomist **274B** (1), 169 (2003).

F. A. Dilmanian, Z. Zhong, B. Ren, X. Y. Wu, L. D. Chapman, I. Orion, and W. C. Thomlinson, "*Computed tomography of x-ray index of refraction using the diffraction enhanced imaging method*," Physics in Medicine and Biology **45** (4), 933 (2000).

L. A. Feldkamp, S. A. Goldstein, A. M. Parfitt, G. Jasion, and M. Kleerekoper, "*The Direct Examination of 3-Dimensional Bone Architecture Invitro by Computed-Tomography*," Journal of Bone and Mineral Research **4** (1), 3 (1989).

S. Fiedler, A. Bravin, J. Keyrilainen, M. Fernandez, P. Suortti, W. Thomlinson, M. Tenhunen, P. Virkkunen, and M. L. Karjalainen-Lindsberg, "*Imaging lobular breast carcinoma: comparison of synchrotron radiation DEI-CT technique with clinical CT, mammography and histology*," Physics in Medicine and Biology **49** (2), 175 (2004).

P. Fratzl, N. Fratzlzelman, K. Klaushofer, G. Vogl, and K. Koller, "*Nucleation and Growth of Mineral Crystals in Bone Studied by Small-Angle X-Ray-Scattering*," Calcified Tissue International **48** (6), 407 (1991).

P. Fratzl, H. S. Gupta, E. P. Paschalis, and P. Roschger, "*Structure and mechanical quality of the collagen-mineral nano-composite in bone*," Journal of Materials Chemistry **14** (14), 2115 (2004).

L. Gang, Z. H. Chen, Z. Y. Wu, M. Ando, P. Lin, J. Y. Wang, and X. M. Jiang, "*Image quality dependence on thickness of sliced rat kidney taken by a simplest DEI construction*," Nuclear Instruments & Methods in Physics Research Section a-

Accelerators Spectrometers Detectors and Associated Equipment **548** (1-2), 200 (2004).

M. Hasnah, O. Oltulu, Z. Zhong, and D. Chapman, "*Application of absorption and refraction matching techniques for diffraction enhanced imaging*," Review of Scientific Instruments **73** (3), 1657 (2002).

M. O. Hasnah, C. Parham, E. D. Pisano, Z. Zhong, O. Oltulu, and D. Chapman, "*Mass density images from the diffraction enhanced imaging technique*," Medical Physics **32** (2), 549 (2005).

T. Hildebrand, A. Laib, R. Muller, J. Dequeker, and P. Ruegsegger, "*Direct three-dimensional morphometric analysis of human cancellous bone: Microstructural data from spine, femur, iliac crest, and calcaneus*," Journal of Bone and Mineral Research **14** (7), 1167 (1999).

J. P. Hodgkinson, P. Shelley, and B. M. Wroblewski, "*The Correlation between the Roentgenographic Appearance and Operative Findings at the Bone-Cement Junction of the Socket in Charnley Low Friction Arthroplasties*," Clinical Orthopaedics and Related Research (228), 105 (1988).

J. H. Hubbell and S. M. Seltzer, *Tables of X-Ray Mass Attenuation Coefficients and Mass Energy-Absorption Coefficients (version 1.3)*, Retrieved April, 2004, from <http://physics.nist.gov/xaamdi>.

R. W. James, *The optical principles of the diffraction of x-rays*. (Ox Bow Press, Woodbridge, Conn., 1982).

R. E. Johnston, D. Washburn, E. Pisano, C. Burns, W. C. Thomlinson, L. D. Chapman, F. Arfelli, N. F. Gmur, Z. Zhong, and D. Sayers, "*Mammographic phantom studies with synchrotron radiation*," Radiology **200** (3), 659 (1996).

E. P. Katz and S. Li, "*Structure and Function of Bone Collagen Fibrils*," Journal of Molecular Biology **80** (1), 1 (1973).

T. M. Keaveny, E. F. Morgan, G. L. Niebur, and O. C. Yeh, "*Biomechanics of trabecular bone*," Annual Review of Biomedical Engineering **3**, 307 (2001).

J. Keyrilainen, M. Fernandez, and P. Suortti, "*Refraction contrast in X-ray imaging*," Nuclear Instruments & Methods in Physics Research Section a-Accelerators Spectrometers Detectors and Associated Equipment **488** (1-2), 419 (2002).

M. Z. Kiss, D. E. Sayers, and Z. Zhong, "*Comparison of X-ray detectors for a diffraction enhanced imaging system*," Nuclear Instruments & Methods in Physics Research Section a-Accelerators Spectrometers Detectors and Associated Equipment **491** (1-2), 280 (2002).

M. Z. Kiss, D. E. Sayers, and Z. Zhong, "*Measurement of image contrast using diffraction enhanced imaging*," Physics in Medicine and Biology **48** (3), 325 (2003).

M. Z. Kiss, D. E. Sayers, Z. Zhong, C. Parham, and E. D. Pisano, "*Improved image contrast of calcifications in breast tissue specimens using diffraction enhanced imaging*," Physics in Medicine and Biology **49** (15), 3427 (2004).

M. Kothari, T. M. Keaveny, J. C. Lin, D. C. Newitt, H. K. Genant, and S. Majumdar, "*Impact of spatial resolution on the prediction of trabecular architecture parameters*," Bone **22** (5), 437 (1998).

A. Laib and P. Ruegsegger, "*Comparison of structure extraction methods for in vivo trabecular bone measurements*," Computerized Medical Imaging and Graphics **23** (2), 69 (1999).

R. A. Lewis, C. J. Hall, A. P. Hufton, F. Arfelli, A. J. Evans, and S. H. Evans, "*X-ray diffraction-enhanced imaging (DEI)*," Radiology **221**, 165 (2001).

R. A. Lewis, C. J. Hall, A. P. Hufton, S. Evans, R. H. Menk, F. Arfelli, L. Rigon, G. Tromba, D. R. Dance, I. O. Ellis, A. Evans, E. Jacobs, S. E. Pinder, and K. D. Rogers, "*X-ray refraction effects: application to the imaging of biological tissues*," British Journal of Radiology **76** (905), 301 (2003).

T. M. Link, S. Majumdar, S. Grampp, G. Guglielmi, C. van Kuijk, H. Imhof, C. Glueer, and J. E. Adams, "*Imaging of trabecular bone structure in osteoporosis*," European Radiology **9** (9), 1781 (1999).

S. Majumdar, A. S. Issever, A. Burghardt, J. Lotz, F. Arfelli, L. Rigon, G. Heitner, and R. H. Menk, "*Diffraction enhanced imaging of articular cartilage and*

comparison with micro-computed tomography of the underlying bone structure," European Radiology **14** (8), 1440 (2004).

K. A. Mannan, E. Schultke, R. H. Menk, K. Siu, K. Pavlov, M. Kelly, G. McLoughlin, T. Beveridge, G. Tromba, B. H. Juurlink, D. Chapman, L. Rigon, and R. W. Griebel, "*Synchrotron supported DEI/KES of a brain tumor in an animal model: The search for a microimaging modality,*" Nuclear Instruments & Methods in Physics Research Section a-Accelerators Spectrometers Detectors and Associated Equipment **548** (1-2), 106 (2004).

G. Margaritondo, *Introduction to Synchrotron Radiation*. (Oxford University Press, New York, 1988).

R. B. Martin and D. B. Burr, *Structure, function, and adaptation of compact bone*. (Raven Press, New York, 1989).

S. Mishra and M. L. K. Tate, "*Effect of lacunocanalicular architecture on hydraulic conductance in bone tissue: Implications for bone health and evolution,*" Anatomical Record Part a-Discoveries in Molecular Cellular and Evolutionary Biology **273A** (2), 752 (2003).

J. Mollenhauer, M. E. Aurich, Z. Zhong, C. Muehleman, C. C. Cole, M. Hasnah, O. Oltulu, K. E. Kuettner, A. Margulis, and L. D. Chapman, "*Diffraction-enhanced X-ray imaging of articular cartilage,*" Osteoarthritis and Cartilage **10** (3), 163 (2002).

C. S. Moucha, R. M. Urban, T. M. Turner, J. J. Jacobs, and D. R. Sumner, in *Joint replacements and bone resorption: pathology, biomaterials and clinical practice*, edited by A. Shanbhag, H. E. Rubash, and J. J. Jacobs (Marcel Dekker, New York, 2005 (in press)), pp. 13.

C. Muehleman, M. Whiteside, Z. Zhong, J. Mollenhauer, M. Aurich, K. E. Kuettner, and L. D. Chapman, "*Diffraction enhanced imaging for articular cartilage,*" Biophysical Journal **82** (1), 470A (2002).

C. Muehleman, L. D. Chapman, K. E. Kuettner, J. Rieff, J. A. Mollenhauer, K. Massuda, and Z. Zhong, "*Radiography of rabbit articular cartilage with diffraction-enhanced imaging,*" Anatomical Record Part a-Discoveries in Molecular Cellular and Evolutionary Biology **272A** (1), 392 (2003).

C. Muehleman, S. Majumdar, A. S. Issever, F. Arfelli, R. H. Menk, L. Rigon, G. Heitner, B. Reime, J. Metge, A. Wagner, K. E. Kuettner, and J. Mollenhauer, "*X-ray detection of structural orientation in human articular cartilage*," *Osteoarthritis and Cartilage* **12** (2), 97 (2004).

C. Muehleman, D. R. Sumner, and Z. Zhong, "*Refraction effects of diffraction enhanced radiographic imaging - A new look at bone*," *Journal of the American Podiatric Medical Association* **94** (5), 453 (2004).

R. Muller, M. Hahn, M. Vogel, G. Delling, and P. Ruegsegger, "*Morphometric analysis of noninvasively assessed bone biopsies: Comparison of high-resolution computed tomography and histologic sections*," *Bone* **18** (3), 215 (1996).

R. Muller, H. Van Campenhout, B. Van Damme, G. Van Der Perre, J. Dequeker, T. Hildebrand, and P. Ruegsegger, "*Morphometric analysis of human bone biopsies: A quantitative structural comparison of histological sections and micro-computed tomography*," *Bone* **23** (1), 59 (1998).

A. Odgaard, "*Three-dimensional methods for quantification of cancellous bone architecture*," *Bone* **20** (4), 315 (1997).

O. Oltulu, Z. Zhong, M. Hasnah, M. N. Wernick, and D. Chapman, "*Extraction of extinction, refraction and absorption properties in diffraction enhanced imaging*," *Journal of Physics D-Applied Physics* **36** (17), 2152 (2003).

E. Pagot, P. Cloetens, S. Fiedler, A. Bravin, P. Coan, J. Baruchel, J. Hartwig, and W. Thomlinson, "*A method to extract quantitative information in analyzer-based x-ray phase contrast imaging*," *Applied Physics Letters* **82** (20), 3421 (2003).

E. Pagot, S. Fiedler, P. Cloetens, A. Bravin, P. Coan, K. Fezzaa, J. Baruchel, and J. Hartwig, "*Quantitative comparison between two phase contrast techniques: diffraction enhanced imaging and phase propagation imaging*," *Physics in Medicine and Biology* **50** (4), 709 (2005).

S. K. Park and K. W. Miller, "*Random Number Generators - Good Ones Are Hard to Find*," *Communications of the Acm* **31** (10), 1192 (1988).

K. M. Pavlov, C. M. Kewish, J. R. Davis, and M. J. Morgan, "*A variant on the geometrical optics approximation in diffraction enhanced tomography*," *Journal of Physics D-Applied Physics* **34** (10A), A168 (2001).

E. D. Pisano, R. E. Johnston, D. Chapman, J. Geradts, M. V. Iacocca, C. A. Livasy, D. B. Washburn, D. E. Sayers, Z. Zhong, M. Z. Kiss, and W. C. Thomlinson, "*Human breast cancer specimens: Diffraction-enhanced imaging with histologic correlation - Improved conspicuity of lesion detail compared with digital radiography*," *Radiology* **214** (3), 895 (2000).

G. C. Reilly, H. F. Knapp, A. Stemmer, P. Niederer, and M. L. K. Tate, "*Investigation of the morphology of the lacunocanalicular system of cortical bone using atomic force microscopy*," *Annals of Biomedical Engineering* **29** (12), 1074 (2001).

M. Rivers, *Tutorial Introduction to X-ray Computed Microtomography Data Processing*, Retrieved August 13, 2003, from <http://www-fp.mcs.anl.gov/xray-cmt/rivers/tutorial.html>.

H. S. Rocha, R. T. Lopes, L. M. Pessoa, M. G. Honnicke, G. Tirao, C. Cusatis, I. Mazzaro, and C. Giles, "*Diffraction-enhanced imaging for studying pattern recognition in cranial ontogeny of bats and marsupials*," *Nuclear Instruments & Methods in Physics Research Section a-Accelerators Spectrometers Detectors and Associated Equipment* **548** (1-2), 228 (2004).

H. S. Rocha, R. T. Lopes, P. M. Valiante, G. Tirao, I. Mazzaro, M. G. Honnicke, C. Cusatis, and C. Giles, "*Diagnosis of thyroid multinodular goiter using diffraction-enhanced imaging*," *Nuclear Instruments & Methods in Physics Research Section a-Accelerators Spectrometers Detectors and Associated Equipment* **548** (1-2), 175 (2004).

J. Schmitt, P. Machtle, D. Eck, H. Mohwald, and C. A. Helm, "*Preparation and optical properties of colloidal gold monolayers*," *Langmuir* **15** (9), 3256 (1999).

E. M. Schwarz, D. Campbell, S. Totterman, A. Boyd, R. J. O'Keefe, and R. J. Looney, "*Use of volumetric computerized tomography as a primary outcome measure to evaluate drug efficacy in the prevention of peri-prosthetic osteolysis: a 1-year clinical pilot of etanercept vs. placebo*," *Journal of Orthopaedic Research* **21** (6), 1049 (2003).

D. R. Sumner, in *The Adult Knee*, edited by J. J. Callaghan, A. G. Rosenberg, H. E. Rubash et al. (Lippincott Williams & Wilkins, Philadelphia, 2003), pp. 289.

D. Ulrich, B. Van Rietbergen, A. Laib, and P. Ruegsegger, "*The ability of three-dimensional structural indices to reflect mechanical aspects of trabecular bone*," *Bone* **25** (1), 55 (1999).

D. Vashishth, O. Verborgt, G. Divine, M. B. Schaffler, and D. P. Fyhrie, "*Decline in osteocyte lacunar density in human cortical bone is associated with accumulation of microcracks with age*," *Bone* **26** (4), 375 (2000).

B. E. Warren, *X-ray diffraction*. (Addison-Wesley Pub. Co., Reading, Mass., 1969).

S. Weiner and W. Traub, "*Bone-Structure - from Angstroms to Microns*," *Faseb Journal* **6** (3), 879 (1992).

S. Weiner and H. D. Wagner, "*The material bone: Structure mechanical function relations*," *Annual Review of Materials Science* **28**, 271 (1998).

M. N. Wernick, O. Wirjadi, D. Chapman, Z. Zhong, O. Oltulu, and Y. Y. Yang, presented at the IEEE International Symposium on Biomedical Imaging, 2002 (unpublished).

M. N. Wernick, O. Wirjadi, D. Chapman, Z. Zhong, N. P. Galatsanos, Y. Y. Yang, J. G. Brankov, O. Oltulu, M. A. Anastasio, and C. Muehleman, "*Multiple-image radiography*," *Physics in Medicine and Biology* **48** (23), 3875 (2003).

W.J. Whitehou, "*Quantitative Morphology of Anisotropic Trabecular Bone*," *Journal of Microscopy-Oxford* **101** (JUL), 153 (1974).

William H. Zachariasen, *Theory of x-ray diffraction in crystals*. (Dover Publications, New York, 1994).

Z. Zhong, D. Chapman, W. Thomlinson, F. Arfelli, and R. Menk, "*A bent Laue crystal monochromator for monochromatic radiography with an area beam*," *Nuclear Instruments & Methods in Physics Research Section a-Accelerators Spectrometers Detectors and Associated Equipment* **399** (2-3), 489 (1997).

Zhong Zhong, William Thomlinson, Dean Chapman, and Dale Sayers,
"Implementation of diffraction-enhanced imaging experiments: at the NSLS and
APS," Nuclear Instruments and Methods in Physics Research A **450**, 556 (2000).